ELUCIDATION OF ULTRAFAST PHOTOPHYSICS WITH OPTICAL PULSE SHAPING

by

ERIK MARTIN GRUMSTRUP

B.S., University of Minnesota, 2006

A thesis submitted to the

Faculty of the Graduate School of the

University of Colorado in partial fulfillment

of the requirement for the degree of

Doctor of Philosophy

Chemical Physics

2011

This thesis entitled:
Elucidation of Ultrafast Photophysics with Optical Pulse Shaping
written by Erik Martin Grumstrup
has been approved for the Chemical Physics program

_____
Niels H. Damrauer

_____
David M. Jonas

Date_____

The final copy of this thesis has been examined by the signatories and we find that both the content and the form meet acceptable presentation standards of scholarly work in the above mentioned discipline.

ABSTRACT

Grumstrup, Erik Martin (Ph.D., Chemical Physics)

Elucidation of Ultrafast Photophysics with Optical Pulse Shaping

Thesis directed by Professor Niels H. Damrauer

Optical pulse shaping is an incisive tool of laser spectroscopy that allows the experimentalist extensive flexibility to manipulate the electric field of an excitation laser pulse. In this thesis, four applications of optical pulse shaping are examined. In Chapter 2, a partially non-collinear implementation of two-dimensional electronic spectroscopy is demonstrated for the first time on rubidium vapor. The use of a pulse shaper in this context is advantageous as it significantly reduces the complexity of the experimental apparatus. Unfortunately, non-ideal pulse shaping due to pixelation effects in some pulse-shaping devices leads to spurious pulse generation when the spatial masks become highly modulated. To model the effects on recovered 2D spectra, the optical Bloch model is numerically propagated with an explicit inclusion of the electric field modified by pixelation effects. Finally, steps necessary to minimize distortions are outlined. Chapter 3 describes a series of experiments designed to study the mechanism of multiple exciton generation in semiconductor quantum dots through open and closed loop coherent control schemes. The data collected with open loop control methods indicate that the initially formed exciton relaxes on an ultrafast time scale (<20 fs) revealing the reason for a lack of controllability in adaptive, closed-loop optimizations. Chapter 4 of this thesis examines the

process of singlet fission in tetracene thin films employing coherent control and ultrafast pulse shaping. Singlet fission is a promising avenue to achieving highly efficient third generation photovoltaic devices, and in this work, closed-loop control suggests that low-frequency nuclear motions play a mechanistic role in tetracene singlet fission. Finally, Chapter 5 examines a specific class of pulse shaping, sinusoidal spectral phase modulation, which is widely employed in the coherent control community as a route toward an intuitive probe into molecular dynamics. This work seeks to build a bridge between the fields of nonlinear spectroscopy and coherent control by describing the light-matter interactions characteristic of this type of pulse shaping using the tools of time-dependent perturbation theory. This description allows experimentalists to predict and test theories of coherent control simply and with little ambiguity, furthering the usefulness of coherent control as a spectroscopic tool.

CONTENTS

TABLES

Chapter 5 A Time Dependent Perspective of Sinusoidal Spectral Phase Modulation

FIGURES

CHAPTER 1

INTRODUCTION

1.1 Introductory Remarks

It cannot be understated how much the advent of the laser has revolutionized spectroscopy in chemistry and physics. Lasers have allowed an unprecedented glimpse into the complex nuclear and electronic dynamics that give rise to the statistical properties commonly observable for molecular and material systems. Furthermore, with the development of lasers capable of producing pulses with extremely short durations on picosecond (10^{-12} s) and femtosecond (10^{-15} s) timescales, laser spectroscopy has advanced a multitude of time domain techniques which are especially relevant to the study of condensed phase systems. [1]

A complementary technology to ultrashort pulse generation is optical pulse shaping, wherein the amplitudes and phases of the individual spectral components comprising an ultrashort pulse are manipulated. [2] This technology has had far reaching consequences within the laser spectroscopy community. With Nelson's early work showing how pulse shaping with lithographically etched spatial masks could

isolate desired phonon modes [3], to the ability to practically and routinely compress chirped ultrashort pulses [4-6], pulse shaping has dramatically increased the practicality and flexibility of ultrafast spectroscopy.

The most prominent field that couples ultrafast laser spectroscopy and optical pulse shaping is coherent control, which was set in motion with proposals by Tannor and Rice [7,8] as well as Brumer and Shapiro [9,10]. Coherent control was in some sense a natural response to the long-standing desire to steer chemical reactions toward a non-statistical product with laser excitation, especially while dephasing and energy relaxation processes are occurring. [11-13] It differed from previously employed attempts at "laser chemistry" in that it allowed active control over the evolution of a prepared state by manipulating input parameters of an applied light field. A dramatic body of work followed these initial proposals including demonstrations of bond selective chemistry [14-17], control of multiphoton absorption and Raman transitions [18-27], and control over population transfer by matching temporal chirp to the stokes shift of an evolving wavepacket [28-31]. However, the goal of coherent control of producing usable quantities of photochemical products steered by excitation with shaped light fields has so far proved to be insurmountable—it has not become the arbitrarily flexible panacea of synthetic chemistry that was hoped for. [14]

Nevertheless, since the early 2000s pulse shaping in the context of coherent control has become a field that has matured beyond mere demonstration of controllability in various chemical systems. It has become a powerful spectroscopic tool in its own right, advancing beyond the realm of pure multiphoton physics and gas phase

reactions to carve out an important role in the understanding of ultrafast chemical dynamics in the condensed phase. An early example of this is Herek's and Motzkus' work in which a learning algorithm [32] converged on a shaped pulse that affected the branching ratio between internal conversion and energy transfer in a natural light-harvesting antennae (LH2 from a photosynthetic purple bacteria). [33] Further study on a similar system suggested that the shaped pulses acted to create vibrationally hot ground states, which upon excitation to higher lying excited states, evolved along different trajectories, thereby affecting the branching ratio. [34]

There are further examples, using both open and closed loop strategies [32], of how pulse shaping and coherent control are a driving force in the study of novel molecular dynamics. Advancements include resonant vibrational mode enhancement [35-38] and studies of solvent dependent decoherence [39]. Another striking contribution arising from the field was the realization that linear (one-photon) control, once thought to be nebulous and ill-reasoned wishful thinking [40] has, through years of experiments [39,41-43] and (sometimes contentious) discourse [44,45] been shown to be a genuine and highly relevant property of non-Markovian condensed phase molecular physics. [46,47]

So while it is perhaps true that coherent control will never be taught in organic synthesis texts as a preparative strategy, it has turned out to be an incisive tool for examination of processes like dephasing, photophysics along active vibrational coordinates, and the importance of system bath interactions in ultrafast relaxation. Nevertheless, the spectroscopic interpretation of complex results, which are often

natural products of closed loop optimization algorithms, is still in its infancy, remaining a hurdle to successful, routine inquiries with coherent control. To address this difficulty, strategies that simplify the complex spectral phase functions, which are often the outcome of closed loop optimizations, have been developed and experimentally employed to uncover physically meaningful parameters. [26,48-51] In addition, theoretical work in optimal control theory has shown that complex optimal pulse shapes can often be dramatically simplified to intuitive shapes with comparable fitness, reflecting information about molecular dynamics. [52,53] And in this lab, theoretical and experimental work has been undertaken that demonstrates fundamental links between interferometric methods and coherent control of multiphoton processes. [54,55]

Nevertheless, much work remains to be done. The literature still abounds with qualitative descriptions of control mechanisms that, though appealing in their link to original control schemes invoked by Tannor and Rice and Brumer and Shapiro, lack the rigor and formalism necessary for the creation of accurate models, development of predictive theories, and forging of links between nonlinear spectroscopy and coherent control. Pulse shaping is a unique technique in that it has nearly unlimited flexibility for the design of fields to probe complex systems. To exploit the full power of the technique, however, the complexities that are intrinsic to open and closed loop techniques must be further understood. The work presented in this dissertation seeks to address some of these shortcomings with theoretical and experimental studies of atomic, molecular, and solid state systems.

The remainder of this chapter will first discuss optical pulse shaping and give a brief description of how it is performed in our lab. Following that, some background information about what coherent control is and what questions it seeks to address will be presented in section 1.3. Finally in Section 1.4 a summary is given for the work presented in this dissertation along with an outline of its relevance to the spectroscopic community.

1.2 Optical Pulse Shaping

The time domain signal processing employed in common waveform generators used, for example in modern NMR spectroscopy, is incapable of femtosecond pulse shaping because even the fastest integrated electronic circuitry functions at rates far below the bandwidth of ultrafast laser pulses. As a consequence, the most successful method for shaping ultrafast optical pulses uses spatial masking to modulate the spatially resolved optical spectrum (i.e., in the frequency domain), thereby avoiding the necessity for ultrafast signal modulators. [2] The device employed in this work for spatial masking of the spectrum is a liquid crystal spatial light modulator (SLM). A 4-f zero dispersion optical compressor spectrally disperses the input electric field as illustrated in Figure 1.1 (right side of device), and the computer controlled SLM is placed at the Fourier plane of the compressor to ensure maximum spectral resolution. [56] After the spectrally dispersed field is modulated by the SLM, optical inverse Fourier transform by the symmetric compressor (left side of Figure 1.1) results in a shaped time domain field.

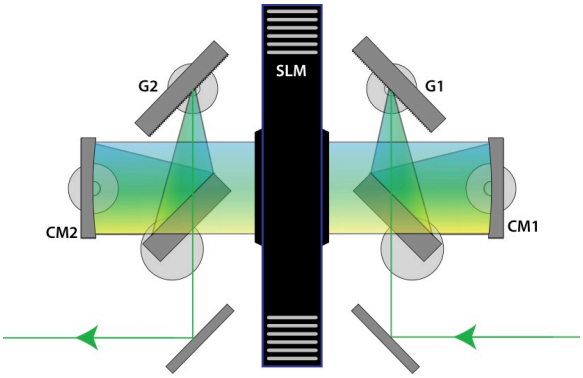

Figure 1.1 An all reflective pulse shaper typically used in this work. The apparatus is comprised of two components: a 4-f zero dispersion pulse compressor and the SLM. The pulse compressor serves to spectrally disperse the time domain input laser pulse. After diffracting off the first grating (G1), the field is collimated by a curved mirror (CM1). For maximum spectral resolution, the SLM is inserted at the Fourier plane. The left side of the pulse compressor, which is the mirror image of the right, simply performs the inverse optical Fourier transform back into the time domain.

SLMs are pixilated devices capable of individually modulating both the amplitude and phase of spectral components of the total field that pass through each pixel. As the pixels have a finite width in Cartesian space and consequently in frequency space, the resolution of a SLM based pulse shaper is ultimately determined by the amount of spectral dispersion achieved by the optical compressor and the number of pixels that can span the spectrum. Pixelation effects in SLMs are a well-quantified phenomena in the literature [2,57] and will be further discussed with respect to two-dimensional electronic spectroscopy in Chapter 2 of this dissertation. Although it is not intended to be a technically correct description of the pulse shaping process, Figure 1.2 illustrates how phase shaping is achieved with an SLM.

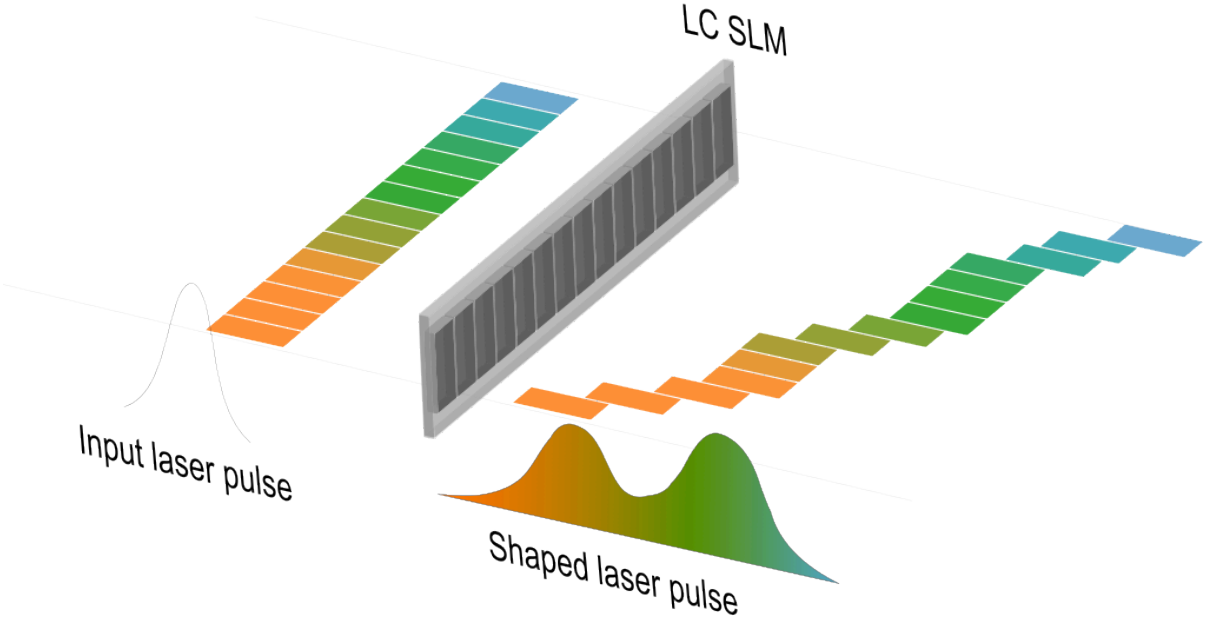

Figure 1.2 Cartoon of optical phase shaping with a pixelated liquid crystal spatial light modulator (SLM): each of the frequency components of the input laser pulse passes through an individually addressable pixel on the SLM. By changing the applied voltage at each pixel the index of refraction is changed, thereby affecting the delay (and thus, relative phase) of the colors passing through each pixel with respect to the others.

In Figure 1.3 is a similar illustration, except that instead of manipulating the phase of the input laser pulse, the amplitude is modulated. Here an amplitude function $A(\omega)$, is defined that is used to parameterize the pulse shaping device (not shown), so that the amplitude of the input spectrum (left of the arrow) is modulated in the frequency domain by the shaping device, resulting in the output spectrum (right of the arrow). Though these illustrations show only phase shaping (Figure 1.2) or only amplitude shaping (Figure 1.3), many pulse shapers (including the SLM used in our lab)

are capable of independently modulating both the amplitude and the phase of an input field.

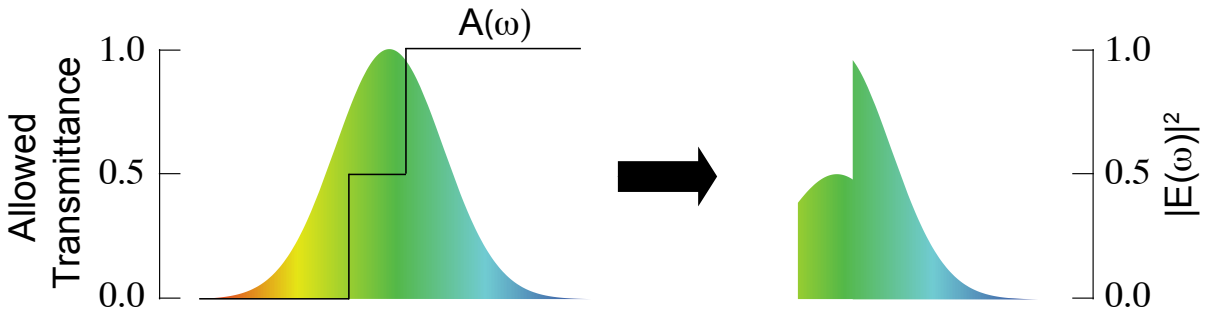

Figure 1.3 Cartoon of amplitude shaping with an SLM. The simple staircase amplitude function, A(ω) has allows 0% transmittance on the red edge of the spectrum, 50 % transmittance in the middle, and 100% transmittance on the blue edge of the spectrum. The arrow represents the amplitude modulation performed by the pulse-shaping device.

1.3 Coherent Control

When a quantum system absorbs light from a laser pulse, the wavefunction $|\psi(t)\rangle$, which is the fundamental descriptor of the system's state at all times, changes in character, reflecting a transfer of energy from the field to the system. This new wavefunction is often not an eigenstate of the excited state Hamiltonian of the system and is called a wavepacket. This wavepacket evolves in time, reflecting constructive and destructive interference of its time-dependent Fourier components. Quite generally, however, the system's excited state wavefunction, whether the probability density evolves in time or not, can be described as a linear superposition of the system's eigenstates:

$$|\psi(t)\rangle = \sum_n c_n e^{-i(E_n t/\hbar - \phi_n)} |\varphi_n\rangle \quad [1.1]$$

Here $|\varphi_n\rangle$ are the system's eigenfunctions with frequencies $E_n/\hbar$, and the c_n and ϕ_n are amplitudes and phases of the constituent eigenfunctions. Coherent control, in its most general form, seeks to exploit the interference phenomena that are intrinsic to quantum mechanical systems to affect a desired outcome by manipulating the phases, ϕ_n, and the amplitudes, c_n, of a quantum system's wavefunction. The two traditional forms of coherent control, Tannor/Rice control [7,8,58] and Brumer/Shapiro control [9,59] share this trait but go about it in conceptually different ways.

Tannor/Rice control has a primarily time domain picture. In their formulation a sequence of femtosecond pulses is used to first excite a wavepacket to the excited state surface. This wavepacket then evolves under the excited state Hamiltonian before being excited (by the second pulse in the sequence) to a third surface or back to the ground state surface thereby affecting a change in product state distribution. In this picture, the amplitudes and phases of the eigenstate components of the wavepacket are manipulated by the interpulse timing, which determines how long each wavepacket evolves under a given Hamiltonian. Figure 1.4 shows a simple example of a Tannor/Rice control scenario in which the timing of the second pulse controls whether the initially excited wavepacket is returned to the initial ground state (A) or sent to evolve on another state (B).

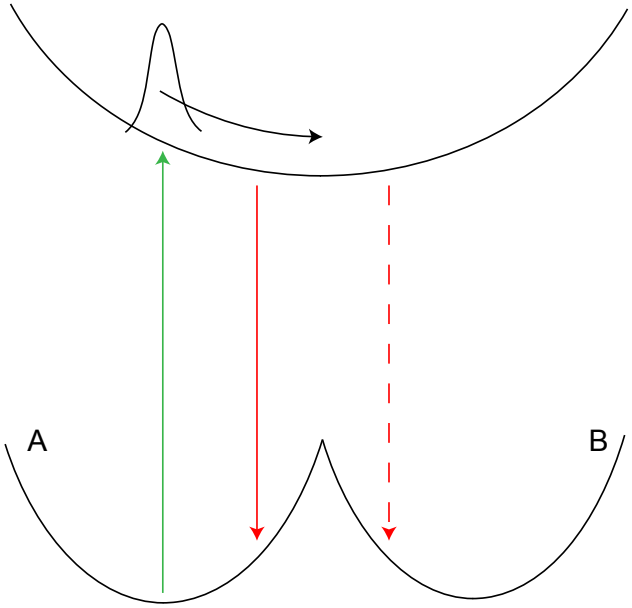

Figure 1.4 Illustration of a simple Tannor/Rice control scheme. The initial laser pulse excites a wavepacket to the excited state surface (green arrow). This wavepacket evolves under the excited state Hamiltonian until the second laser pulse sends the wavepacket back to its initial state A, (solid red) or if the laser pulse is times slightly differently, it will send the wavepacket to state B (dashed red).

In Brumer/Shapiro control, the product state distribution is affected by creating two wavepackets on an excited state surface via two *different, phase-related* pathways. Since two wavepackets are created via two independently adjustable pathways, the phases and amplitudes of the components can also be independently manipulated, allowing for arbitrary control of how the wavepackets interfere. In the two limiting cases, if the two wavepackets are of identical character, they will constructively add, creating four units of population, whereas if they are exactly π out of phase with one another, they will destructively interfere, leaving no population in the excited state.

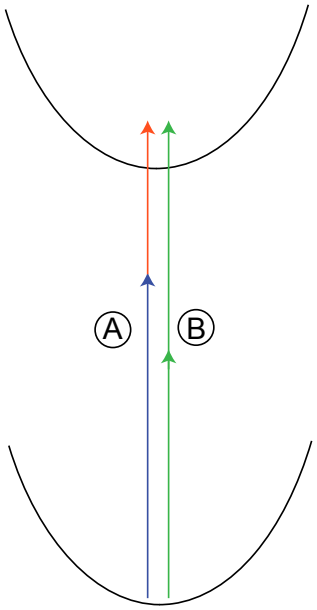

Figure 1.5 Illustration of a Brumer/Shapiro control of a two-photon absorption process. Wavepackets created by paths A and B can be made to constructively or destructively interfere based on independent manipulation of the amplitudes and phases of the component spectral features.

Shown in Figure 1.5 is an illustration of Brumer/Shapiro control for two-photon absorption. Path A and path B create wavepackets of equal energy, however their constituent frequency components are different. By manipulating the phases and amplitudes of these frequency components, the wavepackets created by paths A and B may be made to constructively or destructively interfere.

These methods (both Tannor/Rice and Brumer/Shapiro) are intrinsically multiphoton processes, requiring at least four interactions with the electric field to create an observable. As mentioned previously, recent experimental and theoretical work has shown a third class of coherent control that is a purely linear phenomenon. [39,42,46,47] Theoretical work shows that in this case, it is the initial shape of the wavepacket created and how it subsequently interacts with the quantum

system's environment (rather than an additional perturbation from a laser pulse) that governs the final outcome of the observable. [46,47]

Ultimately, all coherent control schemes are unified by the fact that initially prepared wavepackets are modified by an external field (laser or bath), thereby changing the ensuing molecular dynamics and ultimately affecting experimental observables. This change reflects fundamental information about how energy moves in a quantum system, and it is the ability to directly probe such changes that gives coherent control its unique interrogative power.

1.4 Pulse Shaping as a Spectroscopic Tool

As will be presented in the remainder of this dissertation, optical pulse shaping is a powerful and flexible tool for the investigation of complex photophysics. In Chapter 2, it will be described how pulse shaping can be implemented to easily collect two-dimensional electronic spectra, as demonstrated on Rb vapor sample. [60] In addition, Chapter 2 will discuss calculations undertaken to simulate the distortions to 2D spectra that are resultant of using a pulse shaper as well as the steps that are necessary to minimize them. Chapter 3 will describe work on PbSe quantum dots that employs both open and closed loop methods to attempt to coherently control multiple exciton generation. The methods and results obtained from this work has allowed a refined understanding of what conditions are necessary for coherent control to be an applicable spectroscopic method and revealed some potential limitations of closed loop optimization methods. Chapter 4 describes a series of spectroscopic and coherent

control experiments performed on tetracene thin films. [61] In this case, closed loop optimization techniques guide and inform the study of the singlet fission relaxation process the system undergoes. Finally, Chapter 5 summarizes theoretical work using the tools of time dependent perturbation theory that describes a commonly used coherent control method, sinusoidal spectral phase modulation. The results of these studies begin to bridge the gap separating coherent control and nonlinear spectroscopy communities. Taken as a whole, the use of pulse shaping methods, which allows the ability to regularly and easily collect multidimensional nonlinear spectra and implement open and closed loop coherent control experiments, forms the basis for a class of increasingly sophisticated spectroscopic tools for understanding complex dynamics.

1.4 References Cited

1. S. Mukamel, *Principles of Nonlinear Optical Spectroscopy* (1995).

2. A. M. Weiner, "Femtosecond pulse shaping using spatial light modulators," Rev. Sci. Instrum. **71**, 1929–1960 (2000).

3. A. Weiner, D. Leaird, G. Wiederrecht, and K. Nelson, "Femtosecond pulse sequences used for optical manipulation of molecular motion," Science **247**, 1317 (1990).

4. D. Yelin, D. Meshulach, and Y. Silberberg, "Adaptive femtosecond pulse compression," Opt. Lett **22**, 1793–1795 (1997).

5. E. Zeek, K. Maginnis, S. Backus, U. Russek, M. Murnane, G. Mourou, H. Kapteyn, and G. Vdovin, "Pulse compression by use of deformable mirrors," Opt. Lett **24**, 493 (1999).

6. T. Brixner, M. Strehle, and G. Gerber, "Feedback-controlled optimization of

amplified femtosecond laser pulses," Appl Phys B-Lasers O **68**, 281–284 (1999).

7. D. J. Tannor and S. A. Rice, "Control of selectivity of chemical reaction via control of wave packet evolution," J Chem Phys **83**, 5013 (1985).

8. D. Tannor, R. Kosloff, and S. Rice, "Coherent pulse sequence induced control of selectivity of reactions - exact quantum-mechanical calculations," J Chem Phys **85**, 5805–5820 (1986).

9. P. Brumer and M. Shapiro, "Control of unimolecular reactions using coherent-light," Chem. Phys. Lett. **126**, 541–546 (1986).

10. M. Shapiro, "A Uniform Theory of Preparation, Dissociation, and Product Formation in the Decay of Overlapping Resonances," J. Phys. Chem. A **102**, 9570–9576 (1998).

11. A. Zewail, "Laser selective chemistry 3-is it possible.," Physics Today **November**, 1–8 (1980).

12. F. F. Crim, "Selective excitation studies of unimolecular reaction dynamics," Annual Review of Physical Chemistry **35**, 657–691 (1984).

13. N. Bloembergen and A. H. Zewail, "Energy redistribution in isolated molecules and the question of mode-selective laser chemistry revisited. New experiments on the dynamics of collisionless energy redistribution in molecules possibilities for laser-selective chemistry with subpicosecond pulses," The Journal of Physical Chemistry **88**, 5459–5465 (1984).

14. A. Assion, T. Baumert, M. Bergt, T. Brixner, B. Kiefer, V. Seyfried, M. Strehle, and G. Gerber, "Control of chemical reactions by feedback-optimized phase-shaped femtosecond laser pulses," Science **282**, 919–922 (1998).

15. R. J. Levis, G. M. Menkir, and H. Rabitz, "Selective bond dissociation and rearrangement with optimally tailored, strong-field laser pulses.," Science **292**, 709–713 (2001).

16. N. H. Damrauer, C. Dietl, G. Krampert, S. H. Lee, K. H. Jung, and G. Gerber, "Control of bond-selective photochemistry in CH2BrCl using adaptive femtosecond pulse shaping," The European Physical Journal D - Atomic, Molecular and Optical Physics **20**, 71–76 (2002).

17. D. Cardoza, M. Baertschy, and T. Weinacht, "Understanding learning control of molecular fragmentation," Chemical Physics Letters **411**, 311–315 (2005).

18. Y. Silberberg and D. Meshulach, "Coherent quantum control of two-photon transitions by a femtosecond laser pulse," Nature **396**, 239–242 (1998).

19. D. Meshulach and Y. Silberberg, "Coherent quantum control of multiphoton transitions by shaped ultrashort optical pulses," Physical Review A **60**, 1287–1292 (1999).

20. T. Brixner, N. Damrauer, and G. Gerber, *Femtosecond Quantum Control* (2001), Vol. 46, pp. 1–54.

21. N. Dudovich, B. Dayan, Gallagher Faeder SM, and Y. Silberberg, "Transform-limited pulses are not optimal for resonant multiphoton transitions.," Phys. Rev. Lett. **86**, 47–50 (2001).

22. D. Oron, N. Dudovich, D. Yelin, and Y. Silberberg, "Quantum control of coherent anti-Stokes Raman processes," Physical Review A **65**, 043408 (2002).

23. N. Dudovich, D. Oron, and Y. Silberberg, "Single-pulse coherently controlled nonlinear Raman spectroscopy and microscopy," Nature **418**, 512–514 (2002).

24. T. Brixner, N. Damrauer, B. Kiefer, and G. Gerber, "Liquid-phase adaptive femtosecond quantum control: Removing intrinsic intensity dependencies," J Chem Phys **118**, 3692–3701 (2003).

25. T. Polack, D. Oron, and Y. Silberberg, "Control and measurement of a non-resonant Raman wavepacket using a single ultrashort pulse," Chem Phys **318**, 163–169 (2005).

26. M. A. Montgomery, R. R. Meglen, and N. H. Damrauer, "General method for the dimension reduction of adaptive control experiments," J. Phys. Chem. A **110**, 6391–6394 (2006).

27. M. A. Montgomery and N. H. Damrauer, "Elucidation of control mechanisms discovered during adaptive manipulation of [ru(dpb) 3](pf 6) 2emission in the solution phase," J. Phys. Chem. A **111**, 1426–1433 (2007).

28. C. Bardeen, Q. Wang, and C. Shank, "Selective excitation of vibrational wave packet motion using chirped pulses.," Phys. Rev. Lett. **75**, 3410–3413 (1995).

29. C. Bardeen, Q. Wang, and C. Shank, "Femtosecond chirped pulse excitation of vibrational wave packets in LD690 and bacteriorhodopsin," J. Phys. Chem. A **102**, 2759–2766 (1998).

30. C. Bardeen, V. Yakovlev, J. Squier, and K. Wilson, "Quantum control of population transfer in green fluorescent protein by using chirped femtosecond pulses," J Am Chem Soc **120**, 13023–13027 (1998).

31. J. Cao, C. Bardeen, and K. Wilson, "Molecular pi pulses: Population inversion with positively chirped short pulses," J Chem Phys **113**, 1898–1909 (2000).

32. R. Judson and H. Rabitz, "Teaching lasers to control molecules," Phys. Rev. Lett. **68**, 1500–1503 (1992).

33. J. Herek, W. Wohlleben, R. Cogdell, D. Zeidler, and M. Motzkus, "Quantum control of energy flow in light harvesting," Nature **417**, 533–535 (2002).

34. J. Savolainen, R. Fanciulli, N. Dijkhuizen, A. L. Moore, J. Hauer, T. Buckup, M. Motzkus, and J. L. Herek, "Controlling the efficiency of an artificial light-harvesting complex," P Natl Acad Sci Usa **105**, 7641–7646 (2008).

35. W. Wohlleben, T. Buckup, J. Herek, and M. Motzkus, "Coherent control for spectroscopy and manipulation of biological dynamics," Chemphyschem **6**, 850–857 (2005).

36. J. Hauer, T. Buckup, and M. Motzkus, "Enhancement of molecular modes by electronically resonant multipulse excitation: Further progress towards mode selective chemistry," J Chem Phys **125**, 061101 (2006).

37. J. Hauer, T. Buckup, and M. Motzkus, "Quantum control spectroscopy of vibrational modes: Comparison of control scenarios for ground and excited states in beta-carotene," Chem Phys **350**, 220–229 (2008).

38. T. Buckup, J. Hauer, C. Serrat, and M. Motzkus, "Control of excited-state population and vibrational coherence with shaped-resonant and near-resonant excitation," J Phys B-At Mol Opt **41**, 074024 (2008).

39. P. van der Walle, M. Milder, and L. Kuipers, "Quantum control experiment reveals solvation-induced decoherence," Proceedings of the National Academy of Sciences (2009).

40. P. Brumer and M. Shapiro, "One photon mode selective control of reactions by rapid or shaped laser pulses: An emperor without clothes?," Chemical Physics **139**, 221–228 (1989).

41. V. I. Prokhorenko, A. M. Nagy, and R. J. Dwayne Miller, "Coherent control of the population transfer in complex solvated molecules at weak excitation. An

experimental study," J Chem Phys **122**, 184502 (2005).

42. V. Prokhorenko, A. Nagy, S. Waschuk, and L. Brown, "Coherent control of retinal isomerization in bacteriorhodopsin," Science (2006).

43. M. P. A. Branderhorst, P. Londero, P. Wasylczyk, C. Brif, R. L. Kosut, H. Rabitz, and I. A. Walmsley, "Coherent control of decoherence.," Science **320**, 638–643 (2008).

44. M. Joffre, "Comment on "Coherent Control of Retinal Isomerization in Bacteriorhodopsin,"" Science **317**, 453b–453b (2007).

45. V. I. Prokhorenko, A. M. Nagy, S. A. Waschuk, L. S. Brown, R. R. Birge, and R. J. Dwayne Miller, "Response to comment on "Coherent control of retinal isomerization in bacteriorhodopsin,"" Science **317**, 453c–453c (2007).

46. G. Katz, M. A. Ratner, and R. Kosloff, "Control by decoherence: weak field control of an excited state objective," New J. Phys. **12**, 015003 (2010).

47. M. Spanner, C. A. Arango, and P. Brumer, "Communication: Conditions for one-photon coherent phase control in isolated and open quantum systems," J Chem Phys **133**, 151101 (2010).

48. J. White, B. Pearson, and P. Bucksbaum, "Extracting quantum dynamics from genetic learning algorithms through principal control …," J. Phys. B (2004).

49. D. Cardoza, C. Trallero-Herrero, F. Langhojer, H. Rabitz, and T. Weinacht, "Transformations to diagonal bases in closed-loop quantum learning control experiments.," The Journal of Chemical Physics **122**, 124306 (2005).

50. M. A. Montgomery, R. R. Meglen, and N. H. Damrauer, "General method for reducing adaptive laser pulse-shaping experiments to a single control variable," J. Phys. Chem. A **111**, 5126–5129 (2007).

51. D. G. Kuroda, C. P. Singh, Z. Peng, and V. D. Kleiman, "Mapping excited-state dynamics by coherent control of a dendrimer's photoemission efficiency.," Science **326**, 263–267 (2009).

52. B. Amstrup, R. J. Carlson, A. Matro, and S. A. Rice, "Use of pulse shaping to control the photodissociation of a diatomic molecule: preventing the best from being the enemy of the good," The Journal of Physical Chemistry **95**, 8019–8027 (1991).

53. T. Hornung, M. Motzkus, and R. de Vivie-Riedle, "Teaching optimal control theory to distill robust pulses even under experimental constraints," Physical Review A

65, (2002).

54. M. A. Montgomery and N. H. Damrauer, "A convenient method to simulate and visually represent two-photon power spectra of arbitrarily and adaptively shaped broadband laser pulses," New J. Phys. **11**, 105053 (2009).

55. M. A. Montgomery, E. M. Grumstrup, and N. H. Damrauer, "Fourier transform spectroscopies derived from amplitude or phase shaping of broadband laser pulses with applications to adaptive control," J Opt Soc Am B **27**, 2518–2533 (2010).

56. A. Prakelt, M. Wollenhaupt, A. Assion, C. Horn, C. Sarpe-Tudoran, M. Winter, and T. Baumert, "Compact, robust, and flexible setup for femtosecond pulse shaping," Rev. Sci. Instrum. **74**, 4950–4953 (2003).

57. J. Vaughan, T. Feurer, K. Stone, and K. Nelson, "Analysis of replica pulses in femtosecond pulse shaping with pixelated devices," Opt Express **14**, 1314–1328 (2006).

58. D. Tannor, "Coherent pulse sequence control of product formation in chemical reactions," Advances in chemical physics (1988).

59. M. Shapiro and P. Brumer, "Laser control of product quantum state populations in unimolecular reactions," J Chem Phys **84**, 4103–4104 (1986).

60. E. M. Grumstrup, S.-H. Shim, M. A. Montgomery, N. H. Damrauer, and M. T. Zanni, "Facile collection of two-dimensional electronic spectra using femtosecond pulse-shaping technology," Opt Express **15**, 16681–16689 (2007).

61. E. M. Grumstrup, J. C. Johnson, and N. H. Damrauer, "Enhanced triplet formation in polycrystalline tetracene films by femtosecond optical-pulse shaping.," Phys. Rev. Lett. **105**, 257403 (2010).

CHAPTER 2

OPTICAL PULSE SHAPING FOR TWO-DIMENSIONAL ELECTRONIC SPECTROSCOPY

2.1 Introduction

Two-dimensional electronic spectroscopy (2DE) is a powerful technique used to study a wide range of phenomena in biology, chemistry, and physics. By correlating transition dipoles at two frequencies and with time resolution, 2DE can provide information about chromophores and their environments such as bath-induced relaxation [1, 2] and energy transfer phenomena [3, 4] that are inaccessible to conventional methods because of the technique's sensitivity to phase and coherence information. Experimentally, 2DE can be implemented in a variety of configurations, as sketched in Figure 2.1. The predominant technique for collecting 2D spectra uses a "box-car" type geometry (Figure 2.1a) to spatially separate the phase matched polarization of the sample induced by the three interactions with the electric field. [1, 5, 6] This method is by far the most widespread for collection of 2DE spectra due to its background-free signal detection and overall flexibility.

Nevertheless, there remain several barriers to ubiquitous implementation of 2DE spectroscopy for the study of optical chromophores. The apparatus using a non-collinear geometry is complex, requiring four balanced interferometric delay lines with path lengths

that vary less than a small fraction of the excitation wavelength to ensure phase stability. This requirement often necessitates the use of stabilization techniques. [7-10] Another difficulty associated with the box-car geometry is that absorptive spectra must be determined by separately measuring and correctly adding the signals resultant from rephasing and nonrephasing Liouville pathways since they are emitted in different directions.

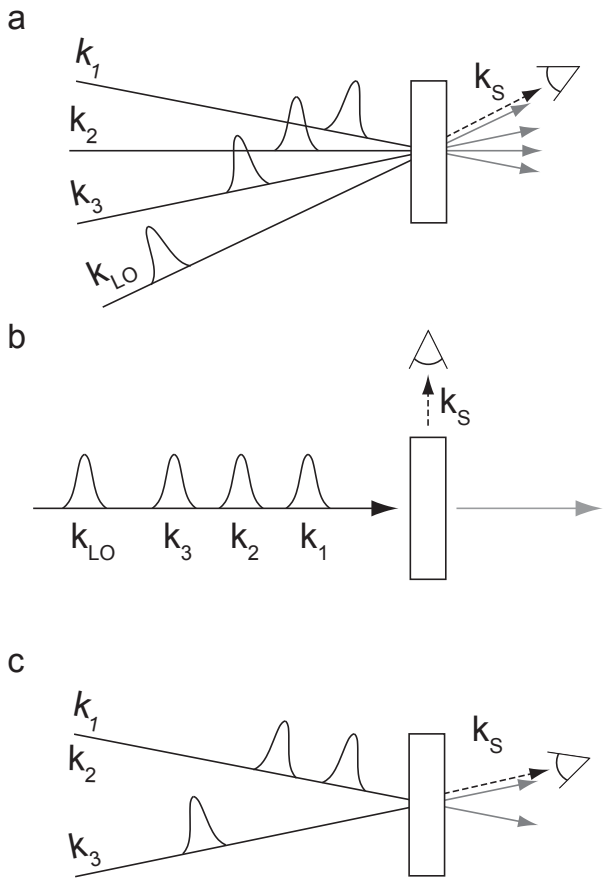

Figure 2.1 Methods for collecting 2D spectra. The k_n are the wavevectors of the excitation pulses and k_s is the wavevector of the emitted signal. (a) A boxcar type of geometry in which all four beams propagate at different angles. (b) An entirely collinear pulse sequence in which fluorescence is collected orthogonally to the beam path. (c) The partially collinear geometry employed here in which two "pump" pulses are followed by an off axis "probe" pulse which is then spectrally resolved.

In efforts to reduce the complexity of collecting 2DE spectra, several approaches have been implemented that maintain the required high phase stability between individual pulses while simplifying the experimental apparatus. Completely collinear geometries (Figure 2.1b) in which all excitation pulses have the same wave vector have been employed, however, because the desired signal is also emitted in the same direction, detection of the field emitted by the third order polarization becomes difficult since this signal is much smaller than the background from the excitation pulses. For this reason, the 2DE spectra collected in a fully collinear geometry using phase cycling [11, 12] and phase modulation schemes [13] have been restricted to fluorescent chromophores, thereby allowing detection of population created by the interaction of a fourth field with the third order polarization. Another technique uses a two-dimensional pulse shaper to delay the excitation pulses with respect to each other, allowing the delay to be controlled and easily maintaining interferometric stabilization while still maintaining the advantages of a box-car geometry. However, few groups have access to these specialized instruments and diffractive optics are still necessary for creating the spatially separated beams. [14]

One solution to the difficulties encountered in these implementations is to use a partially collinear geometry similar to a “pump-probe” measurement. [5, 15] In this case (Figure 2.1c), the system interacts twice with a “pump” beam comprised of a collinear phase locked pulse pair. The third interaction occurs with the “probe” beam, and the signal is radiated along this same wavevector, with the probe beam itself acting to heterodyne the radiated signal. [15] The most salient advantages of this geometry are a dramatic simplification of the apparatus used to collect the 2D spectra and automatic correct addition of the phasing and nonrephasing signals since they are simultaneously detected.

The partially collinear geometry can be implemented using conventional optics as demonstrated by DeFlores, et al. in a publication released simultaneously with this work. [16, 17] However, the significant advantage is not realized until the partially non-collinear geometry is combined with a pulse shaper to produce the phase locked pulse pairs. When this is done, as is presented here and in the originally published work [16], the collection of 2DE spectra is dramatically simplified to the point that it becomes optically comparable to the implementation of a standard pump-probe experiment. Since the pulse pair is produced with a pulse shaper, each pulse travels exactly the same path and sees identical optics, making the required phase stability between pulses an intrinsic property of the apparatus. Furthermore, this implementation opens up avenues of greater flexibility within 2DE spectroscopy including facile collection of highly non-degenerate 2DE spectra [18, 19], implementation of pulse shaping to affect peak intensities [20], or examining coherent control solutions with 2DE spectroscopy [21].

Despite these advantages, there are several drawbacks to the method. The desired third order signal field is radiated in the same direction as the third excitation beam, requiring phase cycling or mechanical chopping to eliminate undesired background signals. Furthermore, since the third excitation field acts to self-heterodyne the radiated field, the intensity of the local oscillator cannot be independently adjusted, eliminating a powerful tool for maximizing the signal to noise ratio. [22] Perhaps the most consequential difficulties, however, are those associated with the use of a pulse shaper to produce the pulse pairs. If a spatial light modulator (SLM) is used (as was done in this work), pixelation effects can generate spurious pulses, leading to dramatic distortions to the collected 2D spectrum.

Despite these difficulties, implementation of 2DE spectroscopy by using a pulse shaper in a partially non-collinear geometry remains a promising tool. This work's initial demonstration of the method in the visible spectrum and subsequent analysis of pixelation effects, provide a basis for further expansion of this powerful technique. This chapter is arranged as follows: A brief overview of the detected signals and principles of 2DE will be followed by a description of pulse pair generation using a pulse shaper. Next, data will be presented that show 2DE spectra collected for Rb vapor using an SLM. Finally, distortion effects will be theoretically examined for a model system using density matrix theory and the steps necessary for mitigation of these distortions will be outlined.

2.2 Two-Dimensional Electronic Spectroscopy

2DE is at least a third order technique meaning that the resultant signal is a consequence of, at minimum, three interactions of the system with an input electric field. In the case of short pulse excitation in which the system polarization is produced by only one interaction per laser pulse, three distinct pulses are required (see Figure 2.2).

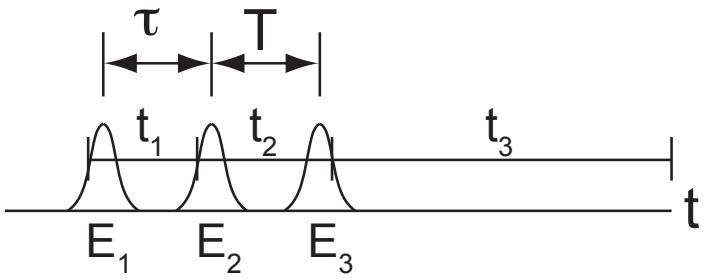

Figure 2.2 Time variables and parameters used in this manuscript: τ is the interval between the first (E_1) and second (E_2) pulse, both contained in the "pump" beam. The parameter T defines the interval between the second (E_2) and third (E_3, probe) pulse. Intervals between interactions with the field are defined as t_3, t_2, and t_1.

The system's response to the three interactions with the field can be described by a response function, $R(t_1, t_2, t_3)$ which is a sum of rephasing and nonrephasing components. [6, 23]

$$R(t_1, t_2, t_3) = R^{(R)}(t_1, t_2, t_3) + R^{(NR)}(t_1, t_2, t_3) \quad [2.1]$$

Each of these components are comprised of Liouville pathways describing specific light matter interactions such as stimulated emission, ground state bleach, and excited state absorption. [6, 23] In the partially non-collinear geometry employed in this work, the first two phase-locked pulses are produced and temporally controlled by the pulse shaper and the spectrum detected in the phase-matched direction is given by:

$$S(\omega_3, T, \tau) \propto \left|\tilde{\epsilon}_3(\omega_3) + i\omega_3\left[P_3^{(1)}(\omega_3) + P_{2D}^{(3)}(\omega_3, T, \tau) + P_{PP1}^{(3)}(\omega_3, T, \tau) + P_{PP2}^{(3)}(\omega_3, T, \tau)\right]\right|^2 \quad [2.2]$$

where $\tilde{\epsilon}_3$ is the complex, frequency domain probe field, $P_3^{(1)}$ is the free-induction decay from the interaction with the probe pulse, $P_{2D}^{(3)}$ is the desired third order polarization of the sample, and $P_{PP1}^{(3)}$ and $P_{PP2}^{(3)}$ are the pump-probe polarizations resulting from pulses E_1 and E_2, respectively. The desired third order induced polarization, $P_{2D}^{(3)}$, is the Fourier transform of the triple convolution of the system response function (Equation 2.1) with the electric field,

$$P_{2D}^{(3)}(\omega_3, T, \tau) = \int_{-\infty}^{\infty} dt\, P_{2D}^{(3)}(t, T, \tau) e^{-i\omega_3 t} \quad [2.3]$$

$$P_{2D}^{(3)}(t, T, \tau) = \int_0^{\infty} dt_3 \int_0^{\infty} dt_2 \int_0^{\infty} dt_1\, \boldsymbol{E}(t + \tau + T - t_3 - t_2 - t_1)\boldsymbol{E}(t + T - t_3 - t_2)\boldsymbol{E}(t - t_3) \times R(t_1, t_2, t_3), \quad [2.4]$$

where, $\boldsymbol{E}(t) = \tilde{E}_1(t+\tau+T) + \tilde{E}_2(t+T) + \tilde{E}_3(t) + c.c.$

To recover a 2DE spectrum, a series of frequency (ω_3) resolved signals (Equation 2.2) is collected for τ values satisfying the Nyquist limit of the studied system frequency. This array of data is then Fourier transformed with respect to τ at a fixed value of T. Thus the two frequency axes of the 2D spectrum correspond to ω_3 and ω_τ. The first of these frequencies (ω_3) is very simply recovered by frequency resolving the detected signal while the second of these frequencies (ω_τ) is indirectly detected by the Fourier transform procedure outlined above. It should be noted that the three other components ($P_3^{(1)}$, $P_{PP1}^{(3)}$, and $P_{PP2}^{(3)}$) of the nonlinear polarization are readily removed from the recovered signal by phase cycling schemes or by simply noting they appear at different frequencies combinations in the 2D spectrum as was done in the work presented here. [6, 24, 25]

2.3 Pulse Pair Generation with a Spatial Light Modulator

To generate an electric field composed of a pair of identical pulses, a spatial light modulator (SLM) is used to modulate the spectral amplitude and phase of a broadband laser pulse[1]. This is done by specification of a transfer function, $R(\omega,\tau)$, that maps the input frequency domain laser pulse, $\tilde{\epsilon}_{in}(\omega)$, onto the desired pulse shape, $\tilde{\epsilon}_{out}(\omega,\tau)$, whose inverse Fourier transform is a pulse pair with a well defined temporal separation, τ.

$$\tilde{\epsilon}_{out}(\omega,\tau) = R(\omega;\tau)\tilde{\epsilon}_{in}(\omega) \qquad [2.5]$$

In the frequency domain, modulations to the amplitude are produced by multiplication of the input electric field with an amplitude function whose range spans 0 (0% transmittance)

[1] In addition to spatial light modulators, acousto-optic light modulators can be used for the necessary pulse shaping. [18, 26] These devices have none of the pixelation problems discussed below.

to 1 (100% transmittance). The spectral phase function applied by the SLM is added to the spectral phase of the unshaped, input electric field, $\tilde{\epsilon}_{in}$. The complex transfer function of a pair of identical laser pulses is given by:

$$R(\omega;\tau) = \frac{1}{2}\left[e^{i\omega\tau} + 1\right] \quad [2.6]$$

Inverse Fourier transform yields the real, time domain electric field $\boldsymbol{E}(t,\tau)$:

$$\boldsymbol{E}(t,\tau) \propto \frac{1}{4}\left(\tilde{E}(t) + \tilde{E}(t-\tau)\right) + c.c. \quad [2.7]$$

where the temporal amplitude $\tilde{E}(t) = A(t)e^{i(-\omega_0 t+\varphi(t))}$, is defined by the slowly varying, real envelope $A(t)$, carrier frequency ω_0 and temporal phase $\varphi(t)$. The transfer function, $R(\omega;\tau)$ can be separated into amplitude and phase components shown in Equations 2.8 and 2.9, respectively,

$$a(\omega;\tau) = \left|\cos\left(\frac{\omega\tau}{2}\right)\right| \quad [2.8]$$

$$p(\omega;\tau) = \frac{\omega\tau}{2} + \left(\frac{\pi}{2} - \frac{\pi}{2}sgn\left[\cos\left(\frac{\omega\tau}{2}\right)\right]\right) \quad [2.9]$$

where *sgn* specifies the sign operator. The first term of Equation 2.9 simply shifts the pulse pair in time, however the second term is necessary to account for the amplitude component of the transfer function (Equation 2.8), which can only take meaningful values between 0 and 1 (instead of the necessary -1 to +1). For this reason, a phase shift of π is necessary when $\cos\left(\frac{\omega\tau}{2}\right) < 0$. Since the SLM is a pixelated device that can only apply discrete phase and amplitude values for each of the individual pixels, Equations 2.8 and 2.9 are rewritten:

$$a(\omega_n;\tau) = \left|\cos\left(\frac{\omega_n\tau}{2}\right)\right| \quad [2.10]$$

$$p(\omega_n;\tau) = \frac{\omega_n \tau}{2} + \left(\frac{\pi}{2} - \frac{\pi}{2} sgn\left[\cos\left(\frac{\omega_n \tau}{2}\right)\right]\right) \quad [2.11]$$

where, the frequency is now discretely indicated by the center frequency of the light passing though pixel n. The pixelation of the phase and amplitude functions leads to non-ideal pulse shaping and will be examined in Section 2.7 in the context of this work. [27, 28]

2.4 **Experimental**

Shown in Figure 2.3 is a sketch of the experimental apparatus used in this work. The broad-band ultrashort laser source (~800 nm ± 17 nm; ~50 fs temporal FWHM; 1 KHz; ~900 μJ/pulse) used in these experiments is a Quantronix Odin multi-pass amplifier seeded by a KM labs MTS mini oscillator. The 'pump' portion of the pulse train was coupled into a home-built 4f zero-dispersion pulse shaper. A pixelated dual-layer computer-controlled SLM (CRI Inc; SLM-640) was placed at the Fourier plane of the pulse shaper and calibrated with in-house procedures. Though our SLM has 640 individually addressable pixels, only 130 were used to span the laser spectrum. Phase and amplitude functions (Equations 2.10 and 2.11) applied to the SLM mask produced variably spaced, collinear pulse pairs. The resulting shaped beam (350 nJ/pulse) was focused with a 300 mm lens into a sealed Pyrex one-inch path length Rb gas cell with ~ 20 mTorr of He buffer gas (Triad Technology, Inc.). The cell was heated to ~ 135±2°C to increase the Rb vapor pressure.

The 'probe' laser beam was directed onto a computer-driven translation stage providing experimental control of the population time (T). Approximately 15 nJ/pulse was focused with a 100 mm lens into the sample at a small angle (~5°) with respect to the

'pump' pulse pair. The signal propagated collinearly with the probe beam and was dispersed with a 1200 g/mm grating in a commercial spectrometer (Acton; Spectrapro 2300i). The dispersed signal was collected on a 1024 pixel photo diode line camera (Spectronic Devices, Ltd; S3904-1024) synchronized with the pulse train, and data were recorded with programs written in house using Labview. Spectra were collected with and without the pump beam and the change in absorption calculated ($\Delta A = A_{\text{pump off}} - A_{\text{pump on}}$).

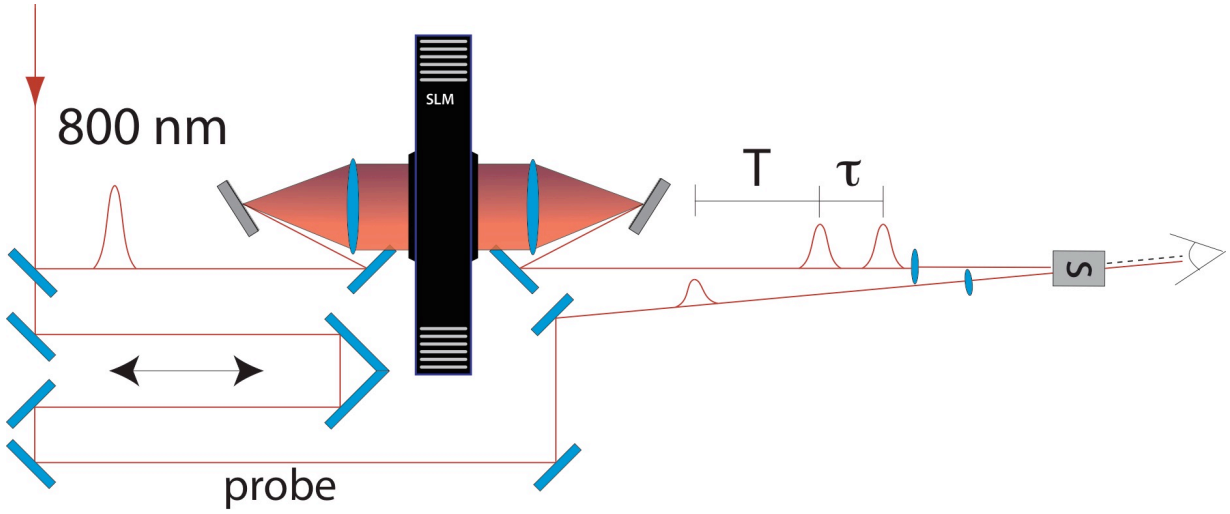

Figure 2.3 Schematic of apparatus employed to collect two-dimensional electronic spectra. Pump and probe beams are split by a beamsplitter. The "probe" beam is coupled onto a mechanical delay line that controls the population time, T. The "pump" beam is dispersed in a 4-f, zero dispersion optical compressor with a dual mask SLM placed at the Fourier plane. The SLM is parameterized with the amplitude and phase functions used to create a pulse pair separated by τ before the beam is focused onto the sample.

2.5 Results

To demonstrate our method, we collected 2DE spectra of atomic rubidium vapor. Rb vapor has atomic transitions at 794.76 ($5P_{1/2} \leftarrow 5S_{1/2}$ and 780.03 nm ($5P_{3/2} \leftarrow 5S_{1/2}$) and has been used to test other 2DE methodologies as it is well characterized, spectrally convenient, and has narrow linewidths. [12-14] Shown in Figure 2.4 is the time domain difference in absorption (given by Equation 2.12) measured at 780 nm as a function of the τ delay,

incremented in 1 fs intervals with the pulse shaper by stepping the E_1 pulse backward in time.

$$\begin{aligned} A(\omega_3, T, \tau) \\ \propto -Log\Big\{\Big|\tilde{\epsilon}_3(\omega_3) \\ + i\omega_3\Big[P_3^{(1)}(\omega_3) + P_{2D}^{(3)}(\omega_3, T, \tau) + P_{PP1}^{(3)}(\omega_3, T, \tau) + P_{PP2}^{(3)}(\omega_3, T, \tau)\Big]\Big|^2 \\ - \Big|\tilde{\epsilon}_3(\omega_3) + i\omega_3\Big[P_3^{(1)}(\omega_3)\Big]\Big|^2\Big\} \end{aligned} \qquad [2.12$$

The signal oscillates with a period of ~2.6 fs (see inset), set by the transition frequencies of the atomic system. These fast oscillations sit on a background that oscillates with a period of ~140 fs, corresponding to the difference frequency between the 795 and 780 nm transitions. This slow oscillation stems from the $P_{PP1}^{(3)}$ and $P_{PP2}^{(3)}$ contribution to the signal and is measured in a standard pump-probe experiment. If desired, they can be straightforwardly removed from the time domain data by phase cycling the relative phase between pulses E_1 and E_2 during the experiment.

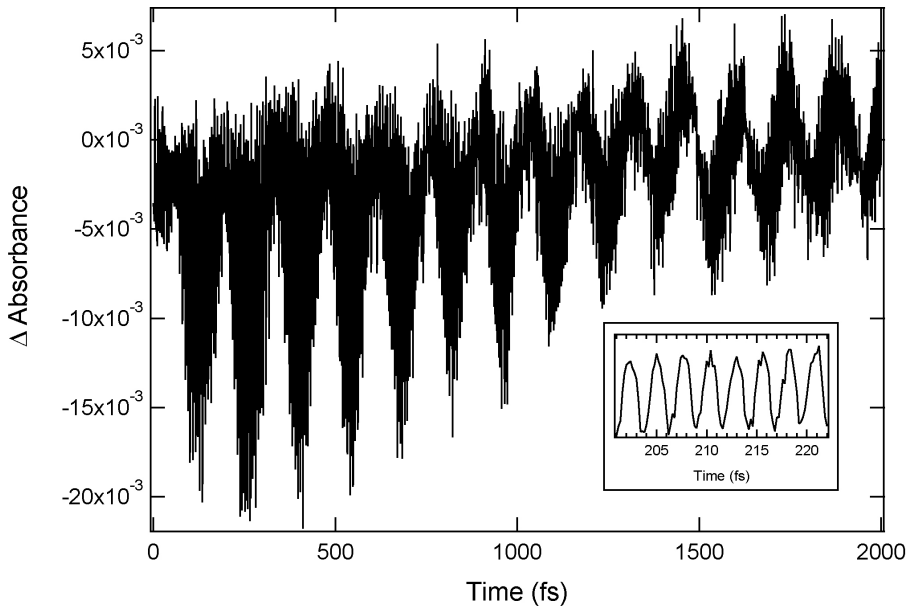

Figure 2.4 Time domain data, $A(\omega_3, T, \tau)$, collected at λ_3 = 780 nm and T = 1.0 ps. Fast oscillations of the signal (see inset) are superimposed on slow modulation of transient absorption signal.

The two frequency axes of the 2DE spectrum correspond to ω_3, which reflects the frequency resolved signal detected with the spectrometer, and the indirectly detected frequency ω_τ, which is recovered from the data set after Fourier transform with respect to τ. The real part of the 2DE spectrum is shown in Figure 2.5 and exhibits diagonal peaks and cross peaks as expected. The diagonal peaks appear at $\lambda_\tau = \lambda_3 =$ 780 and 795 nm ($\lambda_3 = 2\pi c/\omega_3, \lambda_\tau = 2\pi c/\omega_\tau$) and reflect Liouville pathways that sample only one of the two transitions. The cross peaks correlate the two diagonal peaks and are created by pathways that sample both fundamental transitions. [6, 23] The oscillator strengths of the transitions as well as the spectral amplitudes of the excitation laser pulses determine the intensity of each of the peaks.

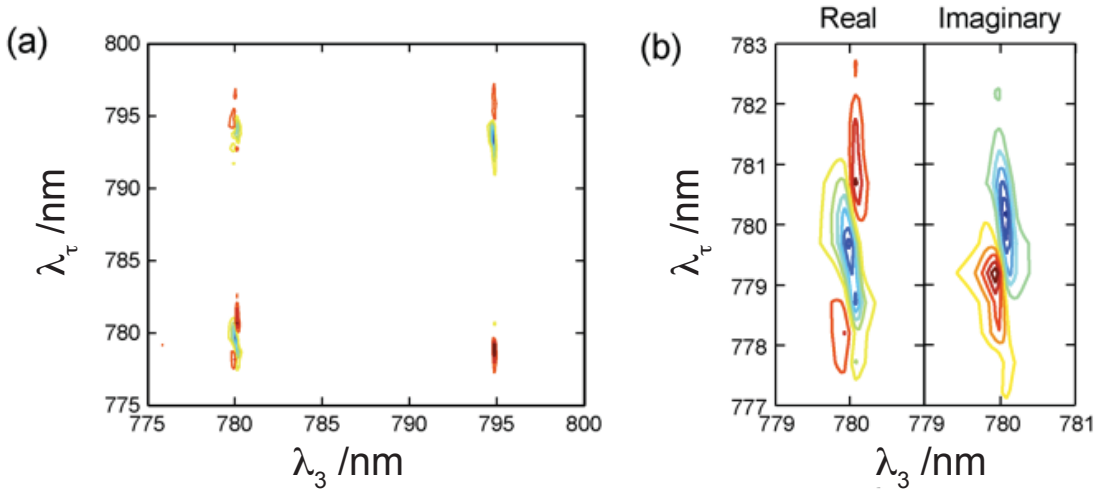

Figure 2.5 (a) Real 2D spectrum of Rb vapor. (b) Detail of the peak at $\lambda_\tau = \lambda_3 =$ 780 nm.

Shown in Figure 2.5b are the real and imaginary parts of the collected 2D spectrum for the diagonal peak at $\lambda_\tau = \lambda_3 =$ 780 nm shown in an expanded plot. The linewidths differ along λ_τ and λ_3, which is expected under our experimental conditions. The width of the peaks along the λ_3 axis is dominated by the spectrometer resolution of 0.65 nm as the Doppler broadened natural linewidth of the atomic absorption transition is only $\sim$ 0.001

nm. The width along the λ_τ axis is given by the natural linewidth of the system convolved with the spectral resolution of the Fourier transform, $\sim 2/\tau^{max}$ where τ^{max} is the largest τ delay. For the spectra shown in Figure 2.5, the time domain signal, $S(\omega_3, T, \tau)$, was convolved with a cosine apodization function that decays to zero at 2.0 ps, further broadening the peak along λ_τ. This convolution was necessary to minimize signal artifacts due to non-ideal pulse pair generation from the SLM as is discussed in more detail below.

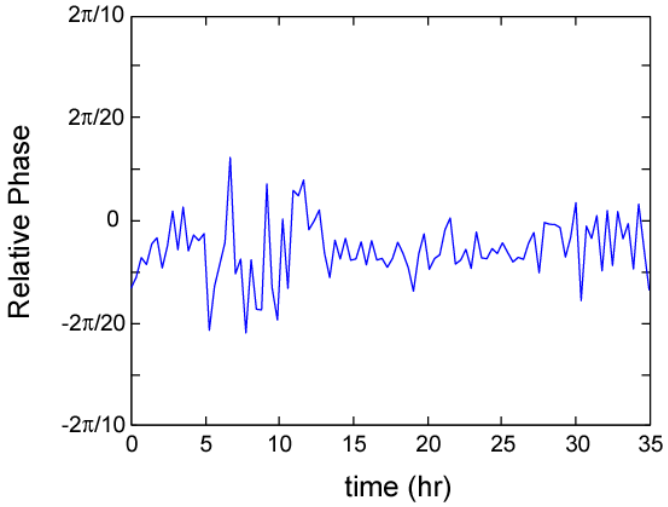

Figure 2.6 Phase stability as measured over 35 hours by repeatedly scanning the signal from t_1= 200 – 220 fs. Phase drift was measured to be λ/67.

The phase stability of the excitation pulses, critical to the implementation of 2DE spectroscopy, is an intrinsic property of pulse pair generation with a SLM. To demonstrate this, we measured the phase stability of the pulse pair generated by the SLM by scanning τ = 200 fs to τ = 224 fs in 0.2 fs steps every 21 minutes over the course of 35 hours. The time-domain data were then Fourier transformed to determine the phase angle. Shown in Figure 2.6 is the measured phase over the course of this period with no stabilization procedures in place. From this plot, the calculated phase stability was determined to be λ/67, which is more than sufficient to generate high quality 2DE spectra. This number

compares to phase drift of λ/100 typical of diffractive optics and λ/250 with HeNe interferometry; measurements made over the course of ~5 hours. [7, 8, 10] It should be noted that no effort was taken to ensure a stable apparatus beyond standard practice for a laser lab, however with greater attention to temperature stabilization and shorter experimental times, the phase stability would be expected to greatly improve.

2.6 Discussion

The pulse shaping method employed here produces pulses with excellent intrinsic phase stability and accurate time resolution because the first two excitation pulses are collinear and thus follow the same optical path. As has been long pointed out, this is a practical advantage over 2DE spectroscopy with non-collinear pulses because the lengths of individual optical paths must not drift more than a fraction of the wavelength requiring extensive stabilization techniques. [5] In the implementation presented here, the only major potential source of phase instability is spatial drift of the excitation beam into the pulse shaper causing changes to the SLM calibration. If such a drift occurred, it could be readily compensated for by periodic recalibration, however this does not seem necessary since our experiments were done in a typical laboratory setting without need for recalibration. The fully collinear geometry does have the benefit that all of the pulses will be phase stable rather than just E_1 and E_2 although for many applications this is unnecessary. Pulse shaping also provides the additional benefit that phase cycling can be easily incorporated into signals, increasing the signal to noise ratio of the desired signal and, although we have not utilized this feature here, use of a pulse shaper allows the signal to be shifted into the rotating frame for faster data collection. [29]

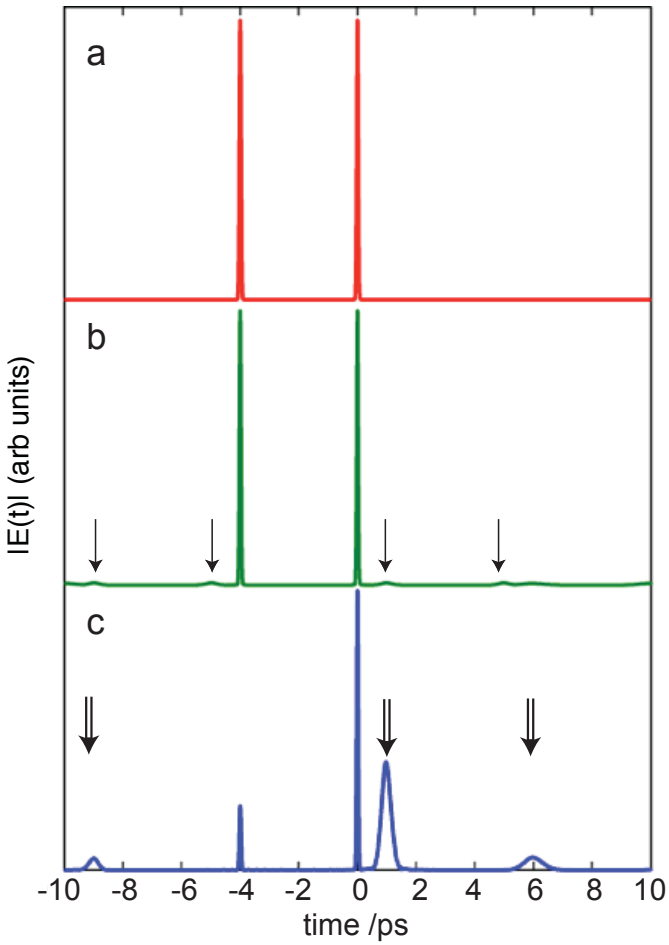

Figure 2.7 (a) Simulated pulse pair ($\tau = 4$ ps) produced with an ideal pulse shaper. (b) Pulse pair produced with simulated gaps, but otherwise continuous shaping ability. Arrows point to small pulses caused by gaps. (c) Spurious pulses produced as a result of simulated mask pixelation. The double arrow points to a spurious peak that interferes with the signal for τ >2 ps.

It is well known that SLMs cause non-negligible artifact pulses to be formed as the phase and amplitude masks become highly modulated. [27, 28] These artifact pulses arise primarily from two intrinsic properties of SLMs, resulting in non-ideal shaping of the electric field. The first of these is that SLMs have small gaps separating each of the independently adjustable liquid crystal pixels, which are not directly controlled by electrodes. Shown in Figure 2.7a is a simulation of a pulse pair (τ = 4.0 ps) created by an

ideal pulse shaper without pixels or gaps. The pulses in the pair are nicely shaped and tail to zero smoothly. Shown in Figure 2.7b is a simulation of the same pulse pair generated by a shaper without pixels, but with gaps of 2 units spaced every 100 units, which corresponds to the spacing of our SLM (2 μm gaps separating pixels of length 100 μm). The unshaped gaps produce additional pulses, but these artifact pulses have negligible effect on the recovered signal as they contribute less than 0.01% to the integrated intensity. The second property of SLMs that results in non-ideal shaping behavior is pixelation. Pixelation effects in pulse shapers arise because each individual pixel is of finite width and can only impart a constant change in the refractive index for all frequencies passing through it. The effects of pixelation are far greater than those associated with the gaps separating the pixels because spurious pulses are produced that have sufficient intensity that they can influence the experiment. Shown in Figure 2.7c is a simulation of the same pulse pair using our SLM pixel resolution of 0.428 nm (and no gaps) which corresponds to 1.25 Thz at 800 nm. The SLM pixelation causes spurious peaks at ~5 ps intervals (marked with a double arrows in Fig. 5c) relative to the second excitation pulse. The temporal position of the spurious pulses roughly corresponds to $2\pi/\Delta\omega_c$ where $\Delta\omega_c$ is the pixel resolution at the center of the spectrum[1]. The positions and intensities of these pulses track with τ, becoming closer to t = 0 and more intense as τ advances. With the spectral resolution of the SLM used in this work, the highest intensity spurious pulse marked with the double arrow has greater energy than the desired excitation pulse at 4 ps.

[1] Note that the spectrum is dispersed linearly in wavelength by the gratings in standard pulse shapers, so $\Delta\omega$ is ill defined across the entire spectrum leading to the observed broadening of the spurious pulses.

The spurious peaks produced by non-ideal shaping intrinsic to an SLM have two consequences for the collection of 2DE spectra. First, since intensity of the E_1 pulse is transferred to the spurious pulses, the magnitude of the desired signal is also proportionally reduced (see Equation 2.4). Second, the spurious pulses set the maximum delay that can be used in the experiments. For this reason, the time-domain data was multiplied with a cosine apodization function along τ that drops to zero by 2 ps, thus limiting the contribution from the spurious peaks.

2.7 Simulation of Pixelation Effects

To investigate the effects of SLM pixelation on the recovered 2D spectrum, a series of simulations were performed using a density matrix formalism with explicit inclusion of the light matter interaction. It is standard practice to employ a density matrix formalism in the description of nonlinear spectroscopies, however typically the density matrix is perturbatively expanded in orders of the light matter interaction (3^{rd} in the case of standard 2DE spectroscopy) to arrive at integrable expressions describing specific Liouville pathways. [23] For these simulations, however, the density matrix was propagated numerically and the light matter interaction was treated exactly (within the dipole approximation) thereby allowing the simulation of arbitrarily shaped electric fields. In this way, it was possible to model the effects of the spurious pulses produced by non-ideal shaping that would contribute to the detected signal in a laboratory setting.

2.7.1 Non-Perturbative Treatment

The induced polarization, $\boldsymbol{P}(t)$, of the density matrix is given by the expectation value of the dipole operator, Equation 2.13,

$$\boldsymbol{P}(t) = \mathrm{Tr}[\hat{\mu}\hat{\rho}(t)] \qquad [2.13]$$

where the density matrix, $\hat{\rho}(t)$, at time, t, is obtained by solving the equation of motion. The third order expansion of the density matrix thus yields the third order polarization, $\boldsymbol{P}^{(3)}(t)$, which can be readily used to calculate the 2DE spectrum (See Equation 2.4). However, when the density matrix is treated non-perturbatively, it yields the *overall* polarization reflecting all orders of the light matter interaction. It is thus necessary to be able to separate those polarization terms that are desired (in this case certain third order terms) from those that do not contribute to the 2DE spectrum.

In general, the induced polarization can be written as a sum of components,

$$\boldsymbol{P}(t) = \sum_{l,m,n} \tilde{P}_{l,m,n}(t) e^{i(lk_1+mk_2+nk_3)r} + c.c. \qquad [2.14]$$

where the k_n are the wave vectors of each portion of the electric field that interacts with the system, $\boldsymbol{E}(t) = \tilde{E}_1(t)e^{ik_1r} + \tilde{E}_2(t)e^{ik_2r} + \tilde{E}_3(t)e^{ik_3r} + c.c.$ Experimentally, each of the contributions to the overall polarization of the sample can be readily distinguished by the direction in which the signal is emitted, $k = lk_1 + mk_2 + nk_3$. The photon echo (non-rephasing pathways), for example, is emitted in the direction corresponding to l = -1, m = +1, n = +1. In a non-perturbative calculation, there can be no directional separation. However, the individual contributions can be separated in a similar way by first defining a phase $\phi_n = k_n r$. The polarization can then be written as,

$$\tilde{P}(t;\phi_1,\phi_2,\phi_3) = \sum_{l,m,n} \tilde{P}_{l,m,n}(t) e^{i(l\phi_1+m\phi_2+n\phi_3)} \quad [2.15]$$

where the parametric dependence of the polarization on individual phases of the electric field components is made explicit. It has been pointed out that the "directional" separation of the emitted polarization can then be realized by solving a set of linear equations [30, 31], or equivalently, by inverse Fourier transform with respect to the phase parameters, ϕ_n [32, 33]:

$$\tilde{P}_{l,m,n}(t) \propto \int_0^{2\pi} d\phi_1 \int_0^{2\pi} d\phi_2 \int_0^{2\pi} d\phi_3 \tilde{P}(t;\phi_1,\phi_2,\phi_3) e^{-i(l\phi_1+m\phi_2+n\phi_3)}. \quad [2.16]$$

Thus, to determine a specific directionally resolved component, the total polarization $\tilde{P}(t;\phi_1,\phi_2,\phi_3)$ is calculated for a set containing at least as many different ϕ_n as phase matched directions need to be uniquely determined. The desired signal can then be isolated by performing the discrete inverse Fourier transform (Equation 2.16) corresponding to the $k = l + m + n$ direction.

2.7.2 Simulation of Pixelation Effects

As mentioned previously, pixelation effects in pulse shapers arise because each pixel is of finite width and only imparts a constant spectral phase for all frequencies passing through it. Numerically, this can be modeled by an electric field of the form shown in Equation 2.17. This form of the field is simply an expansion of the amplitude and phase functions defined in Equations 2.10 and 2.11 which allows more convenient manipulation of the relative phases, ϕ_n, as well as the addition of a third excitation pulse (probe pulse). Nevertheless, it was numerically verified that upon Fourier transform, Equation 2.16

produces a time domain field (complete with spurious pulses) that is identical to that produced by Equations 2.10 and 2.11.

$$\tilde{\epsilon}_{out}(\omega) = \frac{1}{2}\sum_{n}\int_{-\infty}^{\infty} d\omega_n |\tilde{\epsilon}_{in}(\omega)| \Pi\left(\omega - \omega_n / \Delta_n\right)\left(e^{i\left(\frac{-\omega_n\tau}{2}+\phi_1\right)} + e^{i\left(\frac{\omega_n\tau}{2}+\phi_2\right)}\right) e^{-i\left(\frac{\omega_n\tau}{2}+\omega T\right)} + |\tilde{\epsilon}_3(\omega)| e^{i\phi_3} \quad [2.17]$$

Here, $|\tilde{\epsilon}_{in}(\omega)|$ is the spectral amplitude of the unshaped pulse before it is modulated by the SLM and $|\tilde{\epsilon}_3(\omega)|$ is the spectral amplitude of the third excitation pulse centered at t = 0. The ω_n are the set of central frequencies of the portion of the field passing through pixel n, and $\Pi\left(\omega - \omega_n / \Delta_n\right)$ is a rectangle function centered at ω_n with a width Δ_n that corresponds to the desired resolution in wavelength space. Note that SLMs rely on a grating or prism based zero dispersion pulse compressor to disperse the field into its spectral components and so the pixels are distributed linearly with wavelength and not with frequency.

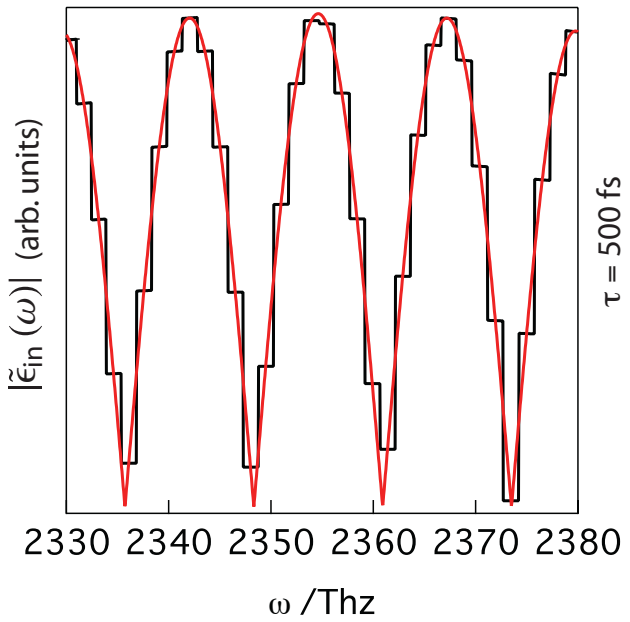

Figure 2.8 Spectral amplitude, $|\tilde{\epsilon}_{out}(\omega; \omega_n, \tau = 500\text{ fs})|$, for ideal pulse shaping (red) and .5 nm pixel resolution (black).

The spectrum of the electric field used in the simulation is a Gaussian defined around a central color (in this case around 2354.56 Thz or ~800 nm) in frequency space. To determine the ω_n, the pixel resolution of the SLM is specified in nm and a numerical algorithm determines the number of sampling points in frequency space (Δ_n) that correspond to the given wavelength resolution at each portion of the spectrum. These points are then binned in a "pixel." Then, the central wavelength of each bin defines ω_n, which is then used for all components of the field passing through pixel n, regardless of its optical frequency. As an illustration, consider Figure 2.8 which shows a portion of the spectral amplitude $|\tilde{\epsilon}_{out}(\omega, \omega_n; \tau = 500 \text{ fs})|$ for ideal pulse shaping with no pixels (red) and for a pixel resolution of .5 nm (black). Note that the resolution of the pulse shaper used in the above data was .428 nm (vide supra). For both cases, $|\tilde{\epsilon}_3(\omega)|$ (see Equation 2.17) has been set to 0 to simplify the spectral amplitude of the total field.

2.7.3 Model System

To determine the effects of the non-ideal shaping behavior, 2DE spectra of the two level Bloch model were simulated subject to pixelated pulse shaping. [34] This system was chosen as it is a system that has been well characterized in the literature and the lineshapes of the 2DE spectra have been extensively studied. [5, 6, 33] The Hamiltonian of the system is given by Equation 2.18 which is composed of the field free Hamiltonian, $\hat{H}_0$, and the field interaction operator $\hat{V}$. Here, $\boldsymbol{E}(t)$ is the real time dependent electric field and μ is the transition dipole moment (set to 1 in this work). E_{00} and E_{11} are the ground and excited state energies of the system.

$$\hat{H}(t) = \hat{H}_0 + \hat{V}(t) = \begin{bmatrix} E_{00} & 0 \\ 0 & E_{11} \end{bmatrix} + \begin{bmatrix} 0 & -\mu \cdot \boldsymbol{E}(t) \\ -\mu \cdot \boldsymbol{E}(t) & 0 \end{bmatrix} \quad [2.18]$$

We evolve the density matrix of the system in time under the Liouville-Von Neumann equation,

$$\frac{\partial}{\partial t}\hat{\rho}(t) = -\frac{i}{\hbar}\left[\hat{H}(t), \hat{\rho}(t)\right] \quad [2.19]$$

subject to the rotating frame and the slowly varying envelope approximations. [23, 34, 35] The densities $\rho_{11}$and ρ_{00} represent the excited and ground state populations, respectively. The density ρ_{10} is a measure of the coherent superposition of the ground and excited states. Equations 2.29-2.23 give the equations of motion for the density operator.

$$\dot{\rho}_{00} = -\frac{i}{\hbar}[\mu\tilde{E}^*(t)\rho_{01} - \rho_{10}\mu\tilde{E}(t)] - \Gamma_{01}\rho_{11} \quad [2.20]$$

$$\dot{\rho}_{10} = \frac{i}{\hbar}[\mu\tilde{E}^*(t)(\rho_{11} - \rho_{00}) - (E_{11} - E_{00})\rho_{10}] - \gamma_{10}\rho_{10} \quad [2.21]$$

$$\dot{\rho}_{11} = -\dot{\rho}_{00} \quad [2.22]$$

$$\rho_{01} = \rho_{10}^* \quad [2.23]$$

Here $\tilde{E}(t)$ is the complex amplitude of the electric field (24.3 fs FWHM by amplitude), given by the inverse Fourier transform of Equation 2.17. The population relaxation term, Γ_{01}, determines the rate of population relaxation from the excited state to the ground state and is set to 0 in these simulations. The dephasing parameter for the off diagonal terms, $\gamma_{10} = \frac{1}{2}\Gamma_{01} + \gamma_{10}^{pure}$ with γ_{10}^{pure} characterizing dephasing mechanisms not associated with population relaxation (such as elastic collisions). [34, 35] For all calculations presented below, γ_{10} = .01 fs^{-1} as this is a reasonable value for the electronic dephasing in condensed phase samples.

For calculation of the 2D spectra, 16 different realizations of the electric field ($\phi_{1,2} = 0, \frac{\pi}{2}, \pi, \frac{3\pi}{2}$ –see Section 2.7.1) were used in the propagation of the density matrix resulting in 16 total polarizations $\tilde{P}(t; \phi_1, \phi_2, \phi_3)$. The rephasing (l = -1, m = +1, n = +1 –see Equation 2.16 and discussion) and non-rephasing (l = +1, m = -1, n = +1) components were then isolated by performing the discrete inverse Fourier transform (Equation 2.16) on the set of overall polarizations, $\tilde{P}(t; \phi_1, \phi_2, \phi_3)$. In the partially collinear geometry, the fields corresponding to rephasing and nonrephasing pathways are emitted along the same wave vector and as such, are simultaneously detected (see Equation 2.2). 2D spectra are obtained by Fourier transform of the sum of rephasing and nonrephasing pathways along t_3 and a cosine transfer along (positive only) τ. [36] Figure 2.9 shows the real and imaginary parts of the 2D spectrum for T = 0 fs (top) and T = 100 fs (bottom). The T = 0 fs 2D spectrum exhibits "phase twist" due to the temporal overlap of E_3 with E_1 or E_2 [5], but the spectra remain identical to that shown for T = 100 fs for all values of T greater than the pulse width. These spectra are generated assuming ideal shaping with no pixelation effects. In the next section, we will examine the spectral distortions that arise from non-ideal pulse shaping.

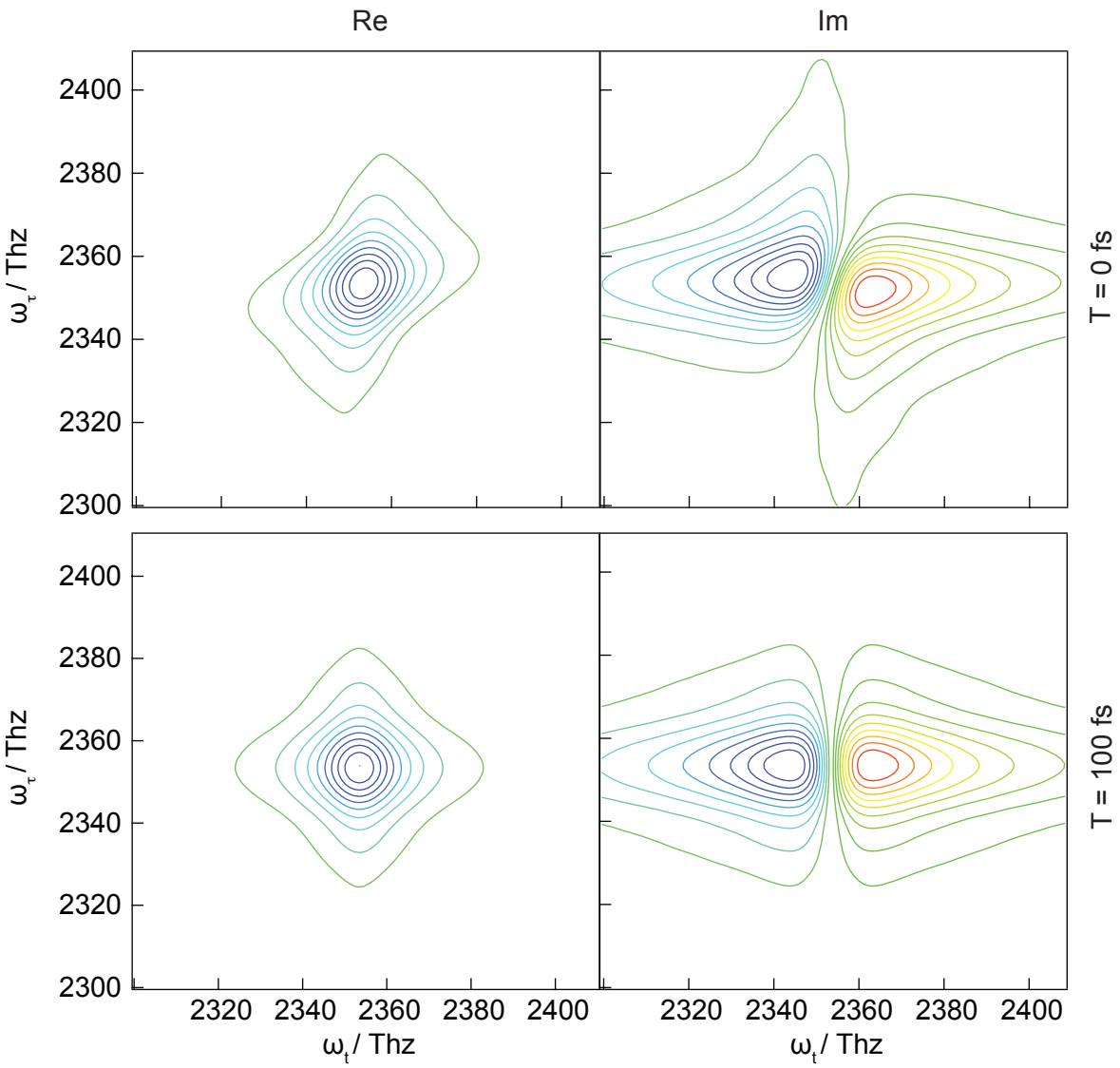

Figure 2.9 (top) Real and imaginary spectra for T = 0 fs for the Bloch model with γ_{10} = .01 fs^{-1}. The spectra show a phase twist due to pulse overlap effects. (bottom) Real and Imaginary spectra for T = 100 fs. Warm colors indicate negative amplitude and cold colors indicate positive amplitude. The contours demarcate 10% intervals of the total amplitude.

2.8 Spectral Distortion

As discussed above, pixelation of the SLM leads to the generation of spurious pulses as well as some amplitude modulation of the E_1 excitation pulse. Figure 2.10 shows a series of spectra generated with pixel resolution, $\Delta\lambda$, of 0.5, 1.0, and 1.5 nm (again, experimental pixel resolution of the SLM for the Rb spectrum collected above was .428 nm) as well as the

corresponding difference spectra comparing the pixelated and non-pixelated results[1]. The wavelength resolutions of 0.5, 1.0, and 1.5 nm correspond to frequency differences (at the center of the spectrum, 800 nm) between pixels of 1.47, 2.94, and 4.41 Thz. As in Figure 2.9 these spectra are collected for the Bloch model with an electronic dephasing rate γ_{10} = .01 fs^{-1}. The pulse pair separation, τ, is scanned from 0 fs to 400 fs and T = 100 fs. In the three spectra collected with pixelation effects, the maximum deviation, defined as the maximum difference between the ideal spectrum and the spectrum generated using the pixelated function Equation 2.16, is 5.6%, 11.8%, and 18.6 % deviation from ideal for $\Delta\lambda$ = 0.5, 1.0, and 1.5 nm, respectively. The cause of this spectral distortion lies in polarizations created by Liouville pathways that are insidiously dependent on the spurious pulses created by the pixelation of the pulse pair function.

[1] Only shown is the real (absorptive) part of the spectrum as it is the only portion experimentally detected in this geometry. [5]

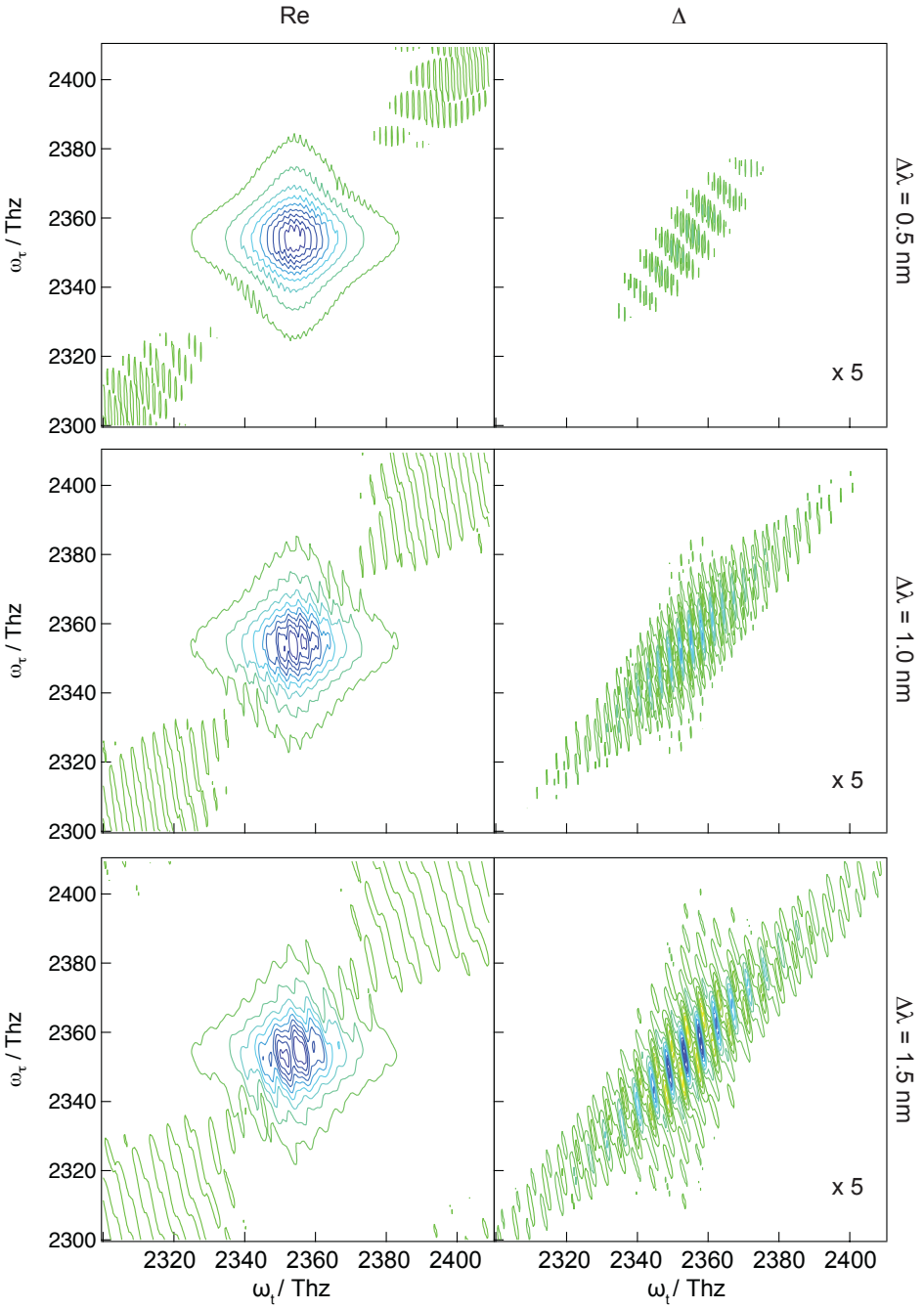

Figure 2.10 (***left***) Real (absorptive) spectra for T = 100 fs for the two level Bloch model with pixel resolution $\Delta\lambda$ = .5 nm (top), 1.0 nm (middle), and 1.5 nm (bottom). Contour lines are at 10% intervals of the maximum. (***right***) Corresponding spectra showing difference (×5) between ideal and pixelated pulse shaping. Contour lines are at 2% intervals of the real, ideal spectrum.

To illustrate the origin of these effects, consider the electric field generated by Fourier transform of Equation 2.17 with τ = 350 fs, $\Delta\lambda$ = 1.0 nm, and T = 100 fs shown in

Figure 2.11. The majority of the electric field amplitude is taken up by the desired three pulse sequence composed of the pulse pair E_1,E_2 separated by τ, and the third excitation pulse E_3, centered at t =0. However, there are spurious pulses (referred to as E_s, generally) that have non-negligible amplitude at ~ 1.7 ps and ~ 3.8 ps. These pulses arise from pixelation effects and are roughly located in time at integer multiples of $2\pi/\Delta\omega_c$.

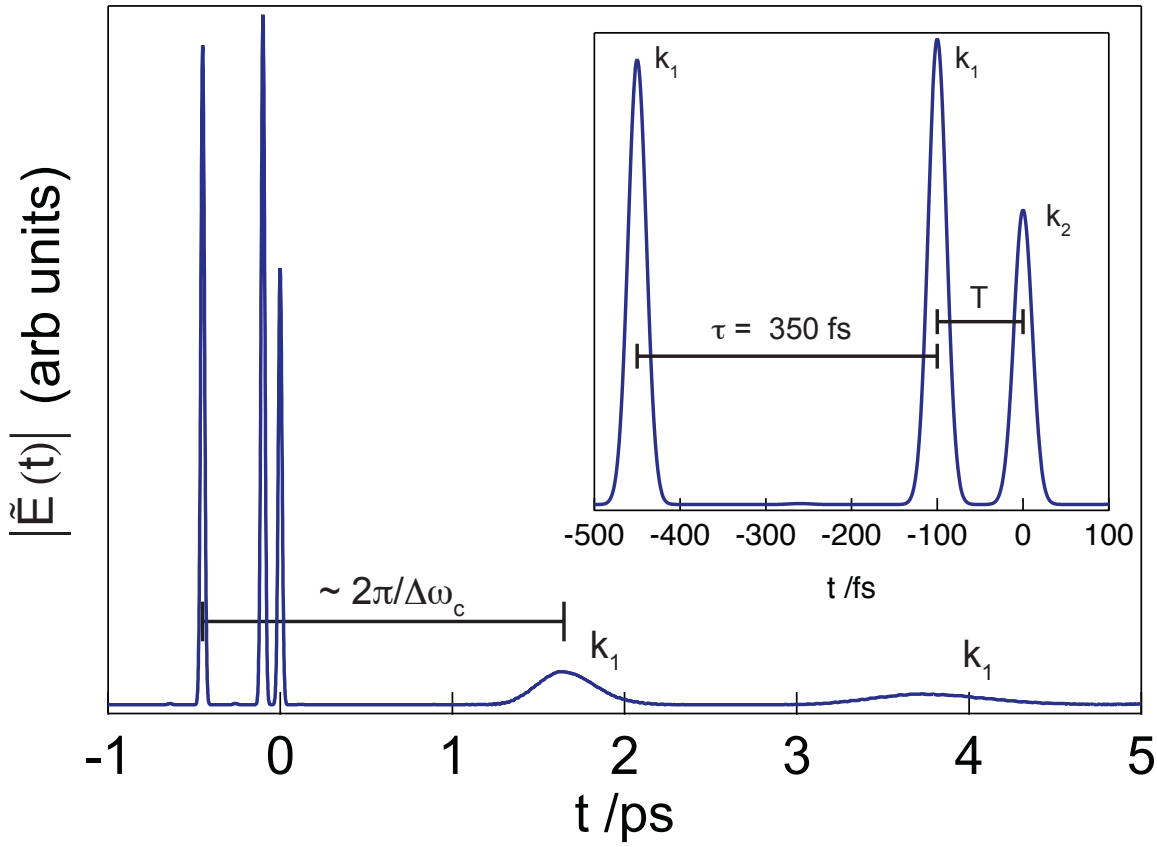

Figure 2.11 Electric field amplitude generated by inverse Fourier transform of Equation 2.16. Parameters are τ = 350 fs and $\Delta\lambda$ = 1.0 nm, and T = 100 fs. Experimentally, pulse E_3 has wavevector k_2, while pulses E_1 and E_2 have wave vectors k_1. The broad spurious pulses also have k_1 wave vectors and are located at at t ~ 1.7 ps and ~3.8 ps, corresponding to ~ $2\pi/\Delta\omega_c$, $4\pi/\Delta\omega_n$, etc. *Inset:* detail of pulses E_1, E_2, and E_3.

Note that in the partially non-collinear geometry used in this work, E_1 and E_2 both have wave vectors given by k_1 and E_3 has a different wavevector given by k_2. Because the

spurious pulses are produced collinearly with the desired pulse pair E_1,E_2, they also have a wave vector given by k_1.

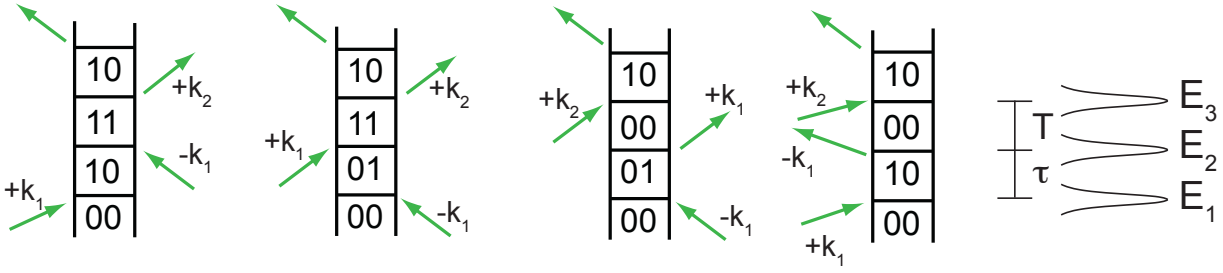

Figure 2.12 Double sided Feynman diagrams showing the four Liouville pathways contributing to the desired polarization $P_{2D}^{(3)}(t,T,\tau)$. Nonrephasing pathways are the represented by the outermost diagrams, rephasing pathways by the middle two diagrams.

The three pulse sequence, E_1, E_2, E_3 is the source of the desired polarization, $P_{2D}^{(3)}(t,T,\tau)$ (see Equation 2.4), which, under the rotating frame approximation and assuming T is greater than the pulse width, arises from the four Liouville pathways represented as double sided Feynman diagrams in Figure 2.12. [23] Under a relatively broad range of conditions, however, additional contributions to the third order polarization are allowed due to the generation of spurious pulses. These pathways have the pulse interaction order of E_2, E_3, E_s and create a polarization with exactly the same phase matching conditions as the desired signal. It is these pathways, which are shown in Figure 2.13, that serve to distort the 2D spectra seen in Figure 2.10.

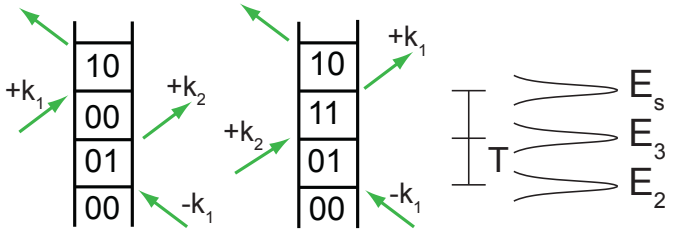

Figure 2.13 Double sided Feynman diagrams showing the Liouville pathways contributing to the spurious polarization.

Note the difference in time ordering of the interactions. The first interaction with the field occurs with E_2 which is centered at t = -T. The second interaction is then with E_3, creating a population that relaxes slowly during the interval between E_3 and a spurious E_s pulse. It is noted that additional diagrams will contribute once the spurious pulses overlap with E_2 and E_3, but those are likely of minor importance in practice, except for samples with very long coherence lifetimes (> 1 ps).

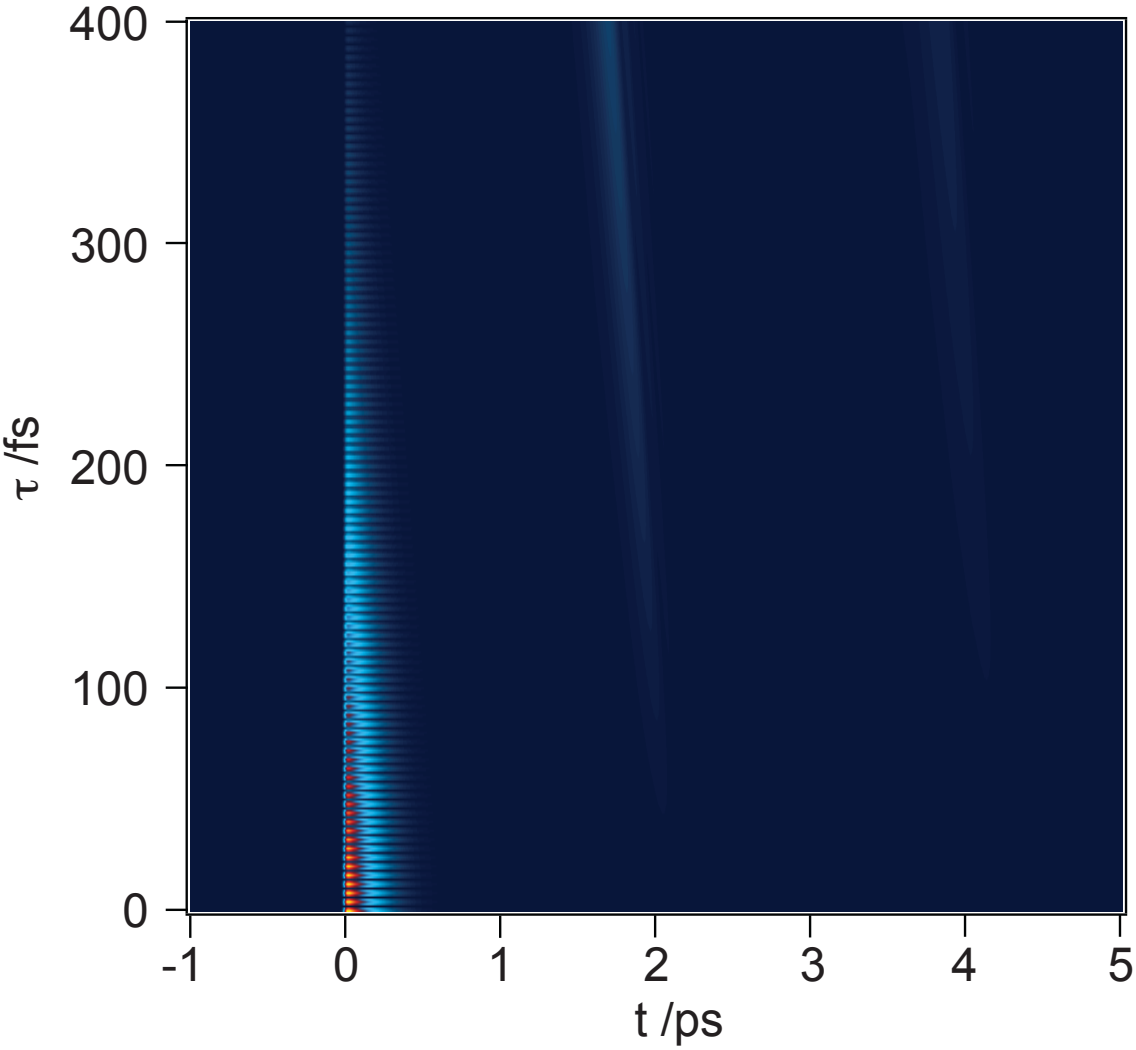

Figure 2.14 Third order polarization that would be experimentally phase matched in the k_2 direction. The primary feature is the desired signal, $P_{2D}^{(3)}(t,T,\tau)$, with an onset at t = 0 ps. The spurious polarization signals that cause spectral distortion have an onset at ~ 2.25 ps and ~ 4.5 ps. They move in time and gain intensity as τ is scanned from 0 fs to 400 fs.

The total 3rd order time dependent polarization in the phase matched direction, k_2, which is a sum of the desired polarization, $P_{2D}^{(3)}(t,T,\tau)$ and the spurious polarization discussed above, is shown in Figure 2.14. As in Figure 2.10 (middle) $\Delta\lambda$ = 1.0 nm, T = 100 fs, and γ_{10} = .01 fs^{-1}. If Figure 2.14 is compared with the electric field shown in Figure 2.11, it can be seen that the distorting polarization is coincident with the spurious pulses and increases in intensity and moves backward in time as τ is scanned from 0 fs to 400 fs. Another property to note is that the spurious polarization is sensitively dependent on the population time, T. Since the Bloch model has exponential damping during coherence intervals, we expect the magnitude of the spurious polarization to exponentially damp with T. As is shown in Figure 2.15, the maximum distortion of the recovered spectrum follows this trend as well.

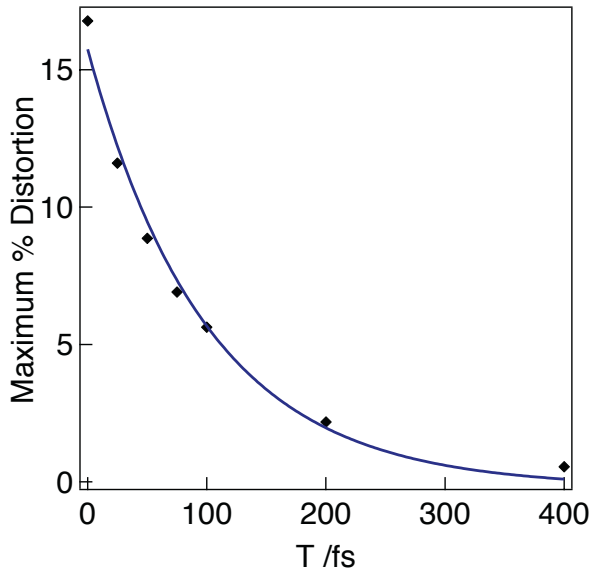

Figure 2.15 Maximum distortion (defined as the maximum of the difference spectra between ideal and pixelated spectra) as a function of population time, T (black diamonds). τ_{max} = 400 fs, $\Delta\lambda$ = .5 nm in all cases. The blue line is an exponential fit with a constrained time constant of 100 fs.

Fortunately, distortions to the 2D spectrum from interactions of this type are relatively easy to mitigate. The most straightforward option is to increase the pixel resolution of the pulse shaper so that contributions to the overall 2D spectrum are negligible. As a general rule, it is necessary for $2\pi/\Delta\omega_c$ to be at least 30 times greater than τ_{max}, the maximum separation between the pulse pair, to keep distortions under 5% of the ideal spectrum, although this is sensitively dependent on the value of T as is discussed above. The pulse shaper used in the experimental portion of this work (at 800 nm) has $\Delta\omega_c = 1.25$ Thz, which should permit τ_{max}~170 fs –a value that is sufficient for many condensed phase samples. We note, however, that the situation may become more difficult at higher energy colors where pixel resolution will decrease due to the higher energy density per unit wavelength.

Even with relatively poor pixel resolution, however, a simple time-domain filter applied to the third-order polarization dramatically improves the recovered 2D spectrum. Experimentally, this filter can be implemented by performing an inverse Fourier transform on the recovered spectrum (Equation 2.2) to retrieve the time domain signal. Since the spurious contributions to the third-order polarization occur later in time t, (see Figure 2.14), application of a time-domain hyperbolic tangent filter, Equation 2.24, easily eliminates all but the desired polarization. [37]

$$F(t) = \frac{1}{2}\left\{\left(\tanh\left(\frac{-t + t^{+}}{a}\right) + 1\right)\left(\tanh\left(\frac{t + t^{-}}{a}\right) + 1\right)\right\} \qquad [2.24]$$

Here t^+ and t^- give the cut off times in positive and negative t, respectively, and a determines the how quickly the filter maps from 0 to 1 (in this case, a = 12 fs, so that the filter transitions from 0 to 1 in ~ 100 fs. Upon Fourier transform of this filtered signal, a

nearly undistorted 2DE spectrum is recovered as shown by the difference spectra presented in Figure 2.16 for the cases of $\Delta\lambda$ = 0.5, 1.0, and 1.5 nm. Here, even for a pixel resolution of $\Delta\lambda$ = 1.5 nm, the maximum deviation from the ideal spectrum after the filtering procedure has been applied is only 1.1%.

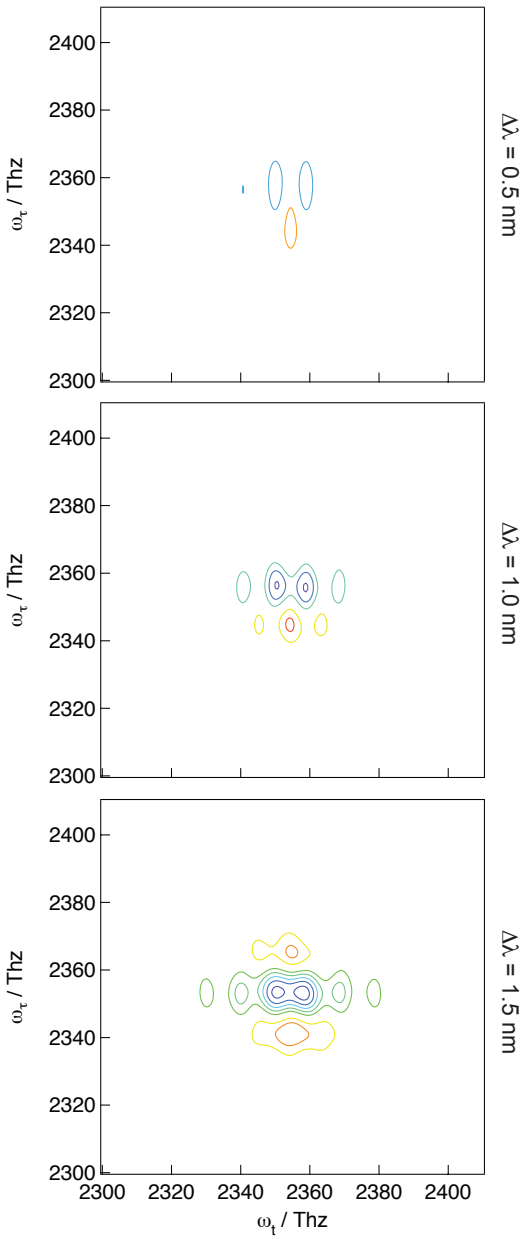

Figure 2.16 Difference spectra (real) for case of $\Delta\lambda$ = .5 nm (top), 1.0 nm (middle), and 1.5 nm (bottom). Contour lines correspond to .2% deviation from the ideal spectrum.

2.9 Conclusions

2DE spectra were collected using a partially non-collinear geometry coupled to a spatial light modulator for generation of phase-locked pulse pairs. The method was demonstrated on atomic Rb vapor, however because of non-ideal pulse shaping by the pixelated device, the interaction of long-lived electronic coherences and spurious pulses likely contributed to distortion of the lineshapes. Simulations using non-perturbative density matrix theory were performed on a simple model to determine how pixelation effects distorted 2D spectra and some guidelines for addressing these effects were proposed. Despite limitations of pulse shaping as a means to produce phase-locked pulse pairs, it remains a theoretically sound and highly practical method for generating 2D spectra. Bearing in mind limitations of an SLM and by applying a simple time-domain filter problems associated with pixelation effects can be easily minimized and there should be no reason high quality 2D spectra cannot be regularly collected with relative ease.

2.9 References Cited

1. J. D. Hybl, A. W. Albrecht, S. M. Gallagher Faeder, and D. M. Jonas, "Two-dimensional electronic spectroscopy," Chemical Physics Letters **297**, 307-313 (1998).

2. I. Stiopkin, T. Brixner, M. Yang, and G. R. Fleming, "Heterogeneous Exciton Dynamics Revealed by Two-Dimensional Optical Spectroscopy," The Journal of Physical Chemistry B **110**, 20032-20037 (2006).

3. G. S. Engel, T. R. Calhoun, E. L. Read, T.-K. Ahn, T. s. Mančal, Y.-C. Cheng, R. E. Blankenship, and G. R. Fleming, "Evidence for wavelike energy transfer through quantum coherence in photosynthetic systems," Nature **446**, 782-786 (2007).

4. D. Zigmantas, "Two-dimensional electronic spectroscopy of the B800-B820 light-harvesting complex," Proc. Natl. Acad. Sci. USA **103**, 12672-12677 (2006).

5. S. M. Gallagher Faeder and D. M. Jonas, "Two-Dimensional Electronic Correlation and Relaxation Spectra: Theory and Model Calculations," The Journal of Physical Chemistry A **103**, 10489-10505 (1999).

6. D. Jonas, "Two-dimensional femtosecond spectroscopy," Ann. Rev. Phys. Chem. **54**, 425-463 (2003).

7. G. Goodno, G. Dadusc, and R. Miller, "Ultrafast heterodyne-detected transient-grating spectroscopy using diffractive optics," Journal Of The Optical Society Of America B-Optical Physics **15**, 1791-1794 (1998).

8. T. Brixner, T. Mancal, I. Stiopkin, and G. Fleming, "Phase-stabilized two-dimensional electronic spectroscopy," Journal Of Chemical Physics **121**, 4221-4236 (2004).

9. V. Volkov, R. Schanz, and P. Hamm, "Active phase stabilization in Fourier-transform two-dimensional infrared spectroscopy," Opt. Lett **30**, 2010-2012 (2005).

10. T. Zhang, C. Borca, X. Li, and S. Cundiff, "Optical two-dimensional Fourier transform spectroscopy with active interferometric stabilization," Opt. Exp. **13**, 7432-7441 (2005).

11. M. Dugan, J. Tull, and W. Warren, "High-resolution acousto-optic shaping of unamplified and amplified femtosecond laser pulses," Journal Of The Optical Society Of America B-Optical Physics **14**, 2348-2358 (1997).

12. P. Tian, D. Keusters, Y. Suzaki, and W. Warren, "Femtosecond phase-coherent two-dimensional spectroscopy," Science **300**, 1553-1555 (2003).

13. P. Tekavec, G. Lott, and A. Marcus, "Flourescence-Detected Two-Dimensional Electronic Coherence Spectroscopy by Acousto-Optic Phase Modulation," Journal Of Chemical Physics **127**(2007).

14. J. Vaughan, T. Hornung, K. Stone, and K. Nelson, "Coherently controlled ultrafast four-wave mixing spectroscopy," The Journal of Physical Chemistry A **111**, 4873-4883 (2007).

15. M. F. Emde, W. P. de Boeij, M. S. Pshenichnikov, and D. A. Wiersma, "Spectral interferometry as an alternative to time-domain heterodyning.," Opt. Lett **22**, 1338-1340 (1997).

16. E. M. Grumstrup, S.-H. Shim, M. A. Montgomery, N. H. Damrauer, and M. T. Zanni, "Facile collection of two-dimensional electronic spectra using femtosecond pulse-shaping technology," Optics Express **15**, 16681-16689 (2007).

17. L. P. Deflores, R. A. Nicodemus, and A. Tokmakoff, "Two-dimensional Fourier transform spectroscopy in the pump-probe geometry.," Opt. Lett **32**, 2966-2968 (2007).

18. J. A. Myers, K. L. M. Lewis, P. F. Tekavec, and J. P. Ogilvie, "Two-color two-dimensional Fourier transform electronic spectroscopy with a pulse-shaper.," Optics Express **16**, 17420-17428 (2008).

19. P. E. Tekavec, J. A. Myers, K. L. M. Lewis, and J. P. Ogilvie, "Two-dimensional electronic spectroscopy with a continuum probe," Opt. Lett **34**, 1390-1392 (2009).

20. D. Abramavicius and S. Mukamel, "Disentangling multidimensional femtosecond spectra of excitons by pulse shaping with coherent control," Journal Of Chemical Physics **120**, 8373 (2004).

21. V. I. Prokhorenko, A. Halpin, and R. J. D. Miller, "Coherently-controlled two-dimensional photon echo electronic spectroscopy," Optics Express **17**, 9764 (2009).

22. M. D. Levenson and G. L. Eesley, "Polarization Selective Optical Heterodyne-Detection for Dramatically Improved Sensitivity in Laser Spectroscopy," Applied Physics **19**, 1-17 (1979).

23. S. Mukamel, *Principles of Nonlinear Optical Spectroscopy* (1995).

24. W. Wagner, C. Li, J. Semmlow, and W. Warren, "Rapid phase-cycled two-dimensional optical spectroscopy in fluorescence and transmission mode," Opt. Exp. **13**, 3697-3706 (2005).

25. S. Yan and H.-S. Tan, "Phase cycling schemes for two-dimensional optical spectroscopy with a pump-probe beam geometry," Chemical Physics **360**, 110-115 (2009).

26. S.-H. Shim, D. Strasfeld, Y. Ling, and M. Zanni, "Automated 2D IR spectroscopy using a mid-IR pulse shaper and application of this technology to the human islet amyloid polypeptide," Proc. Natl. Acad. Sci. USA **104**, 14197-14202 (2007).

27. J. Vaughan, T. Feurer, K. Stone, and K. Nelson, "Analysis of replica pulses in femtosecond pulse shaping with pixelated devices," Optics Express **14**, 1314-1328 (2006).

28. A. Weiner, "Femtosecond pulse shaping using spatial light modulators," Review of Scientific Instruments (2000).

29. D. Keusters, H. Tan, and W. Warren, "Role of pulse phase and direction in two-dimensional optical spectroscopy," The Journal of Physical Chemistry A **103**, 10369-10380 (1999).

30. L. Seidner, G. Stock, and W. Domcke, "Nonperturbative approach to femtosecond spectroscopy: General theory and application to multidimensional nonadiabatic photoisomerization processes," The Journal of Chemical Physics (1995).

31. B. Wolfseder, L. Seidner, G. Stock, and W. Domcke, "Femtosecond pump-probe spectroscopy of electron-transfer systems: a nonperturbative approach," Chemical Physics (1997).

32. H. Wang and M. Thoss, "Nonperturbative simulation of pump–probe spectra for electron transfer reactions in the condensed phase," Chemical Physics Letters **389**, 43-50 (2004).

33. T. s. Mančal, A. V. Pisliakov, and G. R. Fleming, "Two-dimensional optical three-pulse photon echo spectroscopy. I. Nonperturbative approach to the calculation of spectra," The Journal of Chemical Physics **124**, 234504 (2006).

34. R. W. Boyd, *Nonlinear optics,* Third ed. (Elsevier/Academic Press, Amsterdam, 2008).

35. K. Blum, *Density matrix theory and applications,* Second ed., Physics of Atoms and Molecules (Plenum Press, New York, 1996).

36. A. Albrecht, J. Hybl, S. Faeder, and D. Jonas, "Experimental distinction between phase shifts and time delays: Implications for femtosecond spectroscopy and coherent control of chemical reactions," Journal Of Chemical Physics **111**, 10934-10956 (1999).

37. D. Jonas, (personal communication, August 10, 2011).

CHAPTER 3

STUDY OF MULTIPLE EXCITON GENERATION IN SEMICONDUCTOR QUANTUM DOTS WITH OPEN- AND CLOSED-LOOP COHERENT CONTROL

3.1 Introduction

Multiple exciton generation (MEG) has been an enthusiastically pursued research avenue since the proposal by Nozik that the quantum-confined nature of nanocrystalline semiconductor quantum dots might be exploited for use in highly efficient photovoltaic devices. [1] Nozik proposed that MEG, wherein a single hot exciton produces two (or more) lower energy excitons in an energy conserving process, becomes a competitive relaxation channel in quantum-confined systems because large spacings between atomic-like energy levels result in inefficient phonon mediated relaxation. Because higher energy photons would create multiple excitons via MEG (rather then thermally relax) the bandgap of a photovoltaic device could be tuned to lower energies than a traditional device, allowing for a greater utilization of the solar spectrum. Efficient harvesting of multiple excitons as charge carriers would result in an enhanced power conversion efficiency in photovoltaic cells, greatly advancing progress of third-generation photoconversion.

Experimentally, Victor Klimov's group first reported evidence of multiple exciton generation in PbSe nanocrystals [2], followed shortly by the Nozik group with PbS and

PbSe nanocrystals. [3] Since then, exciton production in excess of 100% efficiency has been reported in CdSe, PbTe, InAs, and Si nanocrystals. [4] In many of these studies, ultrafast transient absorption measurements were employed to quantify the effect by comparing the short time (T ≈ 10 ps) bleach signal with that at long times (100s of ps). The early time signal reflects the total exciton (including multiexciton) population before Auger processes destroy any multiexciton population that may be present. The long time signal is a probe of the cooled, long-lived single excitons present at the bandgap energy. [5] Assuming linear excitation conditions and no other competing dynamics are present, the ratio of these two signals determines the quantum efficiency of the MEG process.

Direct photoexcitation [6, 7], coherent multiple exciton generation [8], and a bulk like incoherent impact ionization process [9] have all been proposed to explain the increase in exciton quantum yield observed in these systems. These proposed mechanisms each have different perspectives on how the multiple exciton states are formed. The model of Klimov and coworkers argues that direct photoexcitation from the ground state to states with multiexcitonic character is weakly allowed. The coherent model of Shabaev and coworkers proposes that the initially formed state is a superposition of single and multiple exciton states and the quantum yield of multiple excitons is ultimately determined by a competition between relaxation rates and coupling constants. Finally, the model of Franceschetti et al. argues that impact ionization alone can successfully explain MEG yields. It has therefore been a focus of current research to determine which of the proposed mechanisms is most closely descriptive of the physical process of MEG. The proposed research in this lab sought to employ tools of transient absorption spectroscopy and coherent control via ultrafast pulse shaping to enhance and interrogate the MEG process.

As has been demonstrated in the literature, coherent control methods, through unbiased searches of complex pulse shapes, are able to interact with systems exhibiting a wide range of relaxation behaviors, revealing information about the relevant photophysics. [10-18] Since the mechanistic specifics of the MEG process were unknown, adaptive techniques were initially employed with the directive of increasing MEG yield as they offer an unbiased method to first manipulate, and then through exploration, interrogate the photophysics of the energy conversion mechanism.

After numerous unsuccessful experiments with adaptive optimization techniques, we employed another pulse shaping technique with analogies to interferometry that employs sinusoidal spectral phase modulation to determine that we were unable to coherently couple to the studied system. [19] Consequently, we refitted our lab with a homebuilt non-collinear optical parametric amplifier (NOPA) so that our ability to optically couple more widely spaced excited states or coherently interact with more quickly dephasing states was improved. Subsequent experiments using the sinusoidal modulation technique indicated that despite our use of 35 fs excitation pulses, we were unable to coherently interact with the system. The data collected suggest the electronic dephasing time between the ground and excited states of the quantum dot system studied was occurring in < 20 fs.

3.2 Experimental

Experiments were performed on ~8 nm diameter PbSe nanocrystals prepared by the Nozik group at the National Renewable Energy Laboratory. The bandgap of this system

is centered at 1710 nm, with higher energy transitions easily resolved in the UV-Vis-NIR spectrum shown in Figure 3.1.

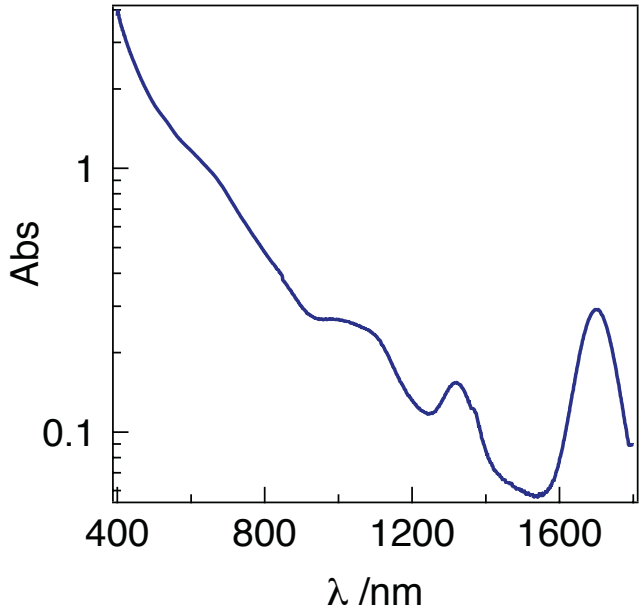

Figure 3.1 UV-Vis-NIR absorption spectrum of ~8 nm PbSe quantum dots suspended in tetrachloroethylene.

The nanocrystals, capped with oleate ligands, were suspended in either tetrachloroethylene or N-hexane, though the samples showed identical kinetics in both suspending liquids. All samples were handled under an inert nitrogen atmosphere in a glovebox and sealed in airtight cells during experimental runs. For initial experiments, pump/probe beams were generated with an amplified femtosecond 1 kHz pulse train centered at 800 nm used to pump a Light Conversion TOPAS optical parametric amplifier (see Figure 3.2). The signal and 800 nm beams were frequency summed to produce ~100 fs FWHM pulses centered at ~532 nm. The pump beam was then coupled into a 4-f, all reflective, zero dispersion pulse compressor with a CRI 640 pixel spatial light modulator (SLM) placed at the Fourier plane. This beam was mechanically chopped at 500 Hz and

coupled onto a mechanical delay stage before being focused onto the sample. To probe the photoinduced change in transmittance of the bandgap transition, the collinear idler beam (~1710 nm) from the OPA was separated with dichroic mirrors from the pump beam and split with a 50/50 beamsplitter before being focused onto the sample. The pump-probe signals, defined as the pump induced changes in probe transmittance (ΔT), were collected on InGAs amplified photodiodes and lock-in detected at the chopper frequency. For probing visible transitions, a probe beam was generated by focusing a small portion of the 800 beam into an amorphous sapphire window producing a white light continuum which was frequency resolved by a monochromator after passing through the sample and detected on an amplified silicon photodiode.

For the second series of experiments all excitation beams used were in the visible spectrum. The pump beam was generated by a homebuilt NOPA [20, 21] pumped by the same Ti:Sapphire laser system as above, compressed in a pair of fused silica prisms, and coupled into the pulse shaper before being focused onto the sample. Autocorrelation of the pump beam in a SiC photodiode showed durations of 35 fs FHWM at the sample position. [22] The probe beam was generated by focusing a small portion of the 800 nm beam into a sapphire window to produce a white light continuum.

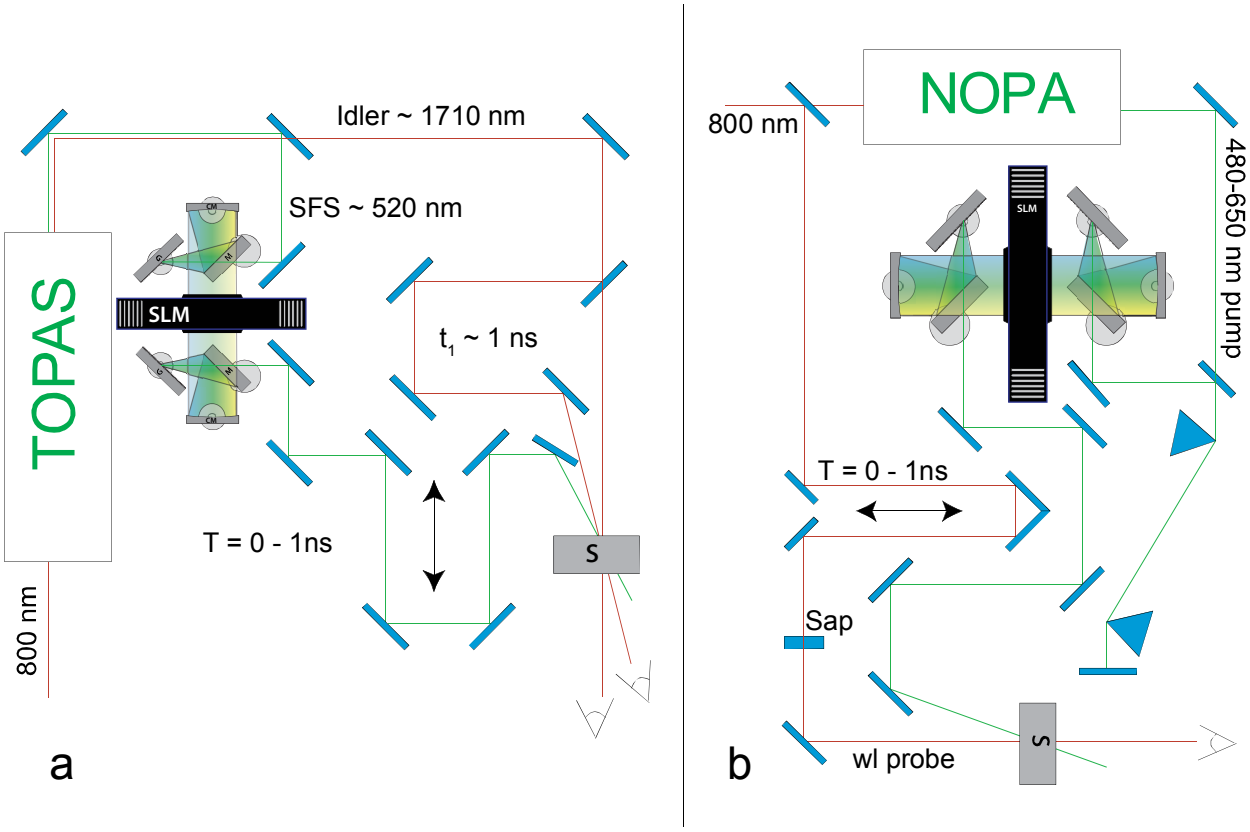

Figure 3.2 (*a)* Schematic of instrument used for adaptive control experiments and τ-scan experiments when λ_{probe} was tuned to the bandgap transition. T is the pump probe delay time varied by a computer-controlled stage. For some experiments, two probe beams were employed to monitor different components of the band edge signal by delaying one arm by t_1. When probing optical transitions, the probe beam was generated by focusing a small portion of the 800 nm beam into an amorphous sapphire window and then directed to the sample. (*b)* The apparatus employing a NOPA produced pump beam differed only in the addition of a fused silica prism compressor. In this figure, *sap* is the sapphire window used to produce the white light continuum probe beam (*wl probe*).

3.3 Adaptive Control

In recent years the development of coherent control has led to its becoming a incisive tool for probing myriad ultrafast photophysical processes in complex molecular systems. Often, adaptive algorithms are employed in these studies as a means to uncover the relevant degrees of freedom that affect excited state dynamics after excitation. [23-25] This technique is well established in our lab and it is particularly suited for examining the

mechanism of multiple exciton generation largely due to its ability to interact with complex systems and its flexibility in guiding experimentation in basic photophysics.

At the time we began these experiments, there were three proposed mechanisms by which MEG might occur. We hypothesized that coherent control methods would affect the direct method of Klimov et al. as well as the coherent model proposed by Shabaev et al. if either were operative, thereby lending insight into MEG mechanisms. [6-8] The coherent model of Shabaev et al. exhibited the most obvious case whereby coherent control schemes would affect quantum yields. The long lived coherence between single and multiple exciton states proposed in this model offered ample opportunity to manipulate interference phenomena affecting photoproduct quantum yields. This was examined in depth by simulating the effects of various pulse shaping techniques on the product distribution of the coherent biexciton model (vide infra). [8] In the model proposed by Klimov, the excitation probability to the multiexciton state is expressed as a product of two interactions: the first is the light-matter interaction which couples the ground state to virtual single exciton states and the second is the coulomb interaction that couples the single exciton states to the final multiexciton state. The sum over all possible products of interactions gives the probability of excitation, much like in perturbative expressions of two-photon absorption. [10, 11] It was hypothesized in this group that manipulating the phase of the exciting electric field would affect interference between contributing pathways to the final state. [26, 27] Finally, it was noted that the model of Franceschetti et al., since it is an intrinsically incoherent model, would yield a negative result to any attempt at control. [9]

In typical time resolved experiments, signatures of more than one exciton per nanocrystal are the Auger recombination kinetics observable for wavelengths probing bandgap transitions. This process is the primary relaxation pathway for multiple excitons in which one electron-hole pair will recombine, nonradiatively transferring the excess energy to another electron or hole. This hot electron or hole then relaxes via phonon coupling returning the system to a single band-gap exciton. [5, 28] Auger recombination occurs in PbSe on the 50 - 100 ps timescale, whereas the radiative rate for the single cooled exciton is in the 10-100 ns timescale. An example of bandgap bleach kinetics collected for the lead selenide system is shown in Figure 3.3. The initial multiple exciton signal decays within 200 ps, and the long-lived single exciton signal does not decay in the window of the measurement as is expected from its 10-100 ns radiative decay lifetime.

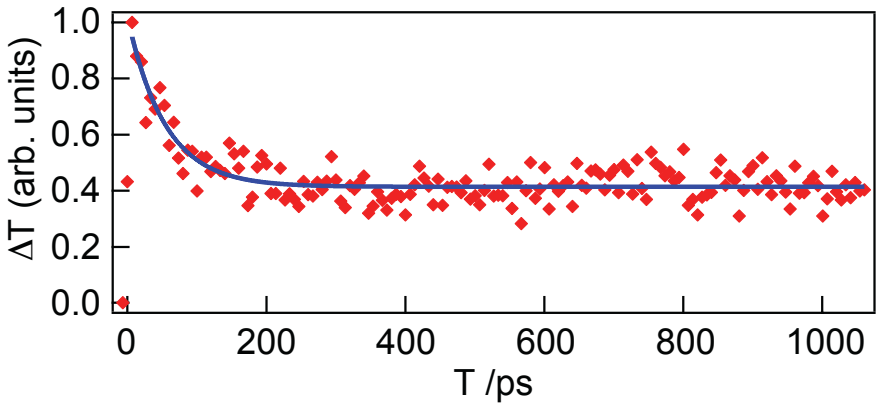

Figure 3.3 Transient bleach kinetics probing at the bandgap of 8 nm quantum dots. Fit is a single exponential with k – 55 ps.

Initial experiments sought to maximize the multiple exciton yield after shaped pulse excitation relative to the long-lived single exciton population. The probe beam was split and one arm delayed so that long time kinetics and early time, multiple exciton kinetics could be monitored simultaneously during an adaptive experiment (see Figure 3.2). An initial population of trial pulse shapes was generated by a random number generator,

which, for each pixel of the SLM, generated the applied phase for each trial pulse shape. Typically the spectrum of the laser pulse was spread across 100-120 pixels. Each of these trial pulse shapes was used to photoexcite the quantum dot sample and a value of the fitness was recorded. For this experiment, the fitness was defined as the ratio of the signal size at early times to the signal size at late times thereby accessing the quantum yield of the system as the fitness objective. The home written genetic algorithm employed analogues of mutation, cloning, and breeding as a means to select the population and advance it toward maximization of the fitness. [16, 17]

More than 20 attempts were made to optimize the quantum yield with no convincing evidence that pulse shaping improved the quantum yield over unshaped pulses. Optimizations were performed under a variety of excitation conditions including varying the pump beam center wavelength between 480 nm and 535 nm and probing at various energies including bandgap transitions in the near IR and visible transitions that probed higher lying states of the nanocrystalline system. Analysis of the data concluded there were two main difficulties with the experiment as designed, and so attempts were made to redesign the experiment to address these two issues. The first practical difficulty arose because of noise stemming from the use of the idler beam produced by the TOPAS. This probe beam proved to be highly unstable with shot to shot noise between 10 and 15 % leading to very difficult measurements of the band gap bleach. This degree of instability, coupled to the required low fluence levels of the pump beam needed to ensure linear excitation conditions, made genetic algorithms highly unstable and subject to erroneous population selections. The second problem associated with the genetic algorithm scheme was the overlap of pump and probe beams with complex pulse shapes. The algorithm

generates highly complex, randomized pulses in the first generation with typical pulse widths spanning 4-5 ps in length. This complex structure, although typically irrelevant to the photophysics of systems studied in our lab, resulted in uncharacteristic rise and decay kinetics. Since the target fitness always included the maximum value of the transient kinetics (as this was the quantity we wished to maximize), long pulse shapes frequently contributed to anomalous values for measured fitness and the genetic algorithm would incorrectly direct the population. These results obviate the limitations of genetic algorithms and show the importance of vigilance so as not to over-interpret artifact-influenced results.

In light of the negative results obtained from adaptive optimization experiments, we sought to determine whether controllability was feasible under the employed experimental conditions. Coherent control of photophysics requires coupling of the excitation field to electronic or vibrational coherences. If this requirement is not met, excitation of a chromophore could just as well be excited with any incoherent light source. It is the ability of shaped laser pulses derived from ultrafast sources to coherently manipulate the vibrational and/or electronic wave packets that can reveal information about the fundamental photophysics of the system. To address this salient point, we designed a pulse shaping experiment based on sinusoidal spectral phase modulation that was aimed at determining whether the quantum dot system was controllable under the experimental conditions we had available in our lab.

3.4 Sinusoidal Spectral Phase Modulation

The technique we developed is a Fourier transform open-loop pulse-shaping technique that employs sinusoidal spectral phase modulation to explore vibrational and electronic coherences by manipulating only the phase of the excitation field. [19] The technique is performed with a pulse shaper and in a typical pump-probe geometry, so there is no modification to the apparatus from a transient absorption measurement or a closed-loop control experiment that uses change in transmittance of a probe beam as a feedback signal. As discussed in much greater detail in chapter 5, the technique uses a sinusoidal phase mask in the spectral domain to produce a train of pulses (in the time domain) with well-defined temporal separations, relative phases, and amplitudes. Equation 3.1 shows the functional form of the phase mask applied during such a measurement.

$$P(\omega;\tau) = \alpha[\cos(\omega\tau + \phi) + 1] \qquad [3.1]$$

Briefly, α defines the amplitude of the phase modulation, which determines the number and relative amplitudes of the subpulses in the time-domain electric field. The temporal interpulse spacing is determined by τ and the relative temporal phase is modified by ϕ. Typically, ω is the frequency of the electric field component passing through the parameterized pixelated SLM, although in principle the choice of this frequency is arbitrary and could be exploited so as to perform measurements in the rotating frame. [29]

Since this technique manipulates only the phase of the electric field, every possible pulse shape produced has the same fluence as a transform-limited pulse. To generate a signal trace with this technique, the excitation pulse is spatially modulated by the pulse shaper for a set of parameters α , τ, and ϕ before passing through the sample. The probe beam is set to probe the photoexcited system at a delay time after the pump-shaping

window has passed and the system dynamics are not rapidly changing. A signal trace, called a τ-scan in this work, is comprised of the data points collected for a scan of the τ parameter. If the quantum yield of the probed species is affected by these phase manipulations, the recovered signal will oscillate at well-defined frequencies corresponding to the fundamental and higher harmonics of the transition frequency connecting ground and excited states.

The problems we encountered with our adaptive control experiments outlined above are readily solved with the τ-scan technique. Since only a few hundred pulse shapes are needed for a signal trace, much longer periods of signal averaging are possible compared to an adaptive control experiment that typically requires several thousand pulse shapes. A further benefit of the method is the Fourier transform of the signal trace greatly enhances the recovery of meaningful signal from noisy data. Thus, the problematic low signal-to-noise levels encountered with adaptive control experiments are mitigated when using a τ-scan technique. The second difficulty encountered with the adaptive control experiments – that of pump-probe temporal overlap are easily eliminated with the τ-scan technique since the pulse train produced is well defined and temporally localized to a few hundred femtoseconds (based on limits set with τ). Consequently, there is little risk of artifacts arising in the signal due to pump-probe overlap as long as the probe reaches the sample after the pump-shaping window has passed.

As an initial guide to the behavior we expected to observe in the lab, we reproduced the coherent biexciton model of Shabaev et al. [8] This model includes a non-perturbative treatment of the light matter interaction and as such, has an explicit inclusion of the time dependent electric field in the Hamiltonian. To simulate the effects of a shaped electric field

on the system, we coupled to the model the ability to arbitrarily shape the simulated laser pulse in the frequency domain. The shaped spectral field was then inverse Fourier transformed and used in the equations of motion (Equations 3.2 - 3.9) as the excitation field. Typical field strengths used in the simulations resulted in an excited state population range of 5-15%, corresponding to our experimental excitation densities. In general, parameters of the system such as relaxation time constants and coulombic coupling constants were systematically varied in the presented simulations to determine a possible range of behaviors expected. A fourth order Runge-Kutta algorithm was used to propagate the equations of motion subject to the slowly varying envelope and rotating wave approximations. [30, 31] Shown in Figure 3.4 is a schematic of the coherent biexciton model.

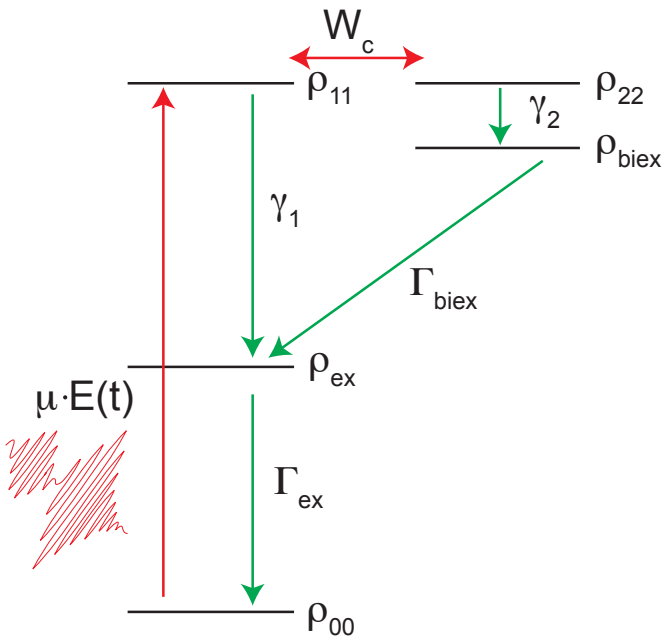

Figure 3.4 Illustration of the coherent biexciton model. The shaped electric field (E(t)) interacts with the system creating an excited single exciton (ρ_{11}) which is coupled to the excited biexciton state (ρ_{11}) with parameter W_c. The single and bi exciton states relax with rates of γ_1 and γ_2, to their respective relaxed states, ρ_{ex} and ρ_{biex}. Biexcitons decay to single excitons with Γ_{biex}. The relaxed single exciton decays to the state with no excitons with the rate Γ_{ex}.

The simulations showed the biexciton quantum yield was sensitive to phase shaped pulses under a wide range of parameters. Furthermore, our study of this model showed that a τ-scan recovered fundamental information about the multiple exciton generation process given the relevance of certain physical parameters. Specifically, the interference of the single and biexciton states allows the determination of the coupling constant between those two states. Shown in the left column of Figure 3.5 are example τ-scan signal traces recovered from the coherent MEG model. The dominant contribution to the signal is the component oscillating at $E_1/\hbar$, where E_1 is the energy difference between the ground and initially excited states. The quantum beats observed in the signal trace are evidence of the coherent nature of the exciton/biexciton superposition that is being influenced by the pulse shape. The power spectrum of the signal shown in the right column of Figure 3.5 reveals peak splitting equal to twice the coupling, W_c, between the two states.

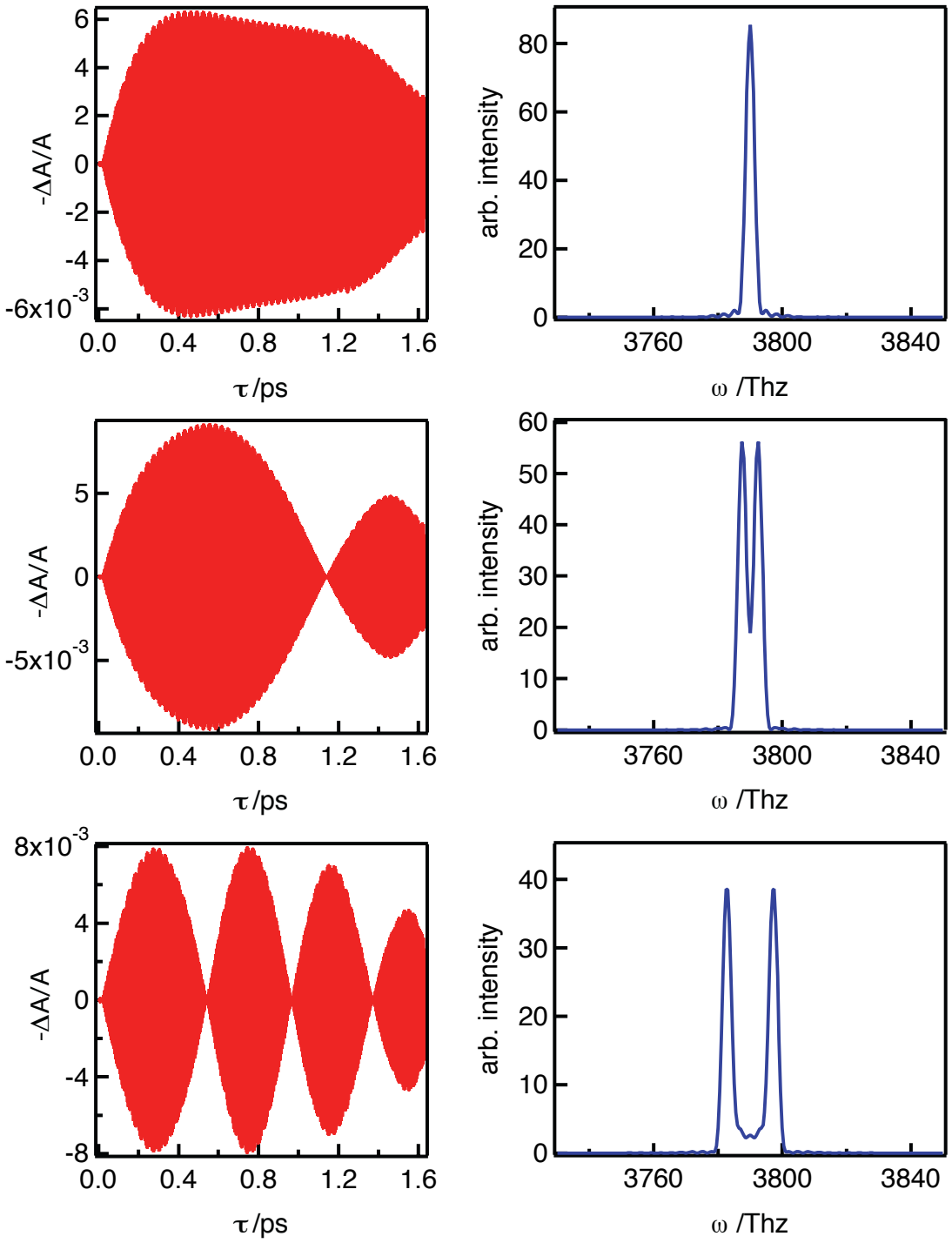

Figure 3.5 Left column: Simulated time domain signal traces for a τ-scan performed on the coherent MEG model with coupling, W_c, between exciton and biexciton states ranging from $.5\gamma_2$ (top), γ_2 (middle), and $2\gamma_2$ (bottom), with γ_2 being the biexciton relaxation rate. Right column: power spectra of corresponding signal traces. Splitting of peaks, $\Delta = 2\ W_c$.

The importance of this measurement is clear. If, through this pulse shaping technique, the coupling between the multi- and single exciton state could be recovered, it would make available a direct probe of the dependence of that parameter on the material of the quantum dot, as well as the size, capping ligands, and a multitude of other properties that affect quantum yield in an unknown manner. Furthermore, because the method is exclusively sensitive to phase dependent manipulations of quantum yield, it is blind to any incoherent multiple excitons produced by multiple, uncorrelated photon absorption events. Consequently, even at higher powers where these multiple absorption events occur, only the phase sensitive events are recovered with this technique. This is highly advantageous as it avoids the low signal to noise measurements or long averaging times that are necessary at the very low fluence levels.

One limitation of the model proposed by Shabaev and coworkers was that it did not include any pure electronic dephasing between states. [8] The timescale of this process is crucially important since coherent control of photochemical processes requires interaction with the target system's electronic and vibrational coherences before they have lost memory of previous interactions. So as to theoretically explore our ability to coherently control this system if it were to exhibit typical dephasing times of condensed phased systems, we modified the model with a simple, phenomenological electronic dephasing parameter, γ_e. Equations 3.2-3.9 show the coupled rate equations defining the system with the modified coherence damping terms, γ_e, added to off-diagonal coherences (ρ_{10} and ρ_{20}) connecting the ground state (ρ_{00}) to the excited single- (ρ_{11}) and bi- (ρ_{22}) excitonic states. This dephasing rate was also included in the off diagonal term (ρ_{12}) connecting the excited single and biexciton states. [32] The parameter Δ_{12} defines the detuning between the single

and biexciton states. As the system is propagated under the rotating wave approximation, the complex amplitude, $\tilde{\varepsilon}(t)$ is used in the equations of motion.

$$\dot{\rho}_{00} = -\frac{i}{\hbar}\left((\mu\cdot\tilde{\varepsilon}^{*})\rho_{10} - \rho_{01}(\mu\cdot\tilde{\varepsilon})\right) + \Gamma_{ex}\rho_{ex} \quad [3.2]$$

$$\dot{\rho}_{11} = i\frac{W_c}{\hbar}(\rho_{12} - \rho_{21}) + \frac{i}{\hbar}\left((\mu\cdot\tilde{\varepsilon}^{*})\rho_{10} - \rho_{01}(\mu\cdot\tilde{\varepsilon})\right) - \gamma_1\rho_{11} \quad [3.3]$$

$$\dot{\rho}_{22} = -i\frac{W_c}{\hbar}(\rho_{12} - \rho_{21}) - \gamma_2\rho_{22} \quad [3.4]$$

$$\dot{\rho}_{ex} = \gamma_1\rho_{11} + \Gamma_{biex}\rho_{biex} - \Gamma_{ex}\rho_{ex} \quad [3.5]$$

$$\dot{\rho}_{biex} = \gamma_2\rho_{22} - \Gamma_{biex}\rho_{biex} \quad [3.6]$$

$$\dot{\rho}_{10} = \frac{i}{\hbar}(\mu\cdot\tilde{\varepsilon})(\rho_{11} - \rho_{00}) + i\frac{\hbar\omega - E_1}{\hbar}\rho_{10} - i\frac{W_c}{\hbar}\rho_{20} - \frac{\gamma_1 + 2\gamma_e}{2}\rho_{10} \quad [3.7]$$

$$\dot{\rho}_{20} = i\frac{\hbar\omega - E_1 + \Delta_{12}}{\hbar}\rho_{20} + \frac{i}{\hbar}(\mu\cdot\tilde{\varepsilon})\rho_{21} - i\frac{W_c}{\hbar}\rho_{10} - \frac{\gamma_2 + 2\gamma_e}{2}\rho_{20} \quad [3.8]$$

$$\dot{\rho}_{12} = i\frac{W_c}{\hbar}(\rho_{11-}\rho_{22}) + i\frac{\Delta_{12}}{\hbar}\rho_{12} + \frac{i}{\hbar}(\mu\cdot\tilde{\varepsilon})\rho_{02} - \frac{\gamma_1 + \gamma_2 + 2\gamma_e}{2}\rho_{12} \quad [3.9]$$

Figure 3.6 shows simulated τ scan signal traces resultant from the sinusoidal phase modulation technique in the window τ = 0 - 150 fs for the coherent biexciton model given electronic dephasing rates, γ_e, of 0 fs^{-1}, .01 fs^{-1}, and .05 fs^{-1}. These dephasing time constants correspond to the limits of an atomic like system at γ_e =0 fs^{-1} and a timescale that would far exceed our detection abilities at γ_e =.05 fs^{-1}. Similarly to Figure 3.5, the oscillation in the signal trace is due to interference of wavepackets created by different subpulses in the pulse train generated by sinusoidal modulation. The diminishing magnitude and duration (note the difference in τ scales) of the interference in the trace reflect the reduced ability of the pulse to coherently couple with previously excited wavepackets due to electronic dephasing of the system. The traces reveal that the sinusoidal phase shaping technique is a

probe of the dephasing time of this photophysical system, and consequently allows for simple and *in situ* determination of the coherent controllability of the system (see Chapter 5). While no claim can be made that the manipulations to quantum yield explored by this pulse shaping technique are optimal, they do reflect whether the field has the necessary spectral and temporal characteristics to couple to the system coherently.

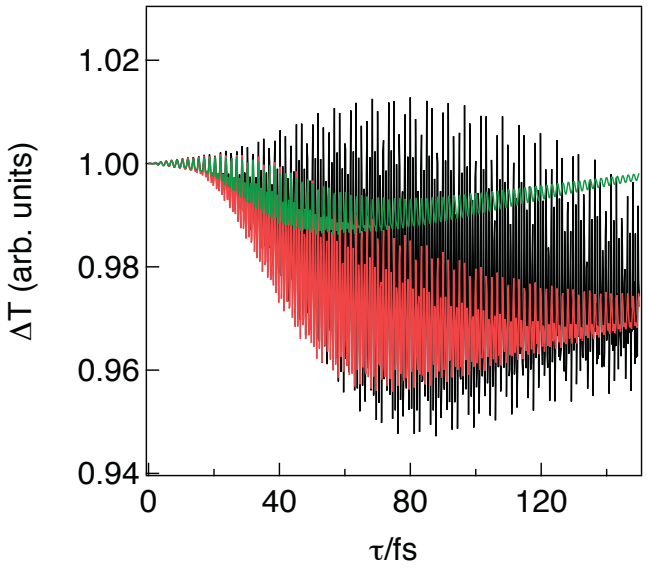

Figure 3.6 Simulated time domain PS signal trace signals with electronic dephasing rate constants, $\gamma_{e,}$ of 0 fs^{-1} (black), .01 fs^{-1} (red), .05 fs^{-1} (green).

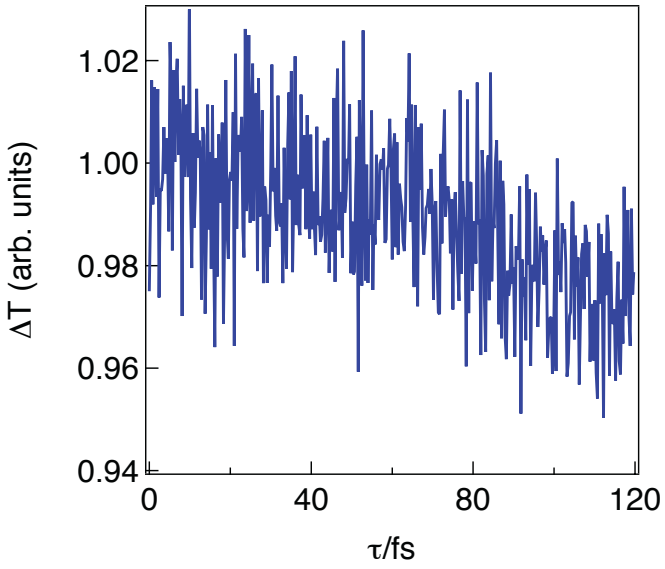

Figure 3.7 Time domain experimental PS signal trace for probe =580 nm, pump = 480 nm (blue).

Shown in Figure 3.7 is an experimental trace of a τ scan on the quantum dot system performed with 100 fs pump pulses centered at 480 nm. The pump-probe delay time (ΔT) was 2.5 ps – well outside the pulse-shaping window for a scan. The probed wavelength was λ_{probe} = 580 nm. Shown in Figure 3.8 are the power spectra of this experimental trace (blue) as well as the theoretical signal traces seen in Figure 3.6 generated with the modified coherent model. Note that for the simulated data, the pump duration was set to 100 fs FWHM, reflecting the experimental conditions. The power spectra of the theoretical signal traces correspond to electronic dephasing rates, γ_e, of 0 fs^{-1}, .01 fs^{-1}, and .05 fs^{-1} in black, red, and green, respectively.

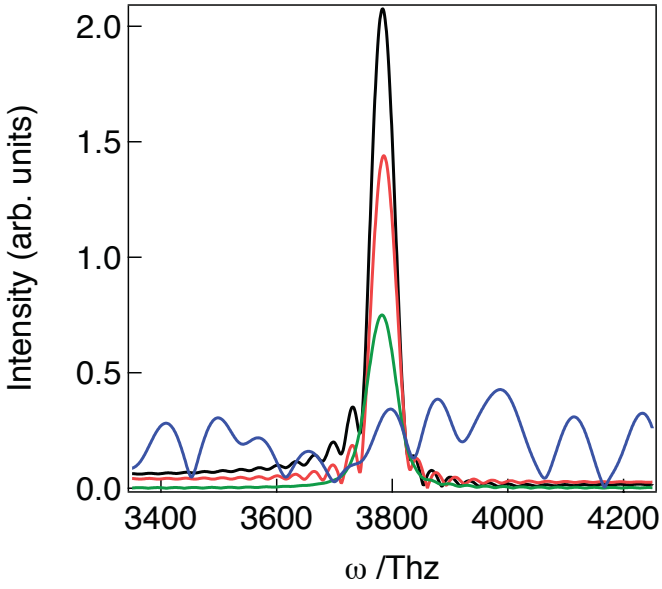

Figure 3.8 Frequency domain of signal trace for probe =580 nm, pump = 480 nm. Also shown are simulated signals with electronic dephasing rate constants, γ_e, of 0 ps^{-1} (black), 10 ps^{-1} (red), 50 ps^{-1} (green).

The clear lack of a transformable signal at the fundamental frequency or second harmonic (not shown) of the excitation pulse shows that coherent coupling to the system is not occurring. We found similar results under a wide range of conditions. Experiments performed with different pump wavelengths all showed negative results, as did

experiments that probed states accessible by different visible transitions or by the near IR idler probe beams.

This lack of evidence for coherent coupling suggests that dephasing in these systems is occurring much faster than the pulse length of the excitation source. Though we have assumed the coherent biexciton model as a guide for the expected behavior of the experimental system, as is shown in Chapter 5, even the simplest two level model exhibits a recoverable peak in the power spectrum at twice the optical frequency if memory of the excitation is maintained for a timescale comparable to the pulse length. Consequently, based on the known pump pulse duration and by comparison of the experimental and theoretical power spectra, we can set a lower bound on the rate of electronic dephasing. The results show that in this case, electronic dephasing is likely occurring faster than 50 fs. Given this timescale, attempts at coherent control with 100 fs excitation pulses are highly unlikely to yield informative results. The pulses generated with the TOPAS were simply too long to successfully affect the quantum yield of the excited state products, and consequently, no information could be gained informing how those product states are formed. In order to gain more insight into the timescale of the photophysics involved with nanocrystal excitation, better time resolution was necessary so that ultrafast relaxation processes could be observed and influenced.

To this end, we retooled our lab with a homebuilt NOPA capable of producing tunable pulses with durations of 35 fs FWHM and reexamined the quantum dot system with the improved time resolution. Initial pump probe spectroscopy in the visible showed Raman active modes in the tetrachloroethylene used as a suspending liquid contributed strongly to the detected signal. Unfortunately, contributions from solvent Raman active

modes were difficult to disentangle from the exciton dynamics being studied. Further, Raman processes are sensitive to the phase of the excitation pulse and decay on similar time scales as the Auger dynamics in quantum dots, which severely complicates coherent control schemes. [33, 34] To eliminate any possible artifacts we suspended the nanocrystals in N-hexane, which has a much weaker Raman response. As expected, the quantum dots exhibited the same kinetic behavior in this suspending liquid and showed minimal contribution from the solvent Raman response.

Sinusoidal spectral phase modulation was initially employed here to determine whether the system was controllable with the shortened pump pulse duration achieved with the NOPA. We further developed a phase cycling scheme (described in detail in Chapter 5) that allowed separation of the oscillating components, which arise from wavepacket interference, from the background signal, which is generated by incoherent, phase-insensitive linear absorption. This dramatically improved the detection limit of the technique. It is the phase-sensitive component whose power spectrum is plotted in Figure 3.9 for experimental and theoretical signal traces. In all cases, the signal is normalized to the absolute value of the total signal size before Fourier transform. The experimental data shown was collected at T = 4.6 ps, λ_{probe} = 600 nm using a 500 nm pump beam which was determined by autocorrelation to be 35 fs FWHM.

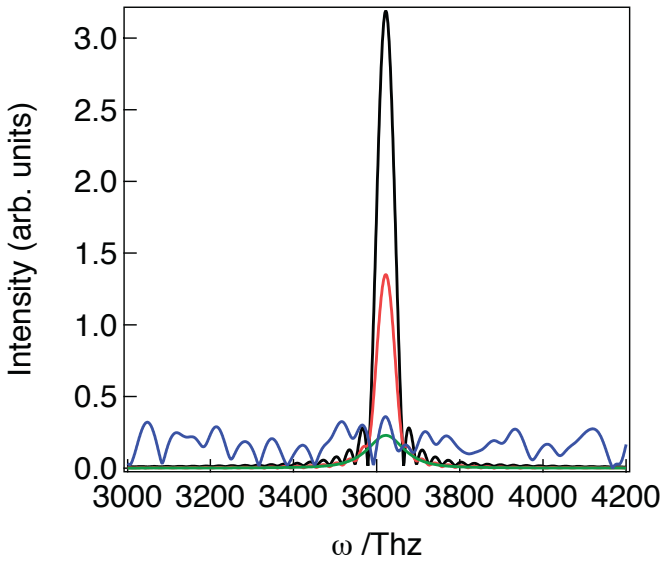

Figure 3.9 Power spectrum of experimental τ-scan signal trace with 35 fs FWHM excitation pulses centered at 500 nm (purple). Also shown are power spectra of theoretical signal traces based on interaction with the coherent biexciton model given a pulse length of 35 fs and electronic dephasing rate constants of 0 fs^{-1} (black), .01 fs^{-1} (red), and .05 fs^{-1} (green).

As is seen, there is no evidence for coherent coupling to the excited state surface with the excitation beam. Such coupling would appear as a peak rising above the noise of the measurement at the frequency of the pump field. It is often the case that more complex peak structure can arise in certain circumstances indicating, for example, coupling to dark excited states such as in Figure 3.5, or optical coupling to multiple vibrational levels on the ground or excited state surfaces. However, as mentioned above, even in the simplest model of a two level system, some indication of coherent system-field coupling can be seen in the power spectrum of the signal trace if interaction with the electronic coherence is possible (See Chapter 5).

Regardless of the specific characteristics of the system subject to such pulse shaping methods, the only case in which some peak structure would not be recoverable from the signal trace is if the excited state and ground state dephase on a timescale that is much faster than the optical pulse length. This can occur only if the bright electronic state to

which the system is initially excited changes in character very quickly. Therefore, all experimental data suggest that the timescale of the excited state dephasing with respect to the ground state surface is occurring faster than 20 fs. Such a fast dephasing timescale means that without employing optical pulses shorter than 20 fs, there is little hope of coherently controlling this system to favor multiple exciton generation or learn any information beyond the upper limit timescales involved, a result supported by recent work in several groups. [35-37]

There are some conclusions that may be drawn based on the experimental and theoretical work described. The very fast dephasing times that are likely responsible for the data presented suggest that the initial excited state formed upon absorption of a photon is very quickly perturbed by coupling to its environment. What this means for the exact mechanism of MEG remains unclear. The very fast dephasing time suggests that the incoherent mechanism is a likely contributor to the observed enhanced yield of excitons in these systems as the more elaborate mechanisms require some finite amount of time during which a coherence lives. The coherent model of Shabaev et al. is a viable description of the dynamics, but the timescales of the model as presented in the original paper are likely at least an order of magnitude too long to be relevant to the experimentally observed behavior. Finally, the direct mechanism of Klimov and coworkers is a possibility, however, the coupling term between the virtual single exciton states and the multiexciton states would need to be very large to efficiently transfer amplitude during the very short coherence time.

3.5 References Cited

1. A. Nozik, "Quantum dot solar cells," Physica E: Low-dimensional Systems and Nanostructures (2002).

2. R. Schaller and V. Klimov, "High efficiency carrier multiplication in PbSe nanocrystals: Implications for solar energy conversion," Physical Review Letters **92**(2004).

3. R. Ellingson, M. Beard, J. Johnson, and P. Yu, "Highly efficient multiple exciton generation in colloidal PbSe and PbS quantum dots," Nano Lett (2005).

4. A. J. Nozik, M. C. Beard, J. M. Luther, M. Law, R. J. Ellingson, and J. C. Johnson, "Semiconductor Quantum Dots and Quantum Dot Arrays and Applications of Multiple Exciton Generation to Third-Generation Photovoltaic Solar Cells," Chemical Reviews **110**, 6873-6890 (2010).

5. V. Klimov, "Spectral and dynamical properties of multilexcitons in semiconductor nanocrystals," Annual Review of Physical Chemistry **58**, 635-673 (2007).

6. V. Klimov, "Mechanisms for photogeneration and recombination of multiexcitons in semiconductor nanocrystals: Implications for lasing and solar energy conversion," Journal Of Physical Chemistry B **110**, 16827-16845 (2006).

7. R. D. Schaller, V. M. Agranovich, and V. I. Klimov, "High-efficiency carrier multiplication through direct photogeneration of multi-excitons via virtual single-exciton states," Nature Physics **1**, 189-194 (2005).

8. A. Shabaev, A. L. Efros, and A. J. Nozik, "Multiexciton generation by a single photon in nanocrystals," Nano Lett **6**, 2856-2863 (2006).

9. A. Franceschetti, J. An, and A. Zunger, "Impact ionization can explain carrier multiplication in PbSe quantum dots," Nano Lett (2006).

10. Y. Silberberg and D. Meshulach, "Coherent quantum control of two-photon transitions by a femtosecond laser pulse," Nature (1998).

11. D. Meshulach and Y. Silberberg, "Coherent quantum control of multiphoton transitions by shaped ultrashort optical pulses," Physical Review A (1999).

12. T. Brixner, N. Damrauer, and G. Gerber, *Femtosecond quantum control*, Advances in Atomic, Molecular, and Optical Physics, Vol 46 (2001), Vol. 46, pp. 1-54.

13. J. Herek, W. Wohlleben, R. Cogdell, D. Zeidler, and M. Motzkus, "Quantum control of energy flow in light harvesting," Nature **417**, 533-535 (2002).

14. T. Brixner, N. Damrauer, B. Kiefer, and G. Gerber, "Liquid-phase adaptive femtosecond quantum control: Removing intrinsic intensity dependencies," Journal Of Chemical Physics **118**, 3692-3701 (2003).

15. W. Wohlleben, T. Buckup, J. Herek, and M. Motzkus, "Coherent control for spectroscopy and manipulation of biological dynamics," Chemphyschem **6**, 850-857 (2005).

16. M. A. Montgomery, R. R. Meglen, and N. H. Damrauer, "General Method for the Dimension Reduction of Adaptive Control Experiments," The Journal of Physical Chemistry A **110**, 6391-6394 (2006).

17. M. A. Montgomery and N. H. Damrauer, "Elucidation of Control Mechanisms Discovered during Adaptive Manipulation of [Ru(dpb) 3](PF 6) 2Emission in the Solution Phase," The Journal of Physical Chemistry A **111**, 1426-1433 (2007).

18. M. P. A. Branderhorst, P. Londero, P. Wasylczyk, C. Brif, R. L. Kosut, H. Rabitz, and I. A. Walmsley, "Coherent control of decoherence.," Science **320**, 638-643 (2008).

19. M. A. Montgomery, E. M. Grumstrup, and N. H. Damrauer, "Fourier transform spectroscopies derived from amplitude or phase shaping of broadband laser pulses with applications to adaptive control," Journal Of The Optical Society Of America B-Optical Physics **27**, 2518-2533 (2010).

20. T. Kobayashi and A. Shirakawa, "Sub-10-fs tunable pulses in visible and NIR and visible sub-5-fs pulses generated by noncollinear OPA," Journal of Luminescence **87**, 119-120 (2000).

21. J. Piel, M. Beutter, and E. Riedle, "20-50-fs pulses tunable across the near infrared from a blue-pumped noncollinear parametric amplifier," Optics Letters **25**, 180-182 (2000).

22. T. Feurer and A. Glass, "Two-photon photoconductivity in SiC photodiodes and its application to autocorrelation measurements of femtosecond optical pulses," Applied Physics B-Lasers And Optics (1997).

23. T. Buckup, T. Lebold, A. Weigel, W. Wohlleben, and M. Motzkus, "Singlet versus triplet dynamics of beta-carotene studied by quantum control spectroscopy," Journal of Photochemistry and Photobiology a-Chemistry **180**, 314-321 (2006).

24. J. Hauer, T. Buckup, and M. Motzkus, "Quantum control spectroscopy of vibrational modes: Comparison of control scenarios for ground and excited states in beta-carotene," Chemical Physics **350**, 220-229 (2008).

25. E. M. Grumstrup, J. C. Johnson, and N. H. Damrauer, "Enhanced triplet formation in polycrystalline tetracene films by femtosecond optical-pulse shaping," Physical Review Letters **105**, 257403- (2010).

26. P. Brumer and M. Shapiro, "Control of unimolecular reactions using coherent light," Chem. Phys. Lett. **126**, 541-546 (1986).

27. M. Shapiro and P. Brumer, "Laser control of product quantum state populations in unimolecular reactions," Journal Of Chemical Physics **84**, 4103-4104 (1986).

28. V. Klimov, J. McGuire, R. Schaller, and V. Rupasov, "Scaling of multiexciton lifetimes in semiconductor nanocrystals," Physical Review B **77**(2008).

29. E. M. Grumstrup, S.-H. Shim, M. A. Montgomery, N. H. Damrauer, and M. T. Zanni, "Facile collection of two-dimensional electronic spectra using femtosecond pulse-shaping technology," Optics Express **15**, 16681-16689 (2007).

30. W. Press, S. Teukolsky, S. Vetterling, and B. Flannery, *Numerical Recipes: The art of Scientific Computing* (2007).

31. R. W. Boyd, *Nonlinear optics,* Third ed. (Elsevier/Academic Press, Amsterdam, 2008), p. xx+613.

32. A. V. Pisliakov, T. s. Mančal, and G. R. Fleming, "Two-dimensional optical three-pulse photon echo spectroscopy. II. Signatures of coherent electronic motion and exciton population transfer in dimer two-dimensional spectra," The Journal of Chemical Physics **124**, 234505 (2006).

33. N. Dudovich, D. Oron, and Y. Silberberg, "Single-pulse coherently controlled nonlinear Raman spectroscopy and microscopy," Nature **418**, 512-514 (2002).

34. T. Polack, D. Oron, and Y. Silberberg, "Control and measurement of a non-resonant Raman wavepacket using a single ultrashort pulse," Chemical Physics **318**, 163-169 (2005).

35. B. Cho, W. K. Peters, R. J. Hill, T. L. Courtney, and D. M. Jonas, "Bulklike Hot Carrier Dynamics in Lead Sulfide Quantum Dots," Nano Lett **10**, 2498-2505 (2010).

36. H. Kamisaka, S. V. Kilina, K. Yamashita, and O. V. Prezhdo, "Ultrafast vibrationally-induced dephasing of electronic excitations in PbSe quantum dot," Nano Lett **6**, 2295-2300 (2006).

37. S. Kilina, C. Craig, D. Kilin, and O. Prezhdo, "Ab initio time-domain study of phonon-assisted relaxation of charge carriers in a PbSe quantum dot," Journal of Physical Chemistry C (2007).

CHAPTER 4

ENHANCED TRIPLET FORMATION IN TETRACENE THIN FILMS BY FEMTOSECOND OPTICAL PULSE SHAPING

4.1 Introduction

Light absorption by semiconductors typically produces excitonic states whose dissociation into free carriers is vital for the generation of electrical or chemical work. In certain cases, correlated electron dynamics result in the formation of multiple excitons per absorbed photon. While these physics have been known for several decades in both inorganic [1, 2] and organic materials [3, 4], their practical impact on solar energy conversion has only recently been pursued. [5-7] In conceptual systems based on simple device architectures, the creation of multiple carriers per photon leads to significantly higher efficiencies (~ 46%), well above the thermodynamic limit of 31% imposed on single junction devices that do not exploit these physics. [1, 8] As a consequence, intense research efforts are now under way to understand both the electron and nuclear dynamics that control reaction rates and branching ratios during multiple exciton generation in order to inform the design of new platforms for solar photoconversion.

Within polyacene organic crystals such as pentacene (Pc), tetracene (Tc), and anthracene, the formation of multiple excitons has been observed as *singlet fission* (SF)

(shown schematically in **Figure 4.1**) wherein an optically bright singlet exciton (S_1) internally converts to a new singlet state ^{1}(TT), which consists of a pair of spin-opposed triplets on different chromophores. [7, 9]

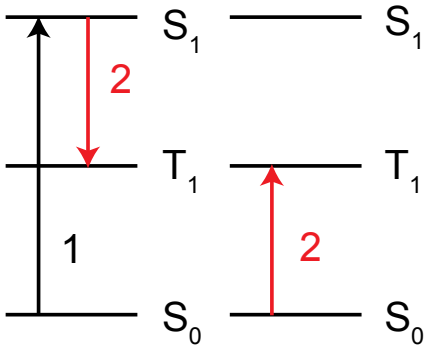

Figure 4.1 Singlet fission: (1) initial optical excitation on one of the chromophores creates a singlet exciton. (2) The excited chromophore relaxes, simultaneously exciting the other chromophore with the product being a T_1 on each.

Once formed, rapid triplet diffusion, dephasing, and thermalization compete with T–T annihilation that would re-form the S_1 state. This process is typically described by a kinetic scheme of the form:

$$S_1 \rightleftharpoons {}^1(TT) \rightleftharpoons 2T_1$$

where T_1 is an uncorrelated triplet state.

The efficiency of SF in organic crystals is sensitively dependent on the relative energies of the S_1 and T_1 states (see **Figure 4.2** for energy level diagrams for the polyacene series). [4, 7] While SF in Pc is exothermic and is the dominant relaxation pathway, in single-crystal Tc it is believed ^{1}(TT) lies slightly higher in energy (literature numbers vary from 0.022 eV to 0.237 eV) than S_1 so that SF must be thermally activated from its equilibrium position. Nevertheless, the rate constant for SF at room temperature is large resulting in a low fluorescence quantum yield and an S_1 lifetime of ~ 100 ps. [10, 11]

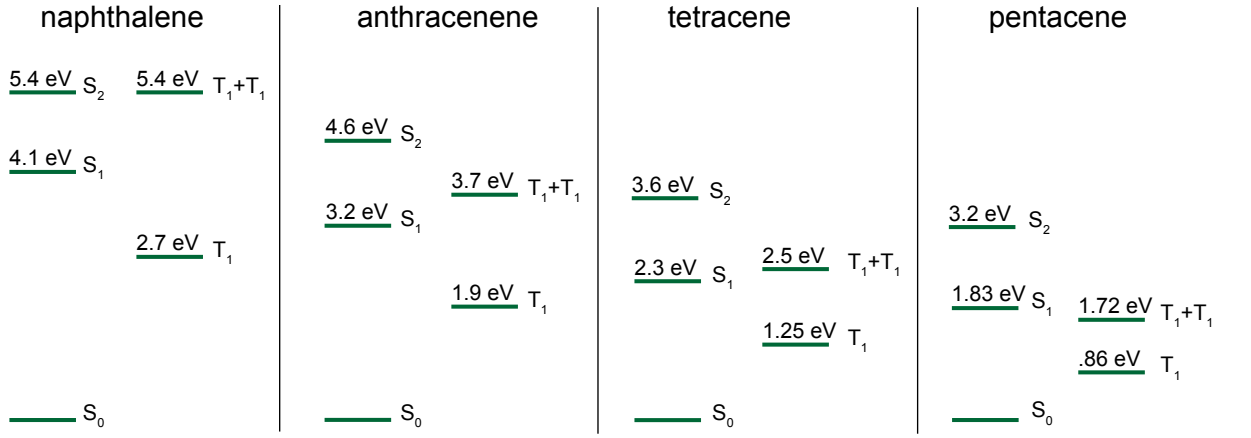

Figure 4.2 Energy level diagrams for polyacene series from naphthalene to pentacene. These data are from crystal and solution measurements.

The occurrence of SF in single crystals of Tc and Pc is no longer disputed, however its underlying mechanisms are still poorly understood. [7, 12, 13] This chapter reports a previously published study [14] of SF pathways in polycrystalline tetracene thin films using tools of ultrafast pump probe spectroscopy and open and closed loop coherent control methods achieved through optical pulse shaping.

As SF in Tc is an activated process in competition with, amongst other pathways, fluorescence, the control experiments were designed to alter the branching ratio of the photoexcited system. A search parameter space inclusive of trains of ~ 30 fs visible laser pulses was used to identify optimal fields that improve triplet yield by up to 20%. It is shown that pulse trains result in an enhancement of triplet yield and not just S_1 population, and further, the optimal fields appear to interact with low frequency intermolecular modes while exploiting these motions and/or the geometries they achieve to affect the SF process.

4.2 Experimental and Characterization

Polycrystalline tetracene thin films of ~ 80 nm thickness were grown using a standard thermal evaporation route and characterized with UV-Vis absorption, x-ray

diffraction, and atomic force microscopy (AFM). In these films individual crystallites (see **Figure 4.3**) grow with the *ab* plane of the unit cell parallel to the optically transparent 1 mm glass substrate surface but randomly oriented with respect to neighboring crystallites. [15] This was confirmed by the isotropic response to multiple polarizations of incident light in UV-Vis absorption spectra, as well as a diffraction pattern (**Figure 4.4**) showing only (00l) peaks.

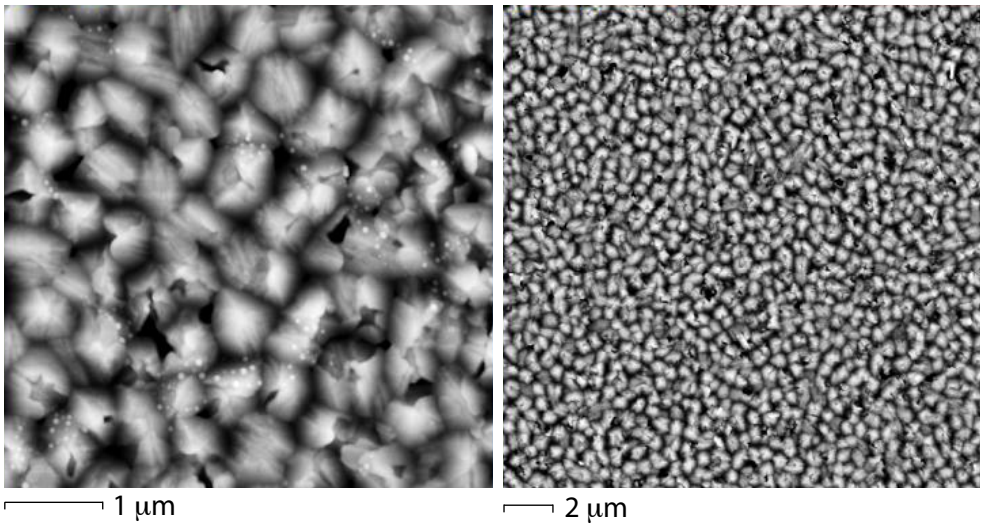

Figure 4.3 AFM images of the studied film. Individual crystallites, which are ~ 500 nm in diameter, have the *ab* plane parallel to the substrate, however are randomly oriented with respect to each other.

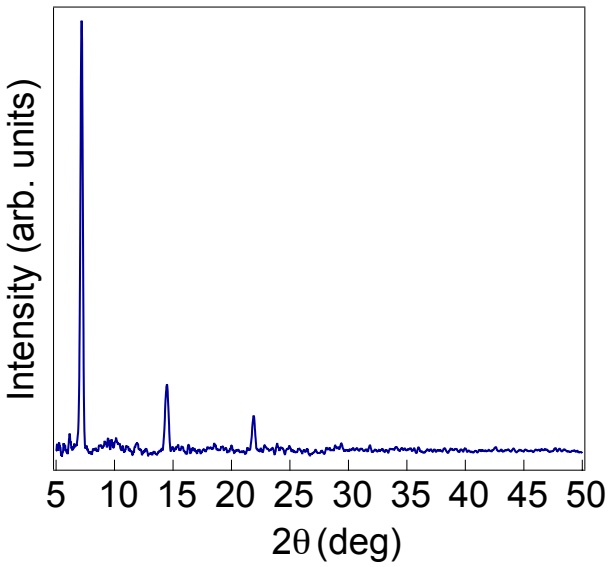

Figure 4.4 Glancing angle X-ray diffraction pattern of the film studied in this work. The peaks are all indexed to the (00l) (l=1,2,3) plane.

A 1 kHz (ν_f) pulse train centered at 800 nm (50 fs FHWM) was derived from a Quantronix Odin Ti:Sapphire multipass amplifier seeded by K&M Labs MTS mini oscillator. Approximately 200 μJ of the available 1 mJ was used to pump a homebuilt noncollinear optical parametric amplifier (NOPA) with a series of irises to ensure a high quality spatial mode.[16, 17] In this work, the NOPA was tuned to ~530 nm. The resultant visible pulse train was compressed with a pair of fused silica prisms and then passed through the pulse shaper which consists of a home built, all reflective zero-dispersion compressor [18] with a dual mask CRI 640 spatial light modulator (SLM) at the Fourier plane. The output of the pulse shaping apparatus was mechanically chopped at $\nu_f/2$, attenuated to 50 nJ/pulse, and focused onto the sample with a 125 mm lens (200 μm spot diameter). Autocorrelation was performed at the sample position (30 fs FWHM) and the prisms were adjusted until the pulses were near transform limited. [19] The probe beam was produced in a sapphire window, compressed with a BK7 single prism compressor and focused with the same lens

as the pump beam at an angle of ~ 7°. Pump and probe beams were orthogonally polarized to minimize detection of scattered pump light. The probe was spectrally resolved in an Acton 2300i monochromator. The detected signal was coupled to a Stanford Research SR250 boxcar integrator and the output detected at 500 Hz with a Stanford Research SR810 lockin amplifier. To maintain an inert environment during measurement, the film was placed in a quartz cell fitted with a teflon cap and connected to a source continually flowing argon. The film was otherwise stored in a glovebox under a nitrogen atmosphere. For the closed-loop (adaptive) [20] and open-loop pulse shaping experiments a 3-parameter phase function was used (vide infra). The adaptive algorithm uses analogues of evolutionary strategies including mutation, crossover, and cloning to enhance a specified observable. [21]

For time resolved emission measurements, A Clark-MXR NJA-5 Ti:Sapphire oscillator operating at 100 Mhz repetition rate produced 200 fs FWHM laser pulses centered at 792 nm. The pulse train was frequency doubled in a BBO crystal, filtered with a neutral density filter to 1.5 pJ/pulse and focused normal to the film with a spot size diameter of ~ 100 μm. Spontaneous emission is collected with a collimating lens at an angle of ~35° from normal, passed through a double monochromator (Sciencetech 9030DS), and detected with a Hamamatsu R3809U-50 MCP-PMT. Time correlation is performed with a Becker & Hickl SPC-630 single photon counting module.

4.3 Spectroscopy

The films exhibit an electronic absorption spectrum (**Figure 4.5**) with properties resembling the constituent monomer; namely, a vibronic progression from ~ 400 – 500 nm with peak spacing of ~ 1400 cm^{-1} characteristic of a $\pi^* \leftarrow \pi$ transition of an aromatic species. Individual peaks, shifted and split due to Davydov coupling, shows that tetracene exhibits excitonic behavior typical of other polyacenes with two molecules per unit cell. [4] The peaks at ~ 505 nm and ~ 520 nm correspond to the Davydov doublet of the first vibronic band in the $S_1 \leftarrow S_0$ manifold of transitions. [22]

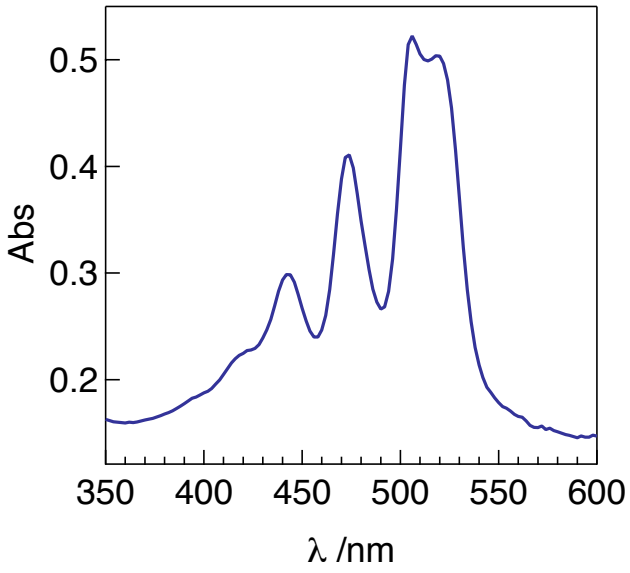

Figure 4.5 Absorption spectrum of the $S_1 \leftarrow S_0$ of 80 nm thick tetracene films on a glass substrate.

The time integrated spontaneous emission spectrum from the studied film is shown in **Figure 4.6** and is in good agreement with published data. [10, 23] The peak at 540 nm and the shoulder at 568 nm are the 0-0 and 0-1 transitions, respectively, of the free singlet exciton emission. The shoulder at 618 nm is likely due to a singlet trap site although the feature observed here is much less prominent than what has been reported for films on

HOPG. [23] The time resolved emission decay (red), detected at 540 nm, is shown in **Figure 4.7** along with a biexponential kinetics model (blue) that was comprised of a major (92%) component with a time constant of 75 ps, and a minor (8%) component with a time constant of 380 ps. The fast emission decay suggest that the primary decay pathways are non-emissive – a fact confirmed by quantum yield measurements that showed an emission quantum yield of ϕ_{em}=.009.

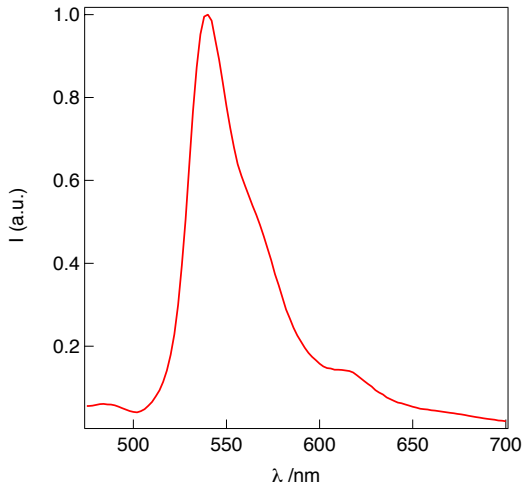

Figure 4.6 Spontaneous emission spectrum of the film studied in this work.

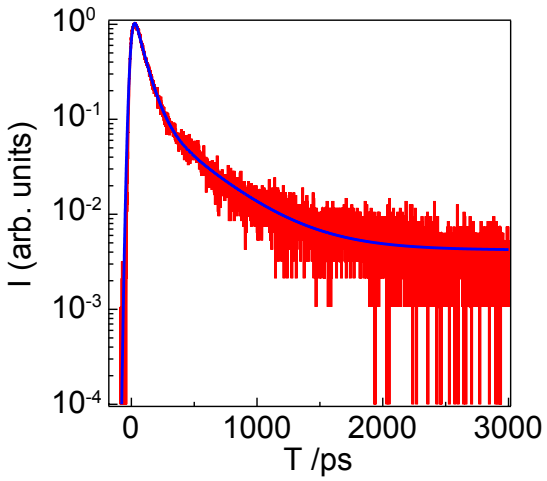

Figure 4.7 Time resolved spontaneous emission (red) at 540 nm from the polycrystalline tetracene film studied in this work. Time constants for the kinetics model (blue) were found to be 75 ps (92%) and 380 ps (8%).

Figure 4.8 shows a transient difference spectrum (bottom) of the film probed 100 ps after excitation along with the ground state absorption spectrum for comparison (**Figure 4.8**, top). An important attribute is the positive feature that peaks at ~ 495 nm, approximately coincident with the valley in the absorption spectrum between the first and second vibronic components. This excited state absorption also serves to diminish the bleach of the Davydov component at 505 nm.

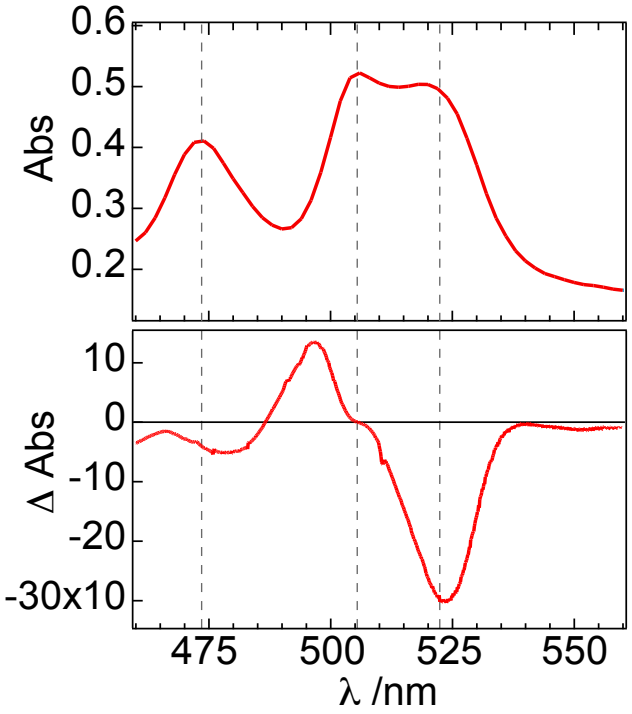

Figure 4.8 (Top) Absorption spectrum of tetracene films used in this work. (bottom) Transient absorption spectrum taken at T = 100 ps of the same film. Dotted lines are drawn for comparison.

Single wavelength transient kinetics (-ΔT) collected at λ_{probe} = 490 nm (**Figure 4.9**) show the absorption, which after an initial fast decay, rises with a time constant of ~ 40 ps and does not decay in the 1600 ps window of the instrument. The transient kinetics at λ_{probe} = 490 nm were also characterized on a ns-μs transient absorption instrument. The

absorptive feature at 490 nm (not shown) was found to decay biexponentially with time constants of 38 ns and 375 ns after excitation with an 8 ns pulse centered at 532 nm.

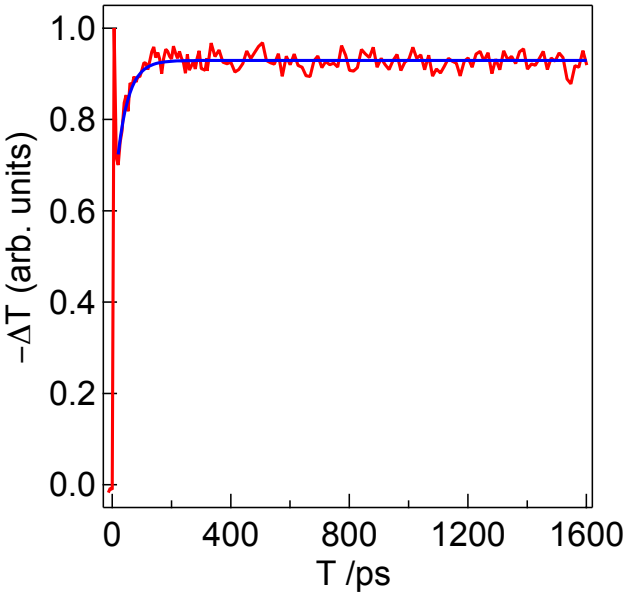

Figure 4.9 (red) Kinetics at 490 nm attributed to the triplet absorption. (blue) Overlay of a single exponential model with a rise time of 37.5 ps (see text)

Taken together, these nanosecond and ultrafast data are consistent with the feature at 495 nm being a signature of the lowest energy triplet (T_1) produced via SF. [3, 4] In support of this assignment, the triplet-triplet absorption spectrum reported for tetracene molecules in an ethanol/methanol glass (113 K) exhibits visible absorption features between 450 – 500 nm (corresponding to $T_n \leftarrow T_1$ (where n > 2) transitions) that are 1–2 orders of magnitude more intense than $T_2 \leftarrow T_1$ absorption features in the near infrared. [24]

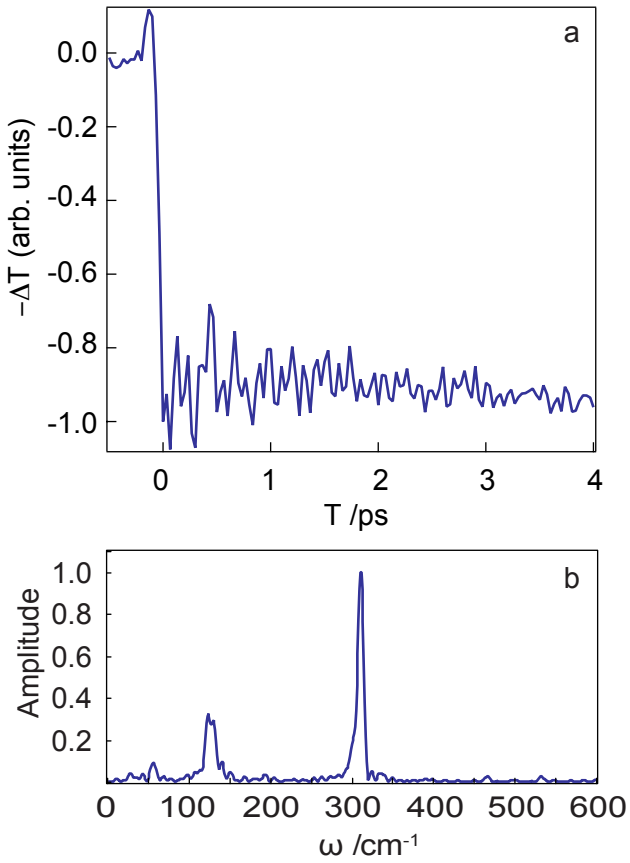

Figure 4.10 **a** Early time kinetics at 500 nm. **b** Power spectrum of residual after subtracting an exponential fit from the kinetic trace in a.

Transient kinetics collected over a shorter time window reveal the pump pulses coherently excite low-frequency vibrational motions in the tetracene thin films. **Figure 4.10** shows particularly well-resolved oscillations in probe transmission on a negative (bleach) signal collected at λ_{probe} = 500 nm[1]. Fourier transform (FT) of the oscillatory residual after subtraction of an exponential fit reveals three prominent features in the power spectrum (Figure 4.10 b): a band at 312 cm^{-1}, a pair of closely spaced (not fully resolved) bands at 123 cm^{-1} and 130 cm^{-1}, and a weak band at 58 cm^{-1}.

[1] Note that in **Figure 4.8** the transient signal at λ_{probe} = 500 nm is absorptive in nature, while the signal in **Figure 4.10** is a bleach. This discrepancy is simply because the T_1 state is not yet fully evolved within the short, early time temporal window of the data shown in **Figure 4.10**.

Published Raman studies of the Tc single crystal show a band within 5 cm^{-1} of the 312 cm^{-1} mode observed here [25] which can be assigned as intramolecular in nature based on comparison with experimental studies of the monomer [26] as well as theoretical studies, which suggest the mode involves a breathing of the monomer along its long axis. [25, 27] The three lowest frequency bands that were observed are also in good agreement with Raman transitions reported for single crystal tetracene at room temperature. [25, 28-30] Venuti et al. have compared experimental data with lattice dynamics calculations and shown that modes below 140 cm^{-1} are due to intermolecular lattice vibrations. [30] The favorable agreement between the frequencies observed in the transient absorption transient absorption trace and reported Raman data suggests the transient absorption oscillations are due to ground state vibrational motions coherently excited under the pump envelope.

To further support the assignment that these are ground state vibrational motions, transient absorption traces were collected with pump pulses shaped to have either positive or negative chirp. In the time domain, positive (negative) chirp means the lower (higher) energy colors of the pulse precede the higher (lower) energy colors in time. In a classical picture, the initial wavepacket follows the gradient of the excited state surface, and therefore, a positively chirped pump pulse should have a lower probability of interacting with the excited-state wavepacket as it evolves in time, assuming the usual circumstance that the energy gap between ground and excited states decreases along the reaction coordinate. [32, 33] If a certain vibrational motion observed in a transient absorption trace is constrained to the ground state surface, the positively chirped pump pulse has a lower likelihood of creating a ground state vibrational superposition. If, however, the vibrational

motion is confined to the excited state surface, the positively chirped pulse should create a similar wavepacket as the negatively chirped pulse. Shown in **Figure 4.11** are the FTs of the residual after an exponential fit of λ_{probe} = 500 nm kinetic traces for a pump pulse with spectral chirp equal to (a) 0 fs^2, (b) +550 fs^2 , and (c) -550 fs^2. As can be seen, the positively chirped pump almost completely eliminates any sign of vibrational motion in the kinetics trace. The negatively chirped does show a reduction in amplitude of the peaks, but this decrease is attributed to the temporally longer pump envelope. These observations indicate that the coherent vibrational motion seen in the kinetics traces is a ground state phenomenon. Though comparison with the negatively chirped pulse suggests the majority of the amplitude arises from ground state motions, the lower frequency peaks do have some remaining amplitude for the positively chirped pump indicating that there may be some contribution from an excited state vibrational coherence. This is an especially interesting observation in light of recent ab-initio calculations by Zimmerman which suggest lattice modes in a 32-mer of tetracene at 124 cm^{-1}, 127 cm^{-1}, and 129 cm^{-1} couple states of S_1 and double triplet ^{1}(TT) character. [31]

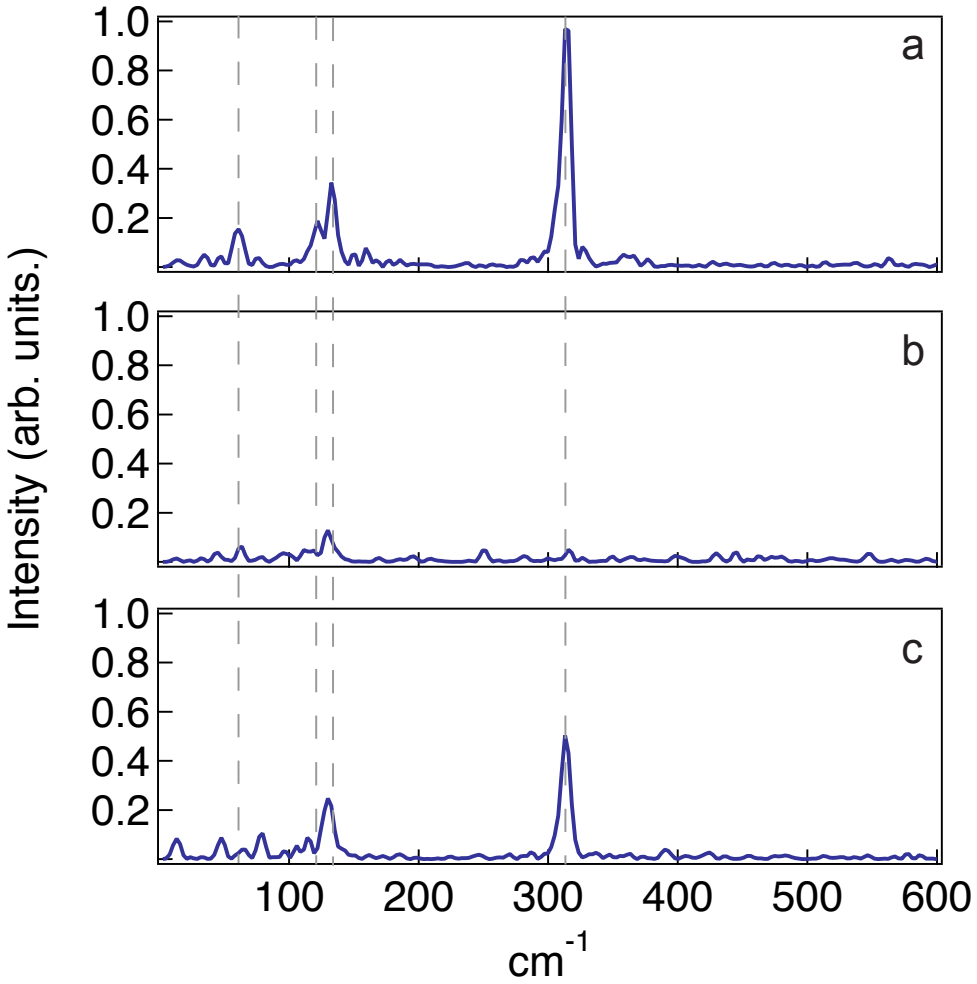

Figure 4.11 FT of residual at λ_{probe} = 500 after subtraction of a single exponential for (a) unshaped pump, (b) +550 fs^2 chirped pump, and (c) -550 fs^2 chirped pump.

4.4 Coherent Control

In efforts to manipulate the magnitude of spectral components of the system, adaptive (closed-loop) control experiments with an automated broad-band laser pulse shaper were performed. [20] Based on precedent set in our lab and the literature for controlling nuclear motions, the variable space sampled by the genetic algorithm was restricted to use of a 3-parameter (α, τ, and ϕ) frequency (ω_n)-dependent sinusoidal phase function, [34-37]

$$P(\omega_n) = \alpha[\cos(\omega_n \tau + \phi) + 1]. \qquad [4.1]$$

In the time domain, the search space explored with this phase function is a family of pulse trains in which α controls the number and relative height of evenly spaced sub-pulses and τ controls the temporal separation between sub-pulses (see a more complete development of this topic in Chapter 5). The parameter ϕ controls the relative temporal phase between sub-pulses. This phase can be understood as a shift in the carrier frequency of each subpulse relative to the unshaped pulse. It should be noted that because phase alone is manipulated, each pulse train within the family of possibilities has the same fluence at the sample. This includes the unshaped pulse produced when α = 0 or when τ = 0. **Figure 4.12** shows an intensity autocorrelation of an example pulse train with α = 1.25 and τ = 225 fs. To minimize unwanted pulse shaping artifacts due to phase wrapping and SLM pixilation effects [38, 39] (also, see Chapter 2), α was constrained to $[-\pi, +\pi]$ and τ to $[-1000 \text{ fs}, +1000 \text{ fs}]$.

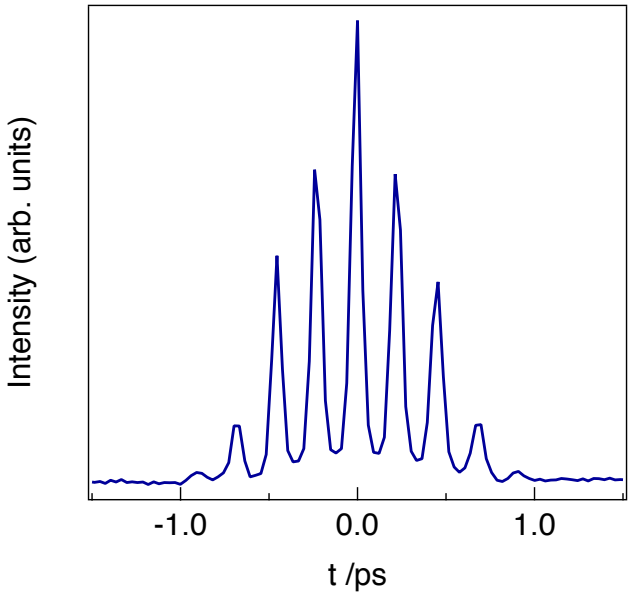

Figure 4.12 Autocorrelation of the pulse train produced by application of Equation 1 with α = 1.25 and τ = 225 fs.

Figure 4.13 shows the results of a typical adaptive optimization experiment in which transient absorption was used to probe population (λ_{probe} = 490 nm) 1500 ps after the arrival of the pump in the sample (ΔT = 1500 ps) while the genetic algorithm, parameterized by Equation 4.1 and with a fitness goal of maximizing this signal, converged on the optimal set (or sets) of solutions. The comparison of the generation average (50 different pulses) with the signal due to an unshaped pulse (once per generation) shows clear evidence that the adaptive algorithm is increasing 490 nm absorption within the parameter space afforded by Equation 4.1, which again, does not affect laser fluence at the sample. The simulated intensity profile of the optimal pulse discovered in this particular experiment (shown in blue in **Figure 4.17**(right)) has τ = 450 fs and α = 2.6. The value of ϕ is not reported for any of the optimal solutions because no correlation has been observed between its value and pulse fitness.

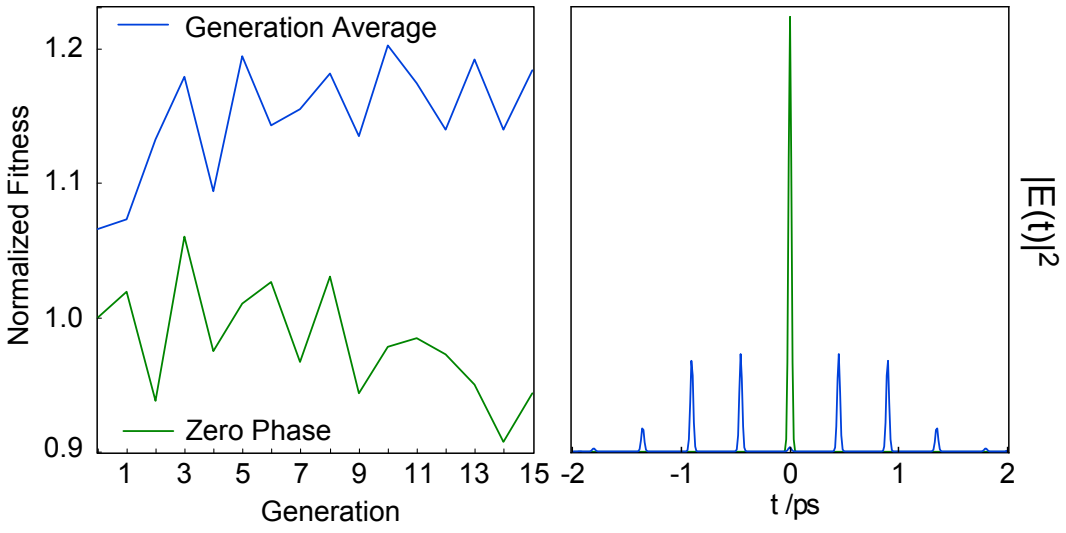

Figure 4.13 (left) Optimization curves of the λ_{probe} = 490 nm absorption. In blue is the generational average of the entire population and in green is the unshaped, zero-phase control pulse recorded once per generation. (right) Simulated electric field intensity for unshaped (green) and optimal (blue) pulses. The optimal pulse has τ = 450 fs and α = 2.6.

Examples of single wavelength kinetics collected following excitation with an optimal pulse shape versus an unshaped pulse are shown in **Figure 4.14** where it can be seen that differences in the λ_{probe} = 490 nm absorption for the two pulses are evident at early times and persist for as long as our measurement can be made.

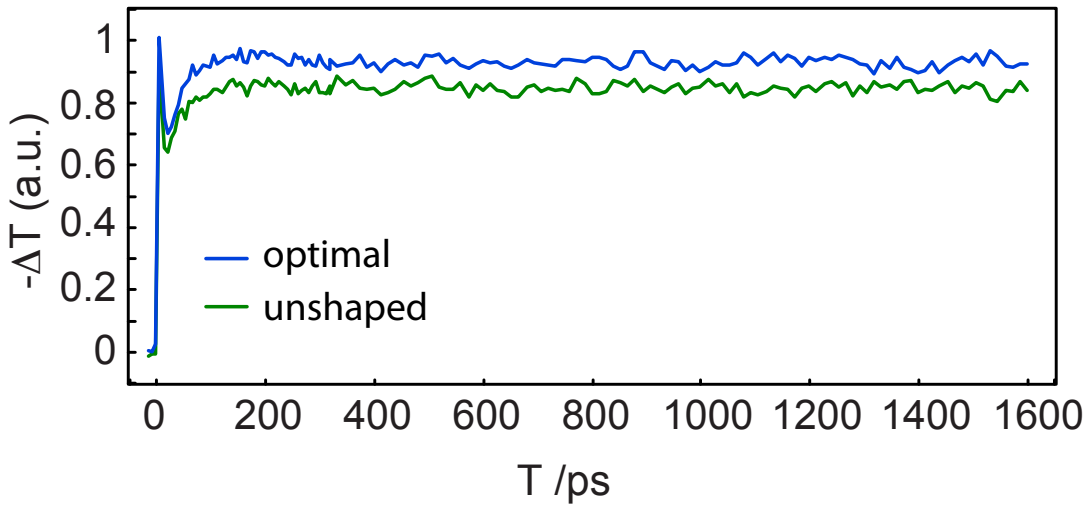

Figure 4.14 Kinetics at λ_{probe} = 490 nm for an unshaped pump pulse (green) and optimal pulse (blue) from optimization shown in **Figure 4.13**.

A second optimization, this time of the 505 nm bleach at ΔT = 4 ps, resulted in two similar classes of optimal pulse trains which yielded the same fitness for the observable: 1) τ = 450 fs, α = 2.5 and 2) τ = 225 fs, α = 2.5. Note that pulse trains with τ = 450 fs are ones in which each pulse arrives at half the frequency of pulse trains with τ = 225 fs. This insight led to the examination of early-time kinetics to determine if the optimal pulses affected the vibrational dynamics previously observed with unshaped pulses. Shown in **Figure 4.15** is the power spectrum of the oscillatory residual from a fit of early-time kinetics collected at λ_{probe} = 505 nm following excitation with both unshaped and optimally shaped pulses. In **Figure 4.15**a is the spectrum normalized to the maximum peak at ~312 cm^{-1} for unshaped pulse excitation. Shown in **Figure 4.15**b is the spectrum recovered when the pump is

shaped with parameters τ = 225 fs and α = 2.5, normalized to the same value as **Figure 4.15** a. What the data indicate is that the shaped pulses, which increase the yield of the bleach at 505 nm, also appear to selectively enhance low frequency intermolecular motions and suppress the high frequency intramolecular 312 cm^{-1} mode.

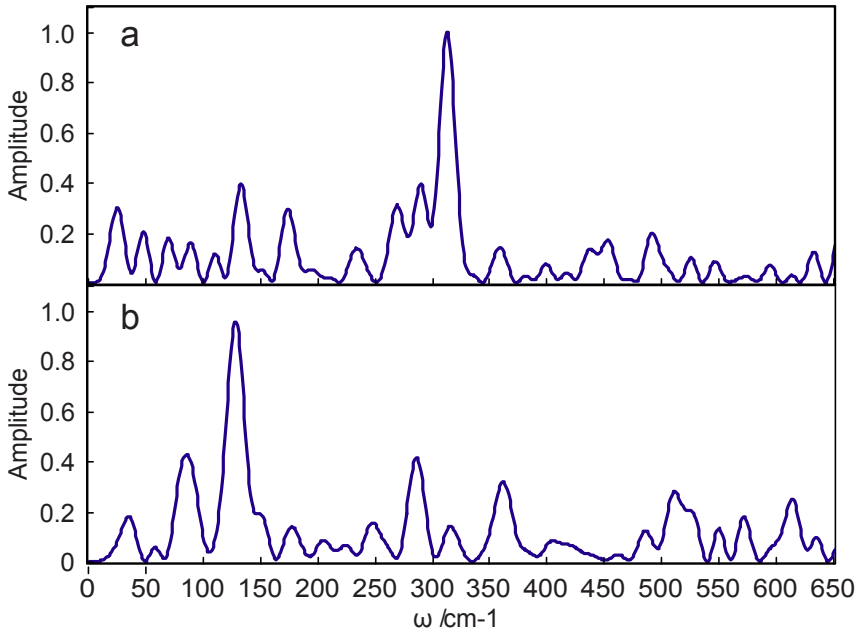

Figure 4.15 **a** Spectrum obtained from λ_{probe} = 505 nm early time dynamics with unshaped excitation. **b** Same spectrum, but with pulse train excitation given by τ = 225 fs, α = 2.5.

It should be noted that there are some difficulties associated with determining the amplitude of the coherent motion in the sample when pulse trains are used for excitation. Since the T = 0 point is no longer well defined (see Chapter 5), it is necessary to fit and FT only the portion of the kinetics trace after the pump pulse has interacted with the sample, otherwise the dynamics are not reflective of the field-free behavior. As a consequence, some caution should be maintained when interpreting **Figure 4.15**. Nevertheless, the implication of the data, namely that pulse trains that were successful in creating a greater population were also preferentially activating specific modes, led to the examination of how certain pulse trains, timed to the frequency of the motions known to be active in the

ground state, affected the triplet population. When these tests were performed, it was found that excitation by pulse trains with τ = 107 fs –in order to match the period of the 312 cm^{-1} oscillation seen in **Figure 4.10**– showed little or no enhancement of the transient absorption signal size as measured at 490 and 495 nm. On the other hand when pulse trains were applied to match the period of the 123 cm^{-1} mode, control was observed that was comparable to what the algorithm achieved. This data suggests that specific modes play an active role in the observed control of the 490 and 495 signals.

The vibrational quantum beats shown in **Figure 4.10** and **Figure 4.15** as well as convergence of the adaptive optimizations on pulse trains of similar character for both the bleach and absorptive signals raises further questions about the nature of the observed control. Namely, does excitation with a pulse train increase the extent of population transfer between ground state (GS) and excited states (ES) exclusively, or does it additionally control triplet yield? These must be distinguished because of results recently reported by Motzkus and coworkers on methanol solutions of the laser dye Nile Blue where it was shown that low fluence pulse trains (also created by a sinusoidal modulation of phase in a pulse shaper) enhance excited state population transfer relative to that achieved with a transform-limited pulse. [40, 41] Enhancement is achieved (they show 11% under their conditions) when the inter-pulse timing is matched to the period of a coherently-excited vibrational motion.

To confirm that enhancement of GS → ES population transfer was occuring, comparisons were made for difference spectra collected following excitation with pulse trains versus those due to the unshaped pulses. One such comparison is shown in **Figure 4.16** for ΔT = 100 ps. Here the parameters of the shaped pulse were α = 2.5, τ = 225 fs, and

ϕ = 0 with the inter-pulse timing being chosen to match the class of pulses discovered in the second set of adaptive experiments discussed above. As expected, both an enhancement of the absorption band peaked at 495 nm as well as the bleach signal at 505 nm were observed; a result consistent with the increased yields exhibited by the adaptive control results (note the 505 bleach has largely decayed by 100 ps in Figure 4.16). Spectral comparisons at ΔT = 5 and 10 ps show similar behavior for the bleach and absorptive features of the spectrum.

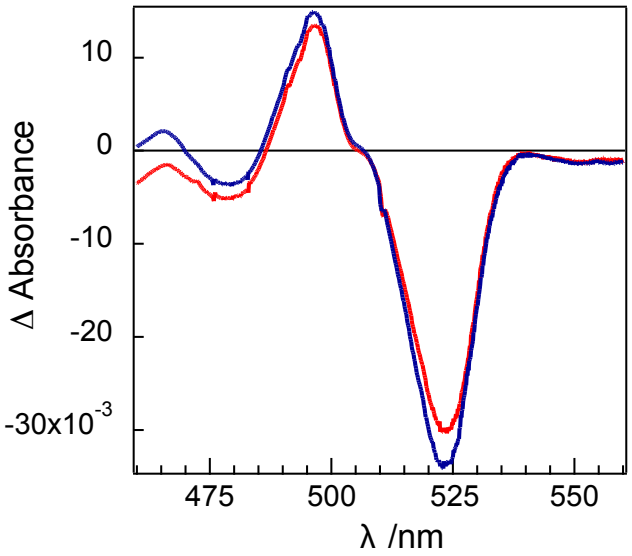

Figure 4.16 Transient difference spectra for unshaped excitation (red) and for pulse train excitation parameterized by α = 2.5 and τ = 225 fs (blue).

While the results described above are consistent with an increased population transfer out of the ground state with certain pulse trains (τ = 225 or 450 fs), the experiments are not sensitive to the nature of the initially formed excited state or its dynamics. Therefore, they are unable to address whether enhanced triplet yield is simply the natural result of a larger initial singlet exciton population (S_1), or whether the pulse trains are directly manipulating the product state distribution. To address this point an

experiment was designed to interrogate the relative yield of emissive singlet species (at 610 ± 5 nm; 20° off the front face of the film) during a transient absorption measurement of triplet yield at 490 nm.

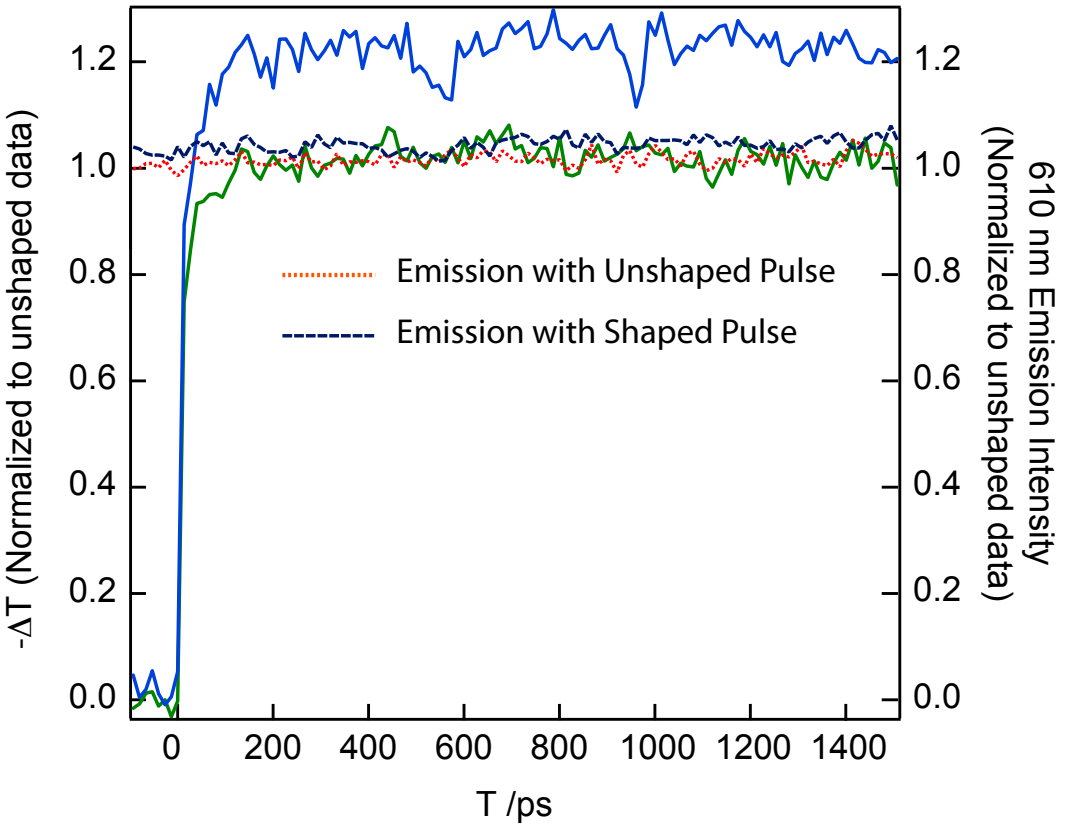

Figure 4.17 Solid lines show the kinetic traces of λ_{probe} = 490 nm for unshaped (green) and shaped (blue; α = 2.5, τ = 225 fs) pulse excitation monitored via transient absorption. Simultaneously measured were spontaneous emission traces from the film for the unshaped pulse (red, dotted) and pulse train (dark blue, dashed).

In **Figure 4.17** normalized transient absorption data (λ_{probe} = 490 nm; normalized at T = 1500 ps) is plotted along with normalized emission data (integrated signal at 610 ± 5 nm) collected during the two kinetics scans (T is irrelevant for the emission measurements). In the first kinetics scan (green solid line), an unshaped near transform limited pulse is sent to the sample leading to a transient absorption trace that is comparable to that shown in the inset of **Figure 4.9**. The spontaneous emission collected

during this scan is shown as the dotted red data. In the second kinetics scan (blue solid line) a shaped pulse is sent to the sample (again, α = 2.5, τ = 225 fs, and ϕ = 0) resulting in a ~ 20% increase of the 490 nm transient absorption signal compared to the unshaped field. This should then be compared to the results from the simultaneously collected emission data (dark blue dashed) where the yield of emission changes by only ~2% relative to the emission following excitation with an unshaped field.

These data suggest the shaped field does indeed affect branching ratios of the initial excited state population such that formation of the triplet is favored. Had increased product yield been achieved *only* by exciting more population from the ground state to the singlet exciton excited state (with branching ratios remaining the same), emission would have increased commensurate with that seen for the transient absorption data (i.e., by ~ 20%). An unresolved question is why the emission increases at all. A plausible explanation is delayed fluorescence due to triplet fusion (the inverse of singlet fission), which occurs when two diffusing triplets (that are presumably born during an earlier SF process) collide and reform a singlet exciton. In our experiment with no time resolution, fluorescence originating from such a process would simply be registered as an increase in yield. A time-resolved emission measurement coupled to an excitation source capable of producing shaped pulses would readily answer this remaining question.

4.5 Discussion and Conclusions

Given the data collected, it is possible to begin to hypothesize about the mechanisms of control by tying together observations of vibrational coherence (**Figure 4.10** and **Figure 4.15**) with the observation that certain pulse trains are successful at increasing triplet yield.

As argued regarding **Figure 4.10**, weak unshaped pulses of sufficient bandwidth are capable, not only of producing the singlet exciton, but also of resonantly exciting ground-state coherent motion of several different lattice and intramolecular vibrational modes that lasts for several picoseconds. The excitation fields produced by the phase-only shaping of Equation 4.1 consist of temporally spaced replicas of the unshaped pulse (see **Figure 4.12**). Each of these sub-pulses in the train is capable of producing singlet exciton population as well as vibrationally coherent ground-state population. As has been extensively demonstrated in the literature, such pulse trains have the ability to amplify resonant modes and filter those modes with a non-resonant period. [37, 42-44] Provided that subsequent pulses in the train are timed to match the period of the motion, vibrational coherence along a specific mode would build, as would the probability that a latter pulse could interact with a non-stationary ground state species, thereby accessing different Frank-Condon regions or different vibrational momentum (or both) to affect subsequent excited state potential energy surface trajectories. With this in mind, control by pulse trains with larger τ (τ = 225 fs, τ = 450 fs) is likely highlighting the importance of the low frequency intermolecular modes at facilitating the singlet fission photochemistry. In a similar vein, the lack of control by trains with shorter τ (107 fs) may indicate that this particular reaction coordinate is unimportant to the final product state.

Two possible control scenarios of this flavor must be tested in future theoretical and experimental work. The first is predicated on the idea that low frequency intermolecular motions between tetracene molecules in the lattice are expected to alter the electronic coupling that governs the rate of internal conversion between the ^{1}S state and the ^{1}(TT) along a high-frequency reaction coordinate. Presumably this high frequency coordinate

involves ring breathing that accompanies the formation of ^{1}(TT) – a state which would have significantly more π^* orbital character than the ^{1}S from which it forms. A properly-timed pulse train that interacts with non-stationary ground state species with momentum along an intermolecular coordinate or at a turning point when individual tetracene molecules are physically closest to each other, would produce ^{1}S species poised to react.

A second scenario considers that intermolecular motions may themselves be important SF reaction coordinates. Recent high level ab initio calculations by Zimmerman and Musgrave on SF in tetracene homodimers [13, 27] and 32-mers [31] have shown an energetically-activated crossing along an intermolecular coordinate between reactant (S_1 in character) and product (TT in character) potential energy curves. Pulse trains that are properly timed to the intermolecular motions might then produce the ^{1}S with more energy along this coordinate and with a nuclear geometry closer to that of the activated state.

In summary, we have shown the results of recent experimental work on tetracene thin films in which triplet state yield, a product of the singlet fission process, is enhanced when excited by specific pulse trains produced by Fourier-domain pulse shaping. There is evidence the enhancement is due in part to efficient coupling of the excitation field to low-frequency, intermolecular nuclear motions which affect the branching ratio of the initial excited state population. Possible mechanisms are discussed that may be responsible for the observed behavior especially in light of recent theoretical work that shows intermolecular motions may play an important role in the singlet fission process in polyacenes. This work is an example of how pulse shaping can serve to reveal novel photophysics through adaptive optimization techniques as well as be employed as a highly capable spectroscopic tool to interrogate relevant relaxation dynamics of complex systems.

4.6 References Cited

1. W. Shockley and H. J. Queisser, "Detailed Balance Limit of Efficiency of p-n Junction Solar Cells," Journal Of Applied Physics **32**, 510-519 (1961).

2. J. Tauc, "Electron impact ionization in semiconductors," Journal of Physics and Chemistry of Solids (1959).

3. C. Swenberg and W. Stacy, "Bimolecular radiationless transitions in crystalline tetracene," Chem. Phys. Lett. **2**, 327-328 (1968).

4. M. Pope and C. E. Swenberg, *Electronic Processes in Organic Crystals and Polymers,* 2nd ed. (Oxford University Press, New York, 1999).

5. A. J. Nozik, M. C. Beard, J. M. Luther, M. Law, R. J. Ellingson, and J. C. Johnson, "Semiconductor Quantum Dots and Quantum Dot Arrays and Applications of Multiple Exciton Generation to Third-Generation Photovoltaic Solar Cells," Chemical Reviews **110**, 6873-6890 (2010).

6. I. Paci, J. Johnson, X. Chen, G. Rana, D. Popovic, D. David, A. Nozik, M. Ratner, and J. Michl, "Singlet fission for dye-sensitized solar cells: Can a suitable sensitizer be found?," Journal Of The American Chemical Society **128**, 16546-16553 (2006).

7. M. B. Smith and J. Michl, "Singlet Fission," Chemical Reviews **110**, 6891-6936 (2010).

8. M. C. Hanna and A. J. Nozik, "Solar conversion efficiency of photovoltaic and photoelectrolysis cells with carrier multiplication absorbers," Journal Of Applied Physics **100**, 074510 (2006).

9. R. C. Johnson and R. E. Merrifield, "Effects of Magnetic Fields on the Mutual Annihilation of Triplet Excitons in Anthracene Crystals," Physical Review B **1**, 896-902 (1970).

10. S. H. Lim, T. G. Bjorklund, F. C. Spano, and C. J. Bardeen, "Exciton delocalization and superradiance in tetracene thin films and nanoaggregates," Physical Review Letters **92**(2004).

11. V. K. Thorsmolle, R. D. Averitt, J. Demsar, D. L. Smith, S. Tretiak, R. L. Martin, X. Chi, B. K. Crone, A. P. Ramirez, and A. J. Taylor, "Morphology Effectively Controls Singlet-Triplet Exciton Relaxation and Charge Transport in Organic Semiconductors," Physical Review Letters **102**(2009).

12. T. S. Kuhlman, J. Kongsted, K. V. Mikkelsen, K. B. Moller, and T. I. Solling, "Interpretation of the Ultrafast Photoinduced Processes in Pentacene Thin Films," Journal Of The American Chemical Society **132**, 3431-3439 (2010).

13. P. M. Zimmerman, Z. Zhang, and C. B. Musgrave, "Singlet fission in pentacene through multi-exciton quantum states," Nature Chemistry **2**, 648-652 (2010).

14. E. M. Grumstrup, J. C. Johnson, and N. H. Damrauer, "Enhanced triplet formation in polycrystalline tetracene films by femtosecond optical-pulse shaping," Physical Review Letters **105**, 257403- (2010).

15. W. Hofberger, "Structure and Optical-Properties of Polycrystalline Evaporated Tetracene Films," Phys Status Solidi A **30**, 271-278 (1975).

16. T. Kobayashi and A. Shirakawa, "Sub-10-fs tunable pulses in visible and NIR and visible sub-5-fs pulses generated by noncollinear OPA," Journal of Luminescence **87**, 119-120 (2000).

17. J. Piel, M. Beutter, and E. Riedle, "20-50-fs pulses tunable across the near infrared from a blue-pumped noncollinear parametric amplifier," Optics Letters **25**, 180-182 (2000).

18. A. Prakelt, M. Wollenhaupt, A. Assion, C. Horn, C. Sarpe-Tudoran, M. Winter, and T. Baumert, "Compact, robust, and flexible setup for femtosecond pulse shaping," Review of Scientific Instruments **74**, 4950-4953 (2003).

19. T. Feurer and A. Glass, "Two-photon photoconductivity in SiC photodiodes and its application to autocorrelation measurements of femtosecond optical pulses," Applied Physics B-Lasers And Optics (1997).

20. R. Judson and H. Rabitz, "Teaching lasers to control molecules," Physical Review Letters **68**, 1500-1503 (1992).

21. M. A. Montgomery, R. R. Meglen, and N. H. Damrauer, "General Method for the Dimension Reduction of Adaptive Control Experiments," The Journal of Physical Chemistry A **110**, 6391-6394 (2006).

22. A. S. Davydov, *Theory of Molecular Excitons* (McGraw-Hill, New York, 1962).

23. M. Voigt, A. Langner, P. Schouwink, J. M. Lupton, R. F. Mahrt, and M. Sokolowski, "Picosecond time resolved photoluminescence spectroscopy of a tetracene film on highly oriented pyrolytic graphite: Dynamical relaxation, trap emission, and superradiance," Journal Of Chemical Physics **127**(2007).

24. Y. H. Meyer, R. Astier, and J. M. Leclercq, "Triplet-Triplet Spectroscopy of Polyacenes," Journal Of Chemical Physics **56**, 801-& (1972).

25. J. R. Weinberg-Wolf, L. E. McNeil, S. Liu, and C. Kloc, "Evidence of low intermolecular coupling in rubrene single crystals by Raman scattering," Journal Of Physics-Condensed Matter **19**, 276204 (2007).

26. R. Lehnig and A. Slenczka, "Spectroscopic investigation of the solvation of organic molecules in superfluid helium droplets," Journal Of Chemical Physics **122**(2005).

27. P. M. Zimmerman and C. B. Musgrave, (personal communication, 2010).

28. Y. Tomkiewicz, R. P. Groff, and P. Avakian, "Spectroscopic Approach to Energetics of Exciton Fission and Fusion in Tetracene Crystals," Journal Of Chemical Physics **54**, 4504-& (1971).

29. R. Jankowiak, J. Kalinowski, M. Konys, and J. Buchert, "Solid-State Transitions in Crystalline Tetracene," Chem. Phys. Lett. **65**, 549-553 (1979).

30. E. Venuti, R. G. Della Valle, L. Farina, A. Brillante, M. Masino, and A. Girlando, "Phonons and structures of tetracene polymorphs at low temperature and high pressure," Physical Review B **70**(2004).

31. P. M. Zimmerman, (personal communication, 2011).

32. C. Bardeen, V. Yakovlev, J. Squier, and K. Wilson, "Quantum control of population transfer in green fluorescent protein by using chirped femtosecond pulses," Journal Of The American Chemical Society **120**, 13023-13027 (1998).

33. J. Cao, C. Bardeen, and K. Wilson, "Molecular pi pulses: Population inversion with positively chirped short pulses," Journal Of Chemical Physics **113**, 1898-1909 (2000).

34. J. Herek, W. Wohlleben, R. Cogdell, D. Zeidler, and M. Motzkus, "Quantum control of energy flow in light harvesting," Nature **417**, 533-535 (2002).

35. D. Cardoza, F. Langhojer, and C. Trallero-Herrero, "Changing pulse-shape basis for molecular learning control," Physical Review A (2004).

36. A. Bartelt, T. Feurer, and L. Woste, "Understanding optimal control results by reducing the complexity," Chemical Physics **318**, 207-216 (2005).

37. T. Buckup, J. Hauer, C. Serrat, and M. Motzkus, "Control of excited-state population and vibrational coherence with shaped-resonant and near-resonant excitation," Journal Of Physics B-Atomic Molecular And Optical Physics **41**, 074024 (2008).

38. A. Weiner, "Femtosecond pulse shaping using spatial light modulators," Review of Scientific Instruments **71**, 1929-1960 (2000).

39. J. Vaughan, T. Feurer, K. Stone, and K. Nelson, "Analysis of replica pulses in femtosecond pulse shaping with pixelated devices," Optics Express **14**, 1314-1328 (2006).

40. J. Hauer, H. Skenderovic, K. Kompa, and M. Motzkus, "Enhancement of Raman modes by coherent control in beta-carotene," Chem. Phys. Lett. **421**, 523-528 (2006).

41. J. Hauer, T. Buckup, and M. Motzkus, "Enhancement of molecular modes by electronically resonant multipulse excitation: Further progress towards mode selective chemistry," Journal Of Chemical Physics **125**, 061101 (2006).

42. A. Weiner, D. Leaird, G. Wiederrecht, and K. Nelson, "Femtosecond Pulse Sequences Used for Optical Manipulation of Molecular Motion," Science **247**, 1317 (1990).

43. H. Kawashima, M. Wefers, and K. Nelson, "Femtosecond Pulse Shaping, Multiple-Pulse Spectroscopy, and Optical Control," Ann. Rev. Phys. Chem. **46**, 627-656 (1995).

44. J. Hauer, T. Buckup, and M. Motzkus, "Quantum control spectroscopy of vibrational modes: Comparison of control scenarios for ground and excited states in beta-carotene," Chemical Physics **350**, 220-229 (2008).

CHAPTER 5

A TIME DEPENDENT PERSPECTIVE OF SINUSOIDAL SPECTRAL PHASE MODULATION

5.1 Introduction

Coherent control has recently matured from a field that primarily focused on the demonstration of novel light matter interactions to an incisive spectroscopic tool for the elucidation of complex photophysics. This is especially apparent in examples in which coherent control has revealed the importance of molecular vibrations to photochemical reactivity. [1-6] One driving contribution that has led to this development has been the use of simple, intuitive functions for the parameterization of the excitation field, which, in the time domain, can often be well described as periodically spaced subpulse replicas of the transform-limited pulse with a spacing readily correlated to known molecular vibrations. [3,7-9] The success of these simple, periodic fields for controlling photochemical reactions is understood as an increased reactivity due to an enhancement of specific vibrational modes along some reaction coordinate.

The predominant method for creating pulse trains in the time domain is a sinusoidal modulation of the spectral phase. The application of these functions only affects the phase of the spectral field and consequently conserves the total energy in a given pulse— an

appealing attribute in coherent control experiments for the practical reasons of eliminating artifacts. The use of these functions was initially restricted to multiphoton absorption and stimulated Raman processes. [10-15] Herek's and Motzkus' use of sinusoidal phase functions in the control of light harvesting proteins was an early success of this class of pulse shaping at controlling time domain phenomena. [3] Since then, there have been numerous examples of successful coherent control employing the simple and intuitively interpreted pulse trains created by these functions.

This intuitive interpretation of the light matter interaction nevertheless leaves important questions unanswered. The literature abounds with qualitative descriptions of excitation fields being particularly well suited to favorably interact with matter waves, but there are few examples of formal descriptions of these phenomena. [3,4,6,7,16,17] Even in simple model systems, enhancement of population transfer to the excited state is not fully understood when pulse trains are used for excitation rather than transform limited pulses. [18,19]

This work seeks to begin to address the lack of transparency in coherent control mechanisms by linking the successful control paradigm of periodic pulse trains with the formalism and predictive abilities of time dependent perturbation theory. We do this by simulating the interaction of pulse trains generated by sinusoidal spectral phase modulation with a simple model of a two level atom using a non-perturbative density matrix, which includes all orders of the light matter interaction. We then separate individual pathways described by perturbation theory from the total signal by a phase cycling scheme and discuss their contribution to the overall population as well as the spectroscopic information they reveal. Finally, we discuss the generalization of this

methodology to more complex systems – especially as a means to test hypotheses of control mechanisms when the suspected mechanism employs phase sensitive excitation pathways –a hallmark of nontrivial coherent control.

5.2 Sinusoidal Spectral Phase Modulation

Sinusoidal spectral phase modulation is achieved by applying a spectral phase, $P(\omega;\alpha,\tau,\phi) = \alpha\cos(\omega\tau+\phi)$, to a broadband laser pulse, $\tilde{\epsilon}_{in}(\omega)$, where α is the amplitude of the applied phase function, ω determines the period of the function, and τ and ϕ determine the number and position of oscillations within the spectral envelope, respectively. The shaped spectral domain laser pulse, $\tilde{\epsilon}_{out}(\omega)$, is modified according to

$$\tilde{\epsilon}_{out}(\omega) = \tilde{\epsilon}_{in}(\omega)e^{i\alpha\cos(\omega\tau+\phi)}. \qquad [5.1]$$

The Fourier Transform pair is

$$\tilde{\epsilon}(\omega)e^{i\alpha\cos(\omega\tau+\phi)} \Leftrightarrow \sum_{m=-\infty}^{\infty} J_m(\alpha)\tilde{E}(t-m\tau)e^{im\left(\phi+\frac{\pi}{2}\right)} + c.c. \qquad [5.2]$$

where $\tilde{E}(t) = A(t)e^{i\left(-\omega_p t+\varphi(t)\right)}$ is the complex temporal amplitude with carrier frequency ω_p comprised of the unshaped temporal envelope $A(t)$ centered at t = 0 and temporal phase $\varphi(t)$. The $J_m(\alpha)$ are the mth Bessel Functions of the first kind. The $\frac{\pi}{2}$ phase shift is a consequence of the Jacobi Anger identity employed in the expansion of the sinusoidal exponential. In general, a sinusoidal spectral phase modulation creates a pulse train in the time domain formally composed of an infinite number of subpulse replicas of the transform limited pulse, though of lower amplitude. [20] This pulse train is centered on the subpulse corresponding to the m = 0 term in the expansion of Equation 5.2, temporally located at the

same position as the unshaped pulse. In practice, however, the envelope is composed of a finite number of subpulses with non-negligible amplitude, the sum of which contains the same integrated area as the transform limited case. In this work, ω will be given by the optical frequency of the electric field, ω_p, however, rotating frame measurements can easily be used to reduce the number of sampling points necessary in acquiring signal traces. [21,22] Figures 5.1-5.3 show frequency and time domain illustrations of the three parameters, α, τ, and ϕ, respectively.

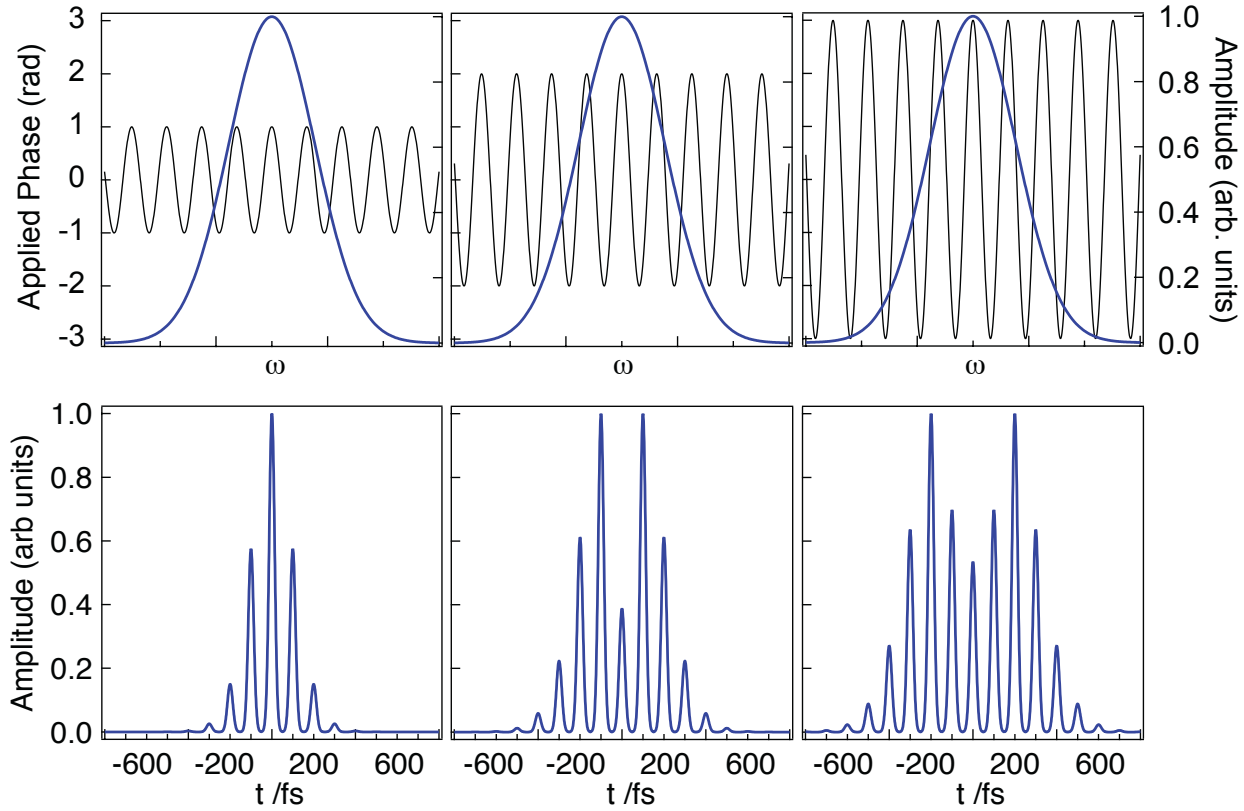

Figure 5.1 *Top:* Spectral amplitude (blue thick line) and applied phase (black thin line) with α = 1 (left), 2 (middle), and 3 (right) in Equation 5.1. *Bottom:* Temporal amplitude for α = 1 (l), 2 (m), and 3 (r) in Equation 5.1. Note the amplitude of the pulse train has been normalized for each individual plot – All pulse trains have the same integrated energy.

The parameter α serves to map the sinusoidal spectral function onto the applied phase of the field as shown in Figure 5.1. In the time domain, an increase in magnitude α roughly

corresponds to a pulse train composed of a greater number of pulse replicas. In addition the relative magnitudes of each one of these individual subpulses is modified according to the evaluation of the Bessel Functions of the first kind at α.

As an example, the pulses given by the m = -1 and m = +1 terms in Equation 5.2 are those immediately preceding and following the center pulse of the train, respectively. For the case of $\alpha = 1.0$, the magnitude of each of these subpulses is given by $J_{-1}(1.0)$ and $J_{+1}(1.0)$, which, if we account for any changes in sign by adding a temporal phase of π to the carrier frequency of the pulse, corresponds to $\sim .58$ of the m = 0 pulse (see Figure 5.1, left). The notation of referring to individual subpulses by the index, m, will be used throughout this manuscript.

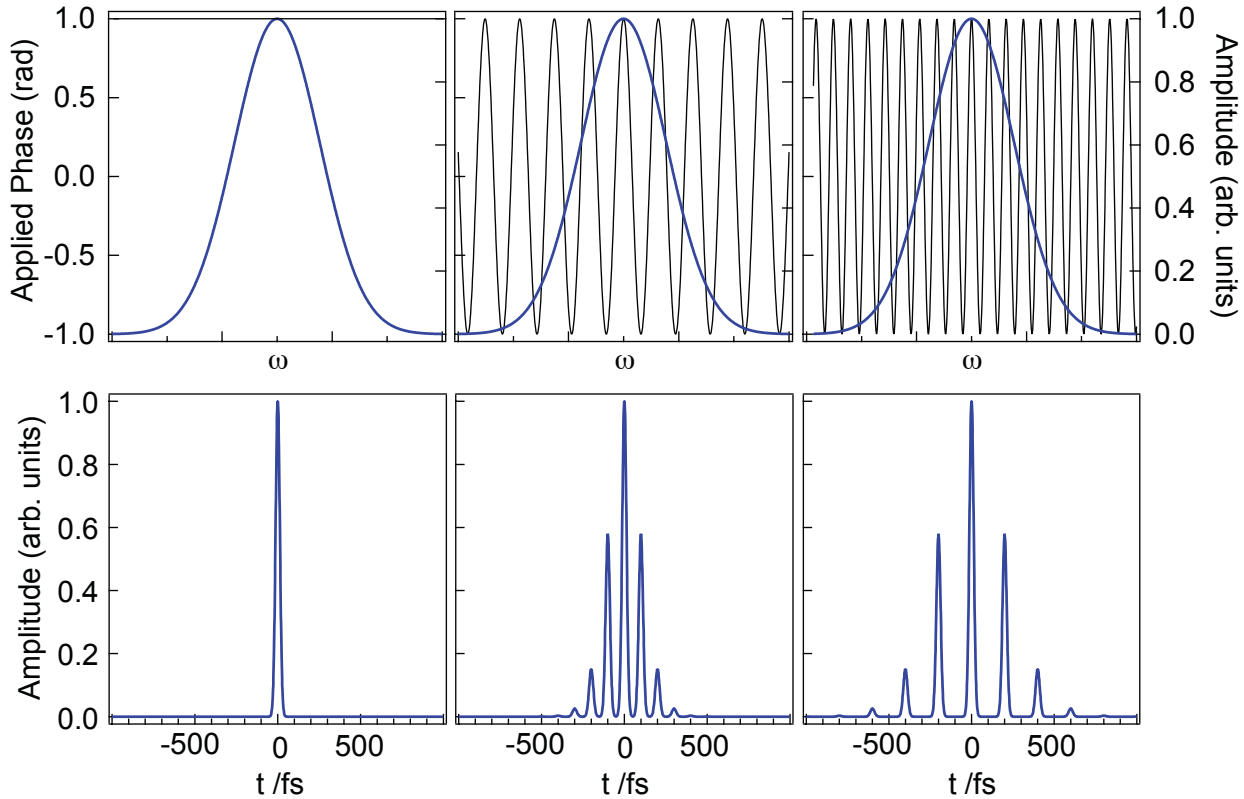

Figure 5.2 *Top:* Spectral amplitude (blue thick line) and applied phase (black thin line) for α =1 and τ = 0 fs (l), 100 fs (m), and 200 fs (r) in Equation 5.1. *Bottom:* Temporal amplitude α =1 and τ = 0 fs (l), 100 fs (m), and 200 fs (r) in Equation 5.1.

Figure 5.2 shows the spectral amplitude and phase for τ = 0 fs (l), τ = 100 fs (m), and τ = 200 fs (r), as well as the corresponding time domain pulse train. In the left column is the applied phase and resultant pulse train for τ = 0 fs which is just an unshaped, transform limited pulse. This limiting case can also be obtained by setting $\alpha = 0$ in Equation 5.1. Note that when the optical frequency is used to set the period of the sinusoidal function, $\frac{2\pi}{\omega}$, as is the case in this work, τ corresponds to the temporal separation between each of the subpulses in the train. Therefore, in Figure 5.2, the pulse trains created by setting τ = 100 fs (m) and τ = 200 fs (r) have subpulses separated by 100 fs and 200 fs, respectively.

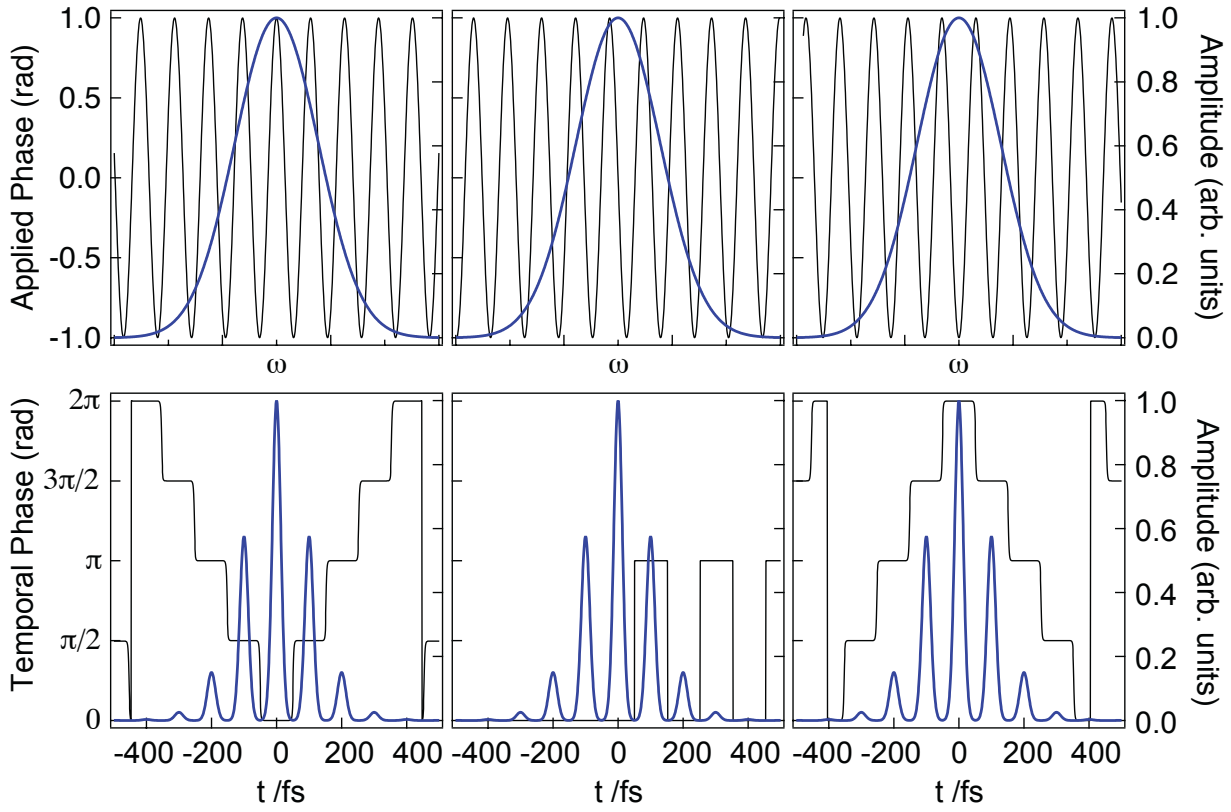

Figure 5.3 *Top:* Spectral amplitude (blue thick line) and applied phase (black thin line) with ϕ = 0 (left), $\frac{\pi}{2}$ (middle), and π (right) in Equation 5.1. *Bottom:* Temporal amplitude and phase for ϕ = 0 (l), $\frac{\pi}{2}$ (m), and π (r) in Equation 5.1.

The final parameter in Equation 5.2, ϕ, determines the relative phase of the individual subpulses in the train. Figure 5.3 illustrates the spectral and temporal effects of

setting $\phi = 0$ (l), $\phi = \frac{\pi}{2}$ (m), and $\phi = \pi$ (r). In this work ϕ will only take the values of $0, \frac{\pi}{2}, \pi$, and $\frac{3\pi}{2}$. As can be seen moving across the top row, the relative position of the cosine function moves with the offset ϕ.

5.3 Density Matrix Model

We examine the interaction of laser pulses shaped by sinusoidal phase modulation and a molecular system by employing density matrix theory to describe a two level model complete with phenomenological relaxation parameters and explicit transition dipole electric field interaction. A two level system serves as a reasonable starting point for the modeling of these interactions as it is a well-characterized system and can readily be described by perturbative expansion in orders of the light matter interaction. [23]

The Hamiltonian of the system is given by Equation 5.3 which is composed of the field free Hamiltonian, $\hat{H}_0$, and the light matter interaction operator $\hat{V}$. Here, $\boldsymbol{E}(t)$ is the real time dependent electric field and μ is the transition dipole moment (set to 1 in this work). E_{00} and E_{11} are the ground and excited state energies of the system.

$$\hat{H}(t) = \hat{H}_0 + \hat{V}(t) = \begin{bmatrix} E_{00} & 0 \\ 0 & E_{11} \end{bmatrix} + \begin{bmatrix} 0 & -\mu \cdot \boldsymbol{E}(t) \\ -\mu \cdot \boldsymbol{E}(t) & 0 \end{bmatrix} \quad [5.3]$$

We evolve the density matrix of the system in time under the Liouville-Von Neumann equation,

$$\frac{\partial}{\partial t}\rho(t) = -\frac{i}{\hbar}\left[\hat{H}(t), \rho(t)\right] \quad [5.4]$$

subject to the rotating frame and the slowly varying envelope approximations. [23-25] ρ_{11} and ρ_{00} represent the excited and ground state populations, respectively. ρ_{10} is a

measure of the coherent superposition of the ground and excited states. Equations 5.5 – 5.8 give the equations of motion for the density operator.

$$\dot{\rho}_{00} = -\frac{i}{\hbar}[\mu\tilde{E}^*(t)\rho_{01} - \rho_{10}\mu\tilde{E}(t)] - \Gamma_{01}\rho_{11} \quad [5.5]$$

$$\dot{\rho}_{10} = \frac{i}{\hbar}[\mu\tilde{E}^*(t)(\rho_{11} - \rho_{00}) - (E_{11} - E_{00})\rho_{10}] - \gamma_{10}\rho_{10} \quad [5.6]$$

$$\dot{\rho}_{11} = -\dot{\rho}_{00} \quad [5.7]$$

$$\rho_{01} = \rho_{10}^* \quad [5.8]$$

Here $\tilde{E}(t)$ is the complex electric field, which can be arbitrarily shaped by construction of the spectral phase and amplitude followed by numerical Fourier Transform (note the functional form of the pulse train made explicit in Equation 5.2 has been suppressed). The population relaxation term, Γ_{01}, determines the rate of population relaxation from the excited state to the ground state, γ_{10}^{pure} quantifies dephasing mechanisms not associated with population relaxation (such as elastic collisions), and $\gamma_{10} = \frac{1}{2}\Gamma_{01} + \gamma_{10}^{pure}$. [23,25] The exact numerical values of these parameters will determine some characteristics of the results examined below and shall be discussed in further detail. Propagation of the full non-perturbative density matrix was performed with a fourth order Runge-Kutta algorithm and checked for convergence by reducing the step size for representative calculations. [26]

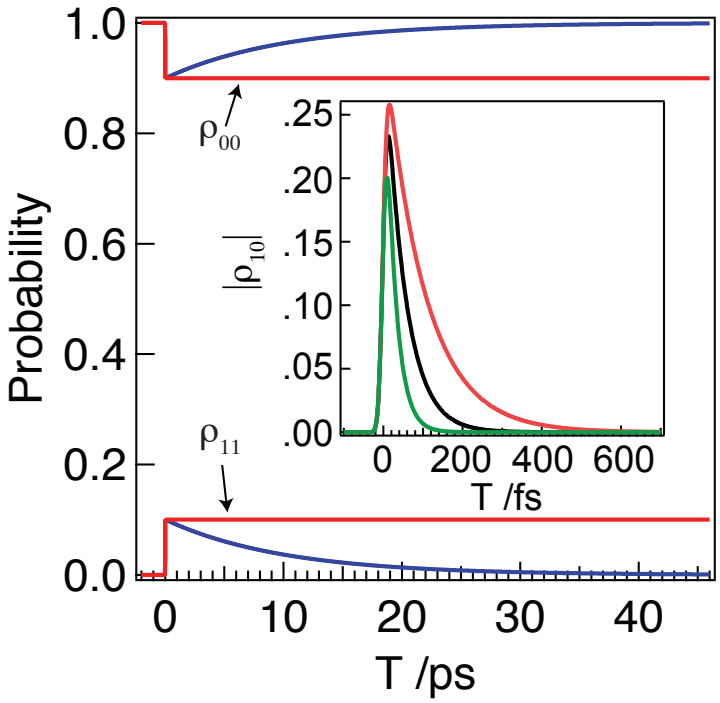

Figure 5.4 Population dynamics of the ground and excited states for population relaxation rates (see Equations 5.5 – 5.8), Γ_{01}= 0 ps^{-1} (red) and Γ_{01}= .1 ps^{-1} (blue). *Inset:* Modulus of the electronic coherence, $|\rho_{10}|$, for γ_{10}^{pure}=.04 fs^{-1} (green), .02 fs^{-1} (black), and .01 fs^{-1} (red).

Figure 5.4 shows typical output of the density matrix model with an illustration of the dependency on the various relaxation parameters. The main plot shows ground state population, ρ_{00}, and excited state population, ρ_{11} as a function of time with respect to the excitation pulse at T = 0 ps. The populations are shown for the cases of population relaxation rate Γ_{01}= 0 ps^{-1} (red) and Γ_{01}= .1 ps^{-1} (blue). Initial excitation level is 10% in both cases. In the inset, the modulus of the electronic coherence, $|\rho_{10}|$ is plotted for three realizations of the electronic dephasing time γ_{10}^{pure}. Green, black, and red traces correspond to γ_{10}^{pure}= .04 fs^{-1}, .02 fs^{-1}, and .01 fs^{-1}, respectively, showing how the electronic coherence quickly damps with respect to the time scale of population dynamics.

5.4 Results and Discussion

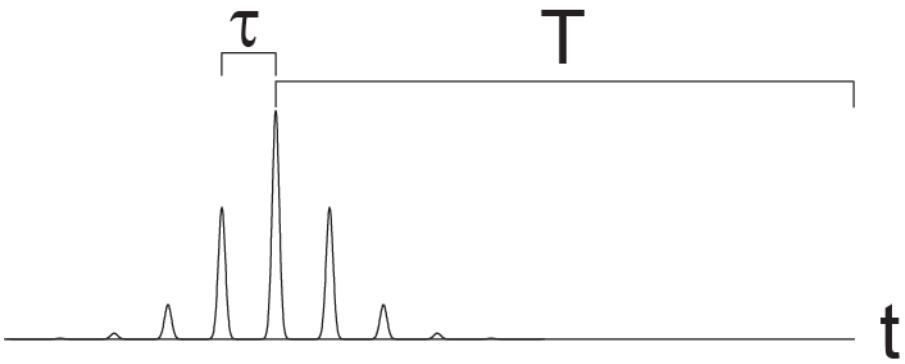

Figure 5.5 Schematic defining various time intervals used throughout. The interval τ separates all subpulses within the pulse train. T defines the delay between excitation and when the population is probed.

In an effort to isolate the portion of the population that is created by interpulse interactions, the population is monitored at a time well after the interaction with the excitation pulse train near T = 0 ps. Figure 5.5 shows a simple schematic of the measurement with the various time interval definitions used throughout this manuscript. Note that T is only well defined with respect to the center of the pulse train, but not for each individual subpulse. The population at T is collected as τ is scanned from $\tau = 0$ to $\tau = \tau^{final}$ ($\tau^{final} > \frac{4}{\gamma_{10}}$), producing a signal trace, $S(T, \tau; \alpha, \phi)$, reflecting the portion of the population dependent on coherent, multi-pulse interactions. Figure 5.6 shows such a trace as τ is scanned from 0 fs to 250 fs ($\alpha = 2.25, \phi = 0$) for the two level system with Γ_{01}= 0 ps^{-1} and γ_{10}^{pure}= .02 fs^{-1}. Note that because Γ_{01}= 0 ps^{-1}, T is irrelevant as long as the population is probed after the pulse train has interacted with the system. The decay is normalized to the excited state population at τ = 0 fs where 10 % of the ground state system has been transferred to the excited state.

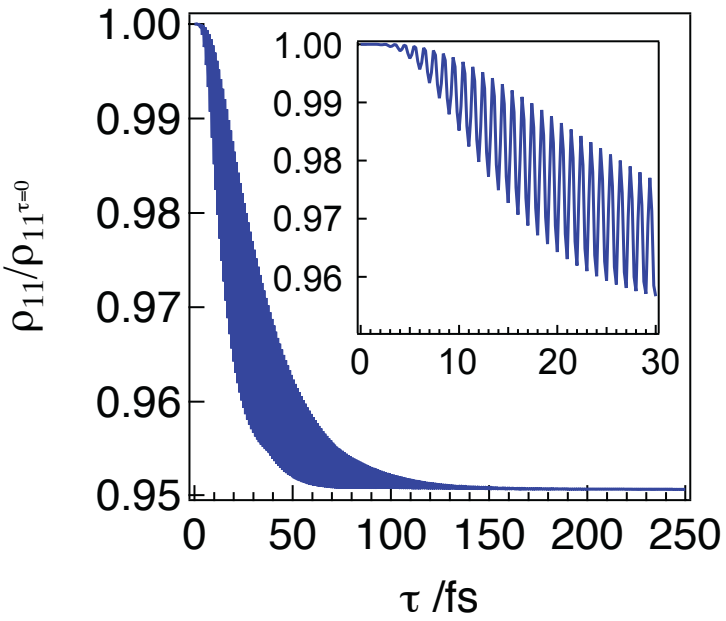

Figure 5.6 Signal trace, $S(T,\tau;\alpha,\phi)$, showing population sensitivity to pulse train excitation. τ is scanned from 0 fs to 250 fs in this case. *Inset:* Magnified portion of the decaying signal showing oscillatory population dynamics with τ.

There are three main components to the signal trace. The first and most dominant is the portion of the population arising from excitation by each individual subpulse. This component comprises (at 10% excitation) ~95% of the population as can be noted at the long τ limit in Figure 5.6. The second component is responsible for the 5% decay of the signal from the transform-limited excitation ($\tau = 0$) to the asymptotic limit reached by ~ 150 fs. Finally, there exists an oscillatory component that decays on the same time scale as the overall decay of the signal trace. The final two contributions to the population decay on a similar time scale as the electronic dephasing parameter $1/\gamma_{10}^{pure}$; it is therefore reasonable to suspect the pathways that lead to these components of the population depend on interactions between unique subpulses in the pulse train. In an effort to determine what specific pathways lead to each contribution and allow a formal description of these processes, time dependent perturbation theory will be used to reproduce the

recovered signal traces obtained from the non-perturbative density matrix described above.

In the perturbative expansion of the density matrix, a population is created only through processes that have an even number of light matter interactions. By way of analogy to standard practice in the coherent control community whereby pulse shaping is employed to affect changes in population, this work only focuses on the induced population changes due to this class of pulse shapes – it is therefore only necessary to consider interactions with the field that are 2nd and 4th order[1].

$$\rho^{(2)}(t) = \left(-\frac{i}{\hbar}\right)^2 \int_{-\infty}^{t} dt' \int_{-\infty}^{t'} dt'' \, \boldsymbol{E}(t')\boldsymbol{E}(t'')U_0(t,t_0)\big[\mu(t'),[\mu(t''),\rho^0]\big]U_0^\dagger(t,t_0) \qquad [5.9]$$

Equation 5.9 is the 2nd order correction to the equilibrium density operator, ρ^0. Here $U_0^\dagger(t,t_0) = e^{-iH_0(t-t_0)}$ is the field free evolution operator and $\mu(t) = U_0^\dagger(t,t_0)\mu_{10}U_0(t,t_0)$. The expansion of the density operator at fourth order (Equation 5.10) is of a similar form:

$$\rho^{(4)}(t) = \left(-\frac{i}{\hbar}\right)^4 \int_{-\infty}^{t} dt' \int_{-\infty}^{t'} dt'' \int_{-\infty}^{t''} dt''' \int_{-\infty}^{t'''} dt'''' \, \boldsymbol{E}(t')\boldsymbol{E}(t'')\boldsymbol{E}(t''')\boldsymbol{E}(t'''')\times U_0(t,t_0)\Big[\mu(t'),\Big[\mu(t''),\big[\mu(t'''),[\mu(t''''),\rho^0]\big]\Big]\Big]U_0^\dagger(t,t_0). \qquad [5.10]$$

Within the rotating wave approximation there are only two pathways (and their complex conjugates) that create population at 2nd order and eight pathways that create population at 4th order. [24] Figure 5.7 shows the double-sided Feynman diagrams corresponding to each of these contributions. In these diagrams, time moves forward from bottom to top, arrows symbolize interactions with the field, and the indices denote the

[1] In principle, 6th order interactions and higher must also be considered, however at the excitation conditions considered here, these higher order pathways have negligibly small contributions to the overall population.

state of the density matrix during the interval between interactions. If the final population arises from interactions of at least two *unique* pulses in the pulse train, it will accumulate a phase factor from the interaction with the electric field consistent with the pathway of population formation. [27-31]

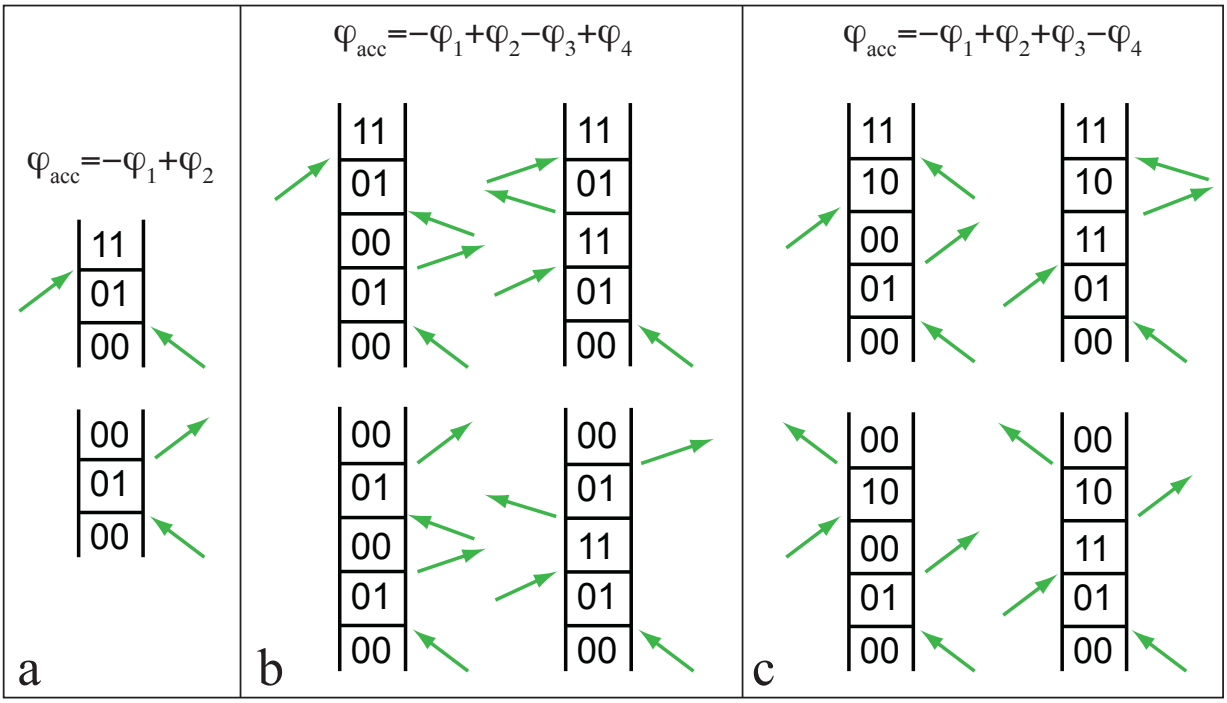

Figure 5.7 Double sided Feynman diagrams corresponding to the 2nd (**a**) and 4th order (**b** and **c**) interactions leading to ground or excited state population. Arrows represent interactions with the field and the indices show the status of the density matrix during the time interval between interactions. Heading the columns are expressions for the accumulated phase, φ_T, from the two (2nd order) or four (4th order) interactions with the electric field.

The expressions for this accumulated phase, φ_{acc}, head the columns of the diagrams for the 2nd order and 4th order pathways that are responsible for population formation in this model system. As an illustration, consider the 2nd order diagrams in which the first interaction symbolized by the arrow pointing to the left adds a phase of $-\varphi_1$ and the second interaction with the arrow pointing to the right adds a phase of $+\varphi_2$. These phase factors affect the magnitude of the integrals, Equations 5.5 and 5.6, for a given time interval between interactions with the field, and they will allow the separation of the various

pathways described by the Feynman diagrams below to be extracted from the overall non-perturbative density matrix propagation.

The accumulated phase factor, φ_{acc}, can be exploited in a manner analogous to k vectors in the noncollinear geometries typically used to separate individual pathways in two-dimensional optical spectroscopy. [24,32] By changing the ϕ parameter in Equation 5.1, the relative phase of each of the subpulses within the excitation pulse train is modified (see Figure 5.3). This affects the phase that each pathway accumulates in a predictable manner, and so, by collecting signal traces like Figure 5.6 for different values of ϕ, it is possible to isolate contributing pathways to the overall population by phase cycling. Table 5-I shows the temporal phase for the mth subpulse produced by Equation 5.2 for four different values of ϕ: $0, \frac{\pi}{2}, \pi$, and $\frac{3\pi}{2}$. Note that in this case where $\phi = l\frac{\pi}{2}$ (l = 0, 1, 2, or 3), the higher order terms in the expansion (m = ±4, ±5, etc.) have the same temporal phase as lower order terms since the relative phase from one pulse to the next goes as modulo 4 with the index of the expansion (see Equation 5.2).

Table 5-I Relative temporal phase associated with the mth subpulse for $\phi = 0, \pi/2, \pi$, and $3\pi/2$ in Equation 5.1.

	m = -3	m = -2	m = -1	m = 0	m = 1	m = 2	m = 3
$\phi = 0$	$-\pi/2$	π	$\pi/2$	0	$\pi/2$	π	$-\pi/2$
$\phi = \pi/2$	0	0	0	0	π	0	π
$\phi = \pi$	$\pi/2$	π	$-\pi/2$	0	$-\pi/2$	π	$\pi/2$
$\phi = 3\pi/2$	π	0	π	0	0	0	0

Four linear combinations of the four signal traces $S\left(T,\tau;\alpha,\phi=l\frac{\pi}{2}\right)$ taken from the non-perturbative density matrix propagation can be made (T,τ,α dependence is suppressed).

$$\mathbb{S}_{++++}=S(\phi=0)+S\left(\phi=\frac{\pi}{2}\right)+S(\phi=\pi)+S\left(\phi=\frac{3\pi}{2}\right) \quad [5.11]$$

$$\mathbb{S}_{+-+-}=S(\phi=0)-S\left(\phi=\frac{\pi}{2}\right)+S(\phi=\pi)-S\left(\phi=\frac{3\pi}{2}\right) \quad [5.12]$$

$$\mathbb{S}_{+--+}=S(\phi=0)-S\left(\phi=\frac{\pi}{2}\right)-S(\phi=\pi)+S\left(\phi=\frac{3\pi}{2}\right) \quad [5.13]$$

$$\mathbb{S}_{++--}=S(\phi=0)+S\left(\phi=\frac{\pi}{2}\right)-S(\phi=\pi)-S\left(\phi=\frac{3\pi}{2}\right) \quad [5.14]$$

Shown in Figure 5.8a-5.8d are the linear combinations associated with Equations 5.11-5.14. In all cases, the signal has been normalized with respect to the excited state population at τ = 0 fs (10 % of the ground state system has been transferred to the excited state), and $\alpha = 2.25$. Again, as in Figure 5.6, there is no population relaxation, Γ_{01}= 0 ps^{-1} and the electronic dephasing rate γ_{10}^{pure}= .02 fs^{-1}.

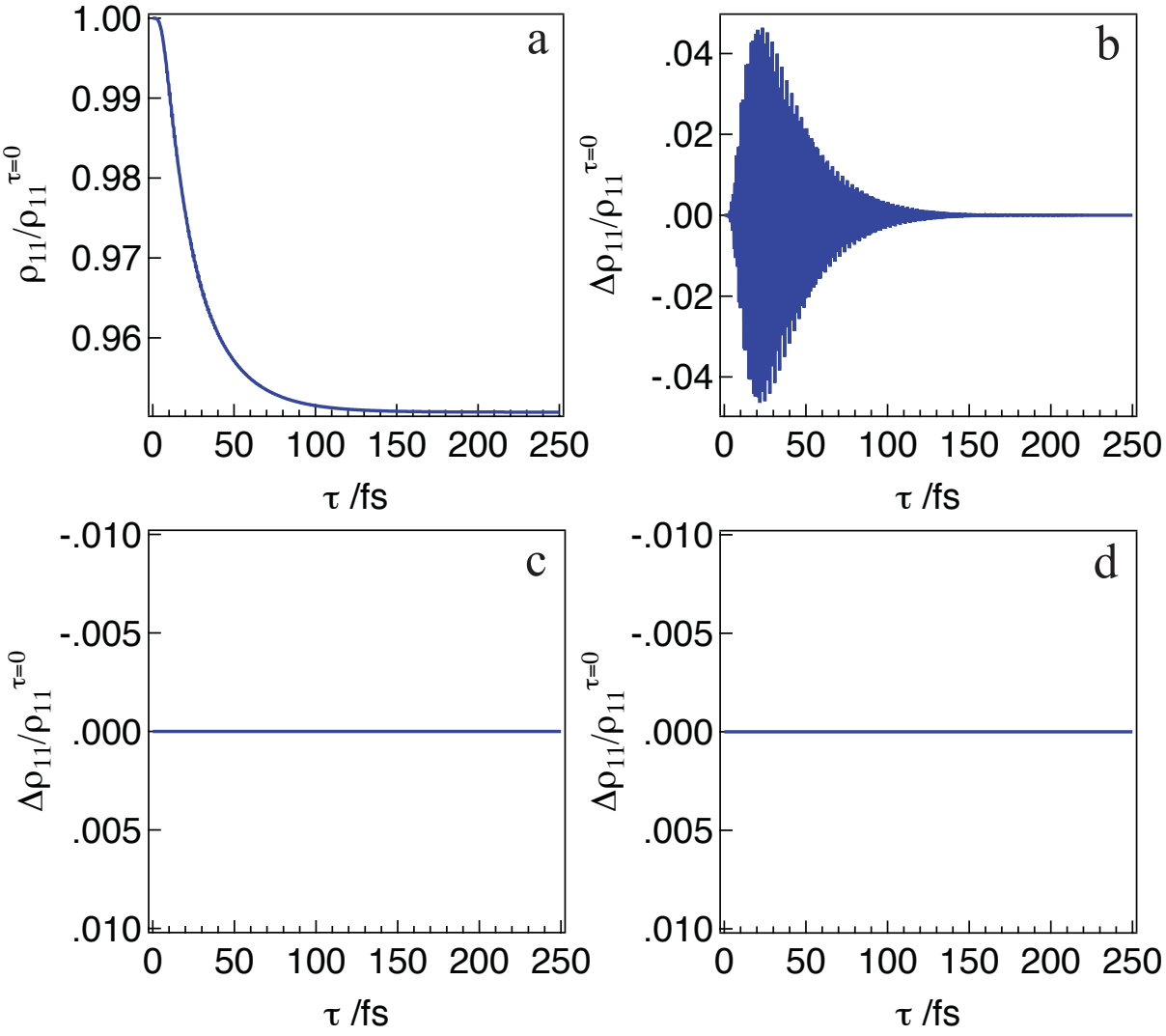

Figure 5.8 *a:* $\mathbb{S}_{++++}$ calculated according to Equation 5.8 from the numerical propagation of the density matrix ρ. Shown in panels *b*, *c*, and *d* are $\mathbb{S}_{+-+-}$, $\mathbb{S}_{+--+}$, and $\mathbb{S}_{++--}$, respectively (see Equations 5.9-5.11)

The four panels in Figure 5.8 comprise the total signal recovered in the propagation of the non-perturbative density matrix. Figure 5.8a**,** which shows $\mathbb{S}_{++++}$, is composed of pathways that accumulate no overall phase in the excitation process. The dominant contributions ($\sim$ 95 %, see the long τ limit) are pathways in which the first and second interactions with the field occur under one subpulse, and so $-\varphi_1+\varphi_1 = 0$ for all possible interactions. The remaining 5 % of the signal, which is responsible for the observed decay, stems from pathways represented by the diagrams Figure 5.7c. To see this we calculate, for

each value of $\phi = l\frac{\pi}{2}$, the accumulated phase, $\varphi_{acc} = -\varphi_1 + \varphi_2 + \varphi_3 - \varphi_4$, for 4 sequential pulses in the pulse train. The tabulated values of φ_{acc} are shown in Table 5-II. The notation describing these interactions, heading each column in the table, for example m = -3,-2,-1,0, simply means the m = -3 pulse interacts with the system first, then the m = -2 pulse, etc. These "interaction subsets" when summed for all possible permutations of the pulse train comprise the signals obtained in Figure 5.8.

Table 5-II Accumulated phase for interaction subsets satisfying, $\varphi_{acc} = -\varphi_1 + \varphi_2 + \varphi_3 - \varphi_4$, for a four pulse sequential excitation sequence.

	m = -3,-2,-1,0	m = -2,-1,0,+1	m = -1,0,+1,+2	m = 0,+1,+2,+3
$\phi = 0$	0	π	π	0
$\phi = \pi/2$	0	π	π	0
$\phi = \pi$	0	π	π	0
$\phi = 3\pi/2$	0	π	π	0

Looking across a row of the table, $\phi = 0$, for example, it can be seen that certain interaction subsets are p out of phase with others (compare m = -3,-2,-1,0 and m = -2,-1,0,+1). Since the interaction subsets are summed to determine the final population, the phase difference results in partial cancelation of the signal, however, because the amplitudes of each of the subpulses is not the same, the cancellation is not perfect. As an example, consider the relative magnitude of the m = -3,-2,-1,0 and m = -2,-1,0,+1 interaction subsets when $\alpha = 1.0$ (see the temporal amplitude in Figure 5.1, left) The product of subpulse amplitudes for m = -3,-2,-1,0 is much smaller than that of m = -2,-1,0,+1, and so there is very little reduction of the signal size due to cancellation between interaction subsets. It should be noted there are other interaction subsets not shown in Table 5-II that satisfy $\varphi_{acc} = -\varphi_1 + \varphi_2 + \varphi_3 - \varphi_4$ and contribute to the signal in Figure 5.8a (m = -2,-1,1,2, for example), so the dependence of the signal size on the α parameter can be complex.

Since the phase of each individual interaction subset in Table 5-II does not change with ϕ, it is clear that $\varphi_{acc} = -\varphi_1 + \varphi_2 + \varphi_3 - \varphi_4$ pathways are not sensitive to manipulations of that parameter. As a consequence, when the phase cycling scheme is employed, $\mathbb{S}_{++++}$ contains all information related to this pathway, whereas in $\mathbb{S}_{+-+-}$, $\mathbb{S}_{++--}$, and $\mathbb{S}_{+--+}$, this contribution is removed. This behavior is in contrast to the pathways satisfying the phase relationship $\varphi_{acc} = -\varphi_1 + \varphi_2 - \varphi_3 - \varphi_4$ (Figure 5.7, right); the accumulated phase values for each of the $\phi = l\frac{\pi}{2}$ manifestations of the pulse train are shown in Table 5-III, again, for each possible interaction subset.

Table 5-III Accumulated phase for interaction subsets satisfying, $\varphi_{acc} = -\varphi_1 + \varphi_2 - \varphi_3 + \varphi_4$, for a four pulse sequential excitation sequence.

	m = -3,-2,-1,0	m = -2,-1,0,+1	m = -1,0,+1,+2	m = 0,+1,+2,+3
$\phi = 0$	π	0	0	π
$\phi = \pi/2$	0	π	π	0
$\phi = \pi$	π	0	0	π
$\phi = 3\pi/2$	0	π	π	0

Now the relative phase of each of the pulses in the pulse train does affect the overall accumulated phase of the interaction subset. The consequence of this phase sensitivity is a π phase shift for $\phi = l\frac{\pi}{2}$, l = 1,3,5, etc., and so these interaction subsets are exclusively shifted to $\mathbb{S}_{+-+-}$

Shown in Table 5-IV is the accumulated phase for the interaction subsets corresponding to the double-sided Feynman diagrams in Figure 5.7a. These 2nd order interactions with an accumulated phase of $\varphi_{acc} = -\varphi_1 + \varphi_2$ are recovered in $\mathbb{S}_{++--}$ and $\mathbb{S}_{+--+}$ (Figures 5.8c and 5.8d).

Table 5-IV Accumulated phase for interaction subsets satisfying, $\varphi_{acc} = -\varphi_1 + \varphi_2$, for a two pulse sequential excitation sequence.

	m = -3,-2	m = -2,-1	m = -1,0	m = 0,+1	m = +1,+2	m = +2,+3
$\phi = 0$	$\pi/2$	$\pi/2$	$\pi/2$	$-\pi/2$	$-\pi/2$	$-\pi/2$
$\phi = \pi/2$	0	0	0	π	π	π
$\phi = \pi$	$-\pi/2$	$-\pi/2$	$-\pi/2$	$\pi/2$	$\pi/2$	$\pi/2$
$\phi = 3\pi/2$	π	π	π	0	0	0

The absence of recoverable signal traces in $\mathbb{S}_{++--}$ and $\mathbb{S}_{+--+}$ can be understood by examining the sum of interaction subsets within a pulse train. In the row $\phi = 0$ of Table 5-IV, interaction subsets that are symmetric in time around the m = 0 pulse (i.e. m = -1,0 and m = 0,+1) have equal amplitudes (since $|J_{-1}(\alpha)\, J_0(\alpha)| = |J_0(\alpha)\, J_{+1}(\alpha)|$) and a phase shift of p with respect to one another. As a consequence, these contributions will exactly cancel and there will be no signal recoverable in $\mathbb{S}_{++--}$ or $\mathbb{S}_{+--+}$.

One exception to this cancellation is the case in which the probed population is not locally invariant. In this case, populations created by earlier interaction subsets see a longer population relaxation time than later ones[1]. As a consequence, the contributions to the population are locally unequal, resulting in the oscillatory signal traces $\mathbb{S}_{++--}$ and $\mathbb{S}_{+--+}$. These are not reflecting a changing population on the excited state (as should be distinguished from $\mathbb{S}_{++++}$ and $\mathbb{S}_{+-+-}$, which do change population), rather, they are simply a consequence of changing the relative time of when the excitation event occurred. Shown in Figure 5.9 are the traces $\mathbb{S}_{++--}$and $\mathbb{S}_{+--+}$resultant from the density matrix propagation with Γ_{01}= 0.1 ps^{-1}, γ_{10}^{pure}= .02 fs^{-1}, and $\alpha = 2.25$. Again, $S\left(T, \tau; \alpha, \phi = l\frac{\pi}{2}\right)$ was collected four times for each value of l (l = 0,1,2,3) with the population recorded at T_1 = 5.0 ps.

[1] To see this, consider the example discussed in the previous paragraph with m = -1,0 and m = 0,+1. The interaction subset that occurs earlier in time sees a population decay time of T_1, whereas the later interaction subset sees a population decay time of T_1- τ.

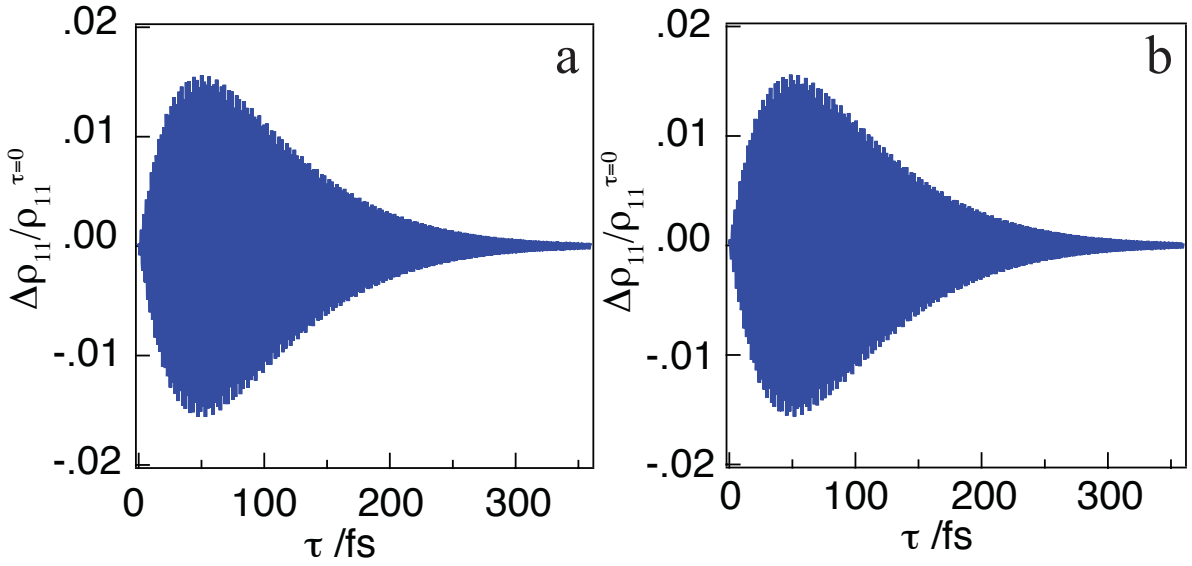

Figure 5.9 $\mathbb{S}_{+--+}$ (**a**) and $\mathbb{S}_{++--}$(**b**) calculated according to Equations 10 and 11 with $\alpha = 2.25$. The density matrix was propagated with Γ_{01}= 0.1 ps^{-1}, γ_{10}^{pure}= .02 fs^{-1} and the excited state population was recorded at T_1=5.0 ps.

The interaction subsets contributing to the observed decay in $\mathbb{S}_{++++}$ follow an analogous excitation channel as the rephasing diagrams commonly observed in experiments designed to observe the photon echo. [24] There are differences in this measurement, however. The observable in the case of this manuscript is simply the population of the excited state which could be observed via spontaneous emission if the studied chromophore was fluorescent. However, if the excited state population were to be studied by transient pump-probe type techniques, the observation of $\mathbb{S}_{++++}$ (and $\mathbb{S}_{+-+-}$) would be a 5th order measurement. The favorable properties of the photon echo remain intact in $\mathbb{S}_{++++}$. The electronic coherences created by the first (ρ_{10}, e.g.) and third (ρ_{01}) interactions with the field are complex conjugates and so the ensemble exhibits the expected rephasing behavior at a time equal to the interval between the first and second interactions with the field. In the case of sinusoidal phase modulation, all intervals between adjacent pulses have exactly the same interpulse delay time of τ. Consequently, the

electronic coherence rephases at τ, when the fourth pulse is impingent on the sample, creating ground or excited state population. As a result, inhomogeneous broadening due to static spectral dispersion in the sample does not contribute to the lineshape recovered upon Fourier transformation of $\mathbb{S}_{++++}$.

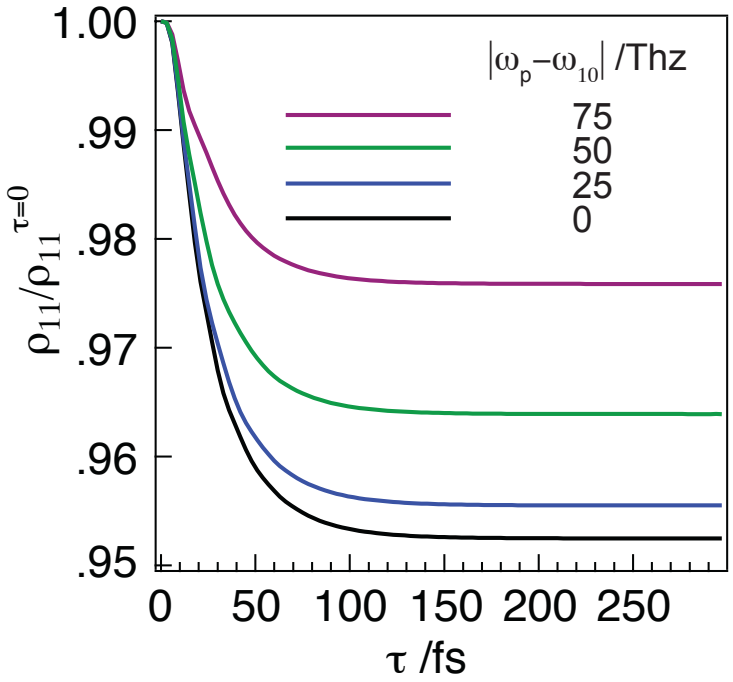

Figure 5.10 $\mathbb{S}^{++++}$ calculated for $|\omega_p - \omega_{10}| = 0$ Thz (black), 25 Thz (blue), 50 Thz (green), and 75 Thz (purple). In all cases, the signal is normalized to the excited state population at $\tau = 0$.

Shown in Figure 5.10 is $\mathbb{S}_{++++}$ calculated for the density matrix propagation under different realizations of the Hamiltonian. The resonance frequency of the system (ω_{10}) was detuned by $\pm$ 0,25,50, and 75 Thz for the black, blue, green, and purple traces, respectively. In the figure, ω_p is the center frequency of the pump field. The primary difference as the pump is detuned from the system resonance is a decrease in amplitude of the decay. This can be seen in the Figure 5.10 as the amplitude decreases from $\sim$ 5% at 0 Thz detuning to

$\sim$ 2% at 75 Thz detuning. Nevertheless, in all cases, the decay exhibits the expected $2\gamma_{10}$ rate determined by the response functions of the interaction pathways.

In the impulsive limit, with the electric field given by Equation 5.15,

$$\boldsymbol{E}(t) = A(t) \sum_{m=-\infty}^{\infty} J_m(\alpha)\, \delta(t - T - m\tau) cos\left(\omega_p(t - T - m\tau) + m\frac{\pi}{2}\right) \qquad [5.15]$$

the decaying component of $\mathbb{S}_{++++}$ is given by Equation 5.16 whose Fourier transform has a simple Lorentzian form (Equation 5.17). Note that for $\mathbb{S}_{++++}$, $\varphi_{acc} = 0$ or π (see Table 5-II), so Equation 5.16 is real.

$$\begin{aligned} &\mathbb{S}^{(4)}_{++++}(\tau, T) \\ &= A(t) \sum_{m=-\infty}^{\infty} \sum_{n=m+1}^{\infty} \left(-\frac{i}{\hbar}\right)^4 J_m(\alpha) J_{m+1}(\alpha) J_n(\alpha) J_{n+1}(\alpha) e^{i\varphi_{acc}} \\ &\quad \times \left(e^{-\Gamma_{01}(T - n\tau)} e^{-2\gamma_{10}\tau}\right) \end{aligned} \qquad [5.16]$$

$$\begin{aligned} &\mathcal{F}\left(\mathbb{S}^{(4)}_{++++}(\tau, T)\right) \\ &\propto \sum_{m=-\infty}^{\infty} \sum_{n=m+1}^{\infty} J_m(\alpha) J_{m+1}(\alpha) J_n(\alpha) J_{n+1}(\alpha) e^{i\varphi_{acc}} e^{-\Gamma_{01}T} \frac{(\gamma_{10} + n\Gamma_{01})}{(2\gamma_{10} - n\Gamma_{01})^2 + \omega^2} \end{aligned} \qquad [5.17]$$

Shown in Figure 5.11 is the normalized plot of Equation 5.17 for $\Gamma_{01} = 0$ ps^{-1} and γ_{10}^{pure}= .02 fs^{-1} as well the real Fourier transform of Figure 5.8a after subtracting the asymptotic limit of the τ domain signal. Clearly there is some broadening in the Fourier transform of $\mathbb{S}_{++++}$ with respect to Equation 5.16. This is due to the finite pulse duration used in the numerical density matrix propagation which causes additional diagrams to contribute to the observable. Nevertheless, the linewidth is within 10% of that expected in the impulsive limit showing that the technique can be used as a spectroscopic tool.

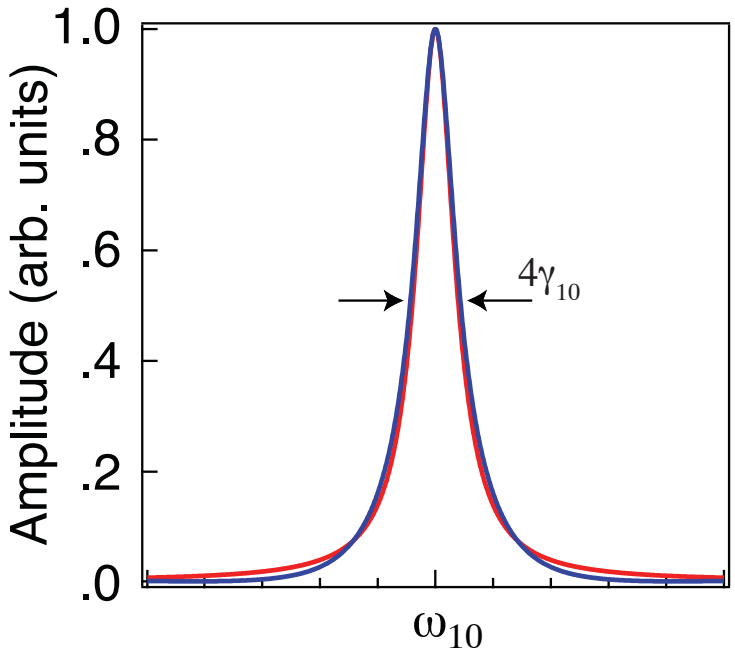

Figure 5.11 *red*: $\mathbb{S}^{(4)}_{++++}$ lineshape under impulsive excitation (Equation 5.17) *blue*: Real part of the Fourier transform of $\mathbb{S}_{++++}$ with $\alpha = 2.25$. The black arrows indicate the FWHM of the red, ideal lineshape. Comparison of the two lineshapes reveals ~10% broadening.

$$\mathbb{S}^{(4)}_{+-+-}(\tau,T) = A(t)\sum_{m=-\infty}^{\infty}\sum_{n=m+1}^{\infty}\left(-\frac{i}{\hbar}\right)^4 J_m(\alpha)J_{m+1}(\alpha)J_n(\alpha)J_{n+1}(\alpha)e^{i\varphi_{acc}} \times\left(e^{-\Gamma_{01}(T+n\tau)}e^{-2(\gamma_{10}-i\omega_{10})\tau}+c.c.\right) \quad [5.18]$$

$$\mathcal{F}\left(\mathbb{S}^{(4)}_{+-+-}(\tau,T)\right) \propto \sum_{m=-\infty}^{\infty}\sum_{n=m+1}^{\infty} J_m(\alpha)J_{m+1}(\alpha)J_n(\alpha)J_{n+1}(\alpha)e^{i\varphi_{acc}}e^{-\Gamma_{01}T} \times\frac{(\gamma_{10}+n\Gamma_{01})(4{\omega_{10}}^2+(-2\gamma+n\Gamma)^2+\omega^2)}{(4{\omega_{10}}^2+(-2\gamma+n\Gamma)^2)^2+2(-4{\omega_{10}}^2+(-2\gamma+n\Gamma)^2)\omega^2+\omega^4} \quad [5.19]$$

The perturbative expression for $\mathbb{S}_{+-+-}$ in the impulse limit is given by Equation 5.18. $\mathbb{S}^{(4)}_{+-+-}(\tau,T)$ looks much the same as Equation 5.16, however the signal has two intervals, τ,

under which the electronic coherence evolves identically as $e^{-i\omega t}$ (or $e^{+i\omega t}$ for the complex conjugate). The pathways described by $\mathbb{S}^{(4)}_{+-+-}$ are analogous to the non-rephasing pathways in third order nonlinear spectroscopy, and in contrast to $\mathbb{S}_{++++}$, they are convoluted with static inhomogeneity. [24] The Fourier transform of $\mathbb{S}^{(4)}_{+-+-}(t)$ is given by Equation 5.19. Again, note $\varphi_{acc} = 0$ or π (see Table 5-III), so $\mathbb{S}^{(4)}_{+-+-}$ is real. Equation 5.19 appears to be quite complicated, however if the population relaxation rate, $\Gamma_{01} \sim 0$ ps^{-1}, resulting in a probed population that is effectively temporally invariant, it simplifies to Equation 5.20.

$$\mathcal{F}\left(\mathbb{S}^{(4)}_{+-+-}(\tau, T)\right) \propto \sum_{m=-\infty}^{\infty} \sum_{n=m+1}^{\infty} J_m(\alpha) J_{m+1}(\alpha) J_n(\alpha) J_{n+1}(\alpha) e^{i\varphi_{acc}} \times \frac{(\gamma_{10})(4(\omega_{10}{}^2+\gamma^2)+\omega^2)}{16(\omega_{10}{}^2+\gamma^2)^2+8(-\omega_{10}{}^2+\gamma^2)\omega^2+\omega^4} \quad [5.20]$$

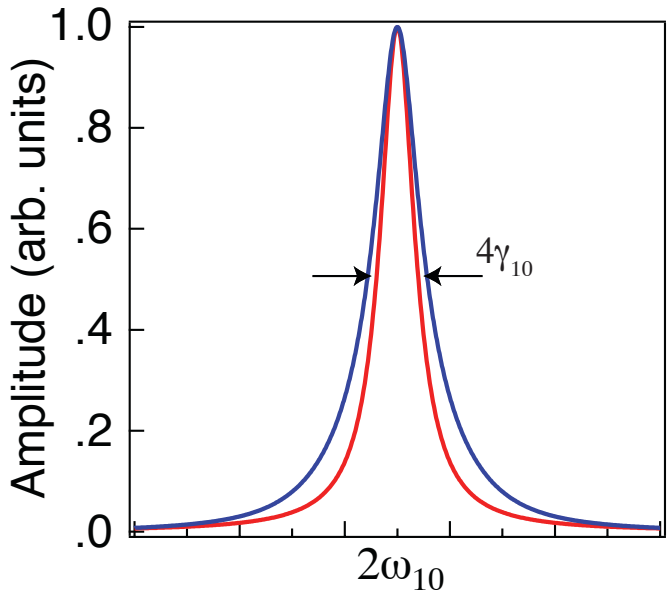

Figure 5.12 *red*: $\mathbb{S}^{(4)}_{+-+-}$ lineshape under impulsive excitation (Equation 5.17) *blue*: Real part of the Fourier transform of $\mathbb{S}_{++++}$ with $\alpha = 2.25$. The black arrows indicate the FWHM of the red, ideal lineshape. Comparison of the two lineshapes reveals ~40% broadening due to nonimpulsive excitation.

Like $\mathbb{S}_{++++}$, the lineshape recovered from Fourier transform of $\mathbb{S}_{+-+-}$ shown in Figure 5.8b shows broadening with respect to impulsive limit (Equation 5.19) due to finite pulse duration effects (Figure 5.12). In addition, because the pathways leading to the recovered signal trace are sensitive to the resonance frequency of the excited system, spectral inhomogeneity will lead to further broadening of the lineshape as shown in Figure 5.13.

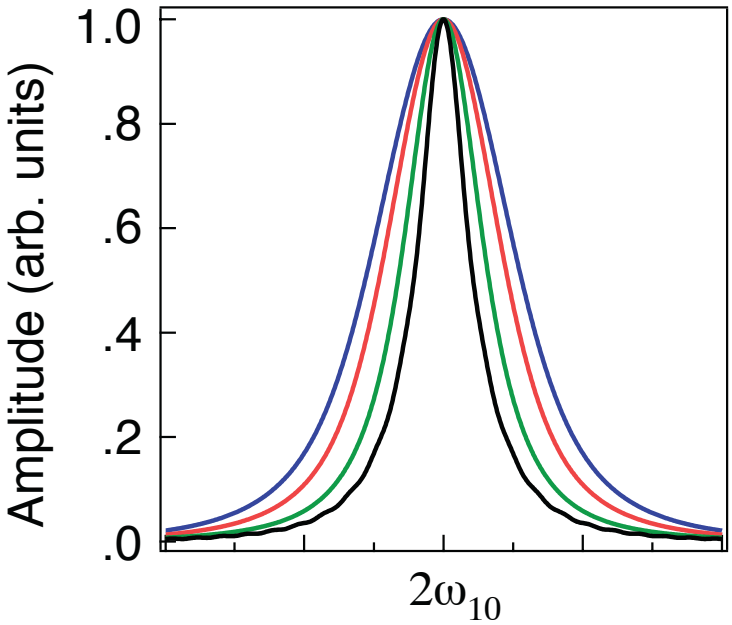

Figure 5.13 Normalized $\mathbb{S}_{+-+-}$ lineshapes with a simulated spectral inhomogeneity with a Gaussian profile and FWHM of 0 (black), 25 (green), 50 (red), and 75 Thz (blue) FWHM.

Here, $\mathbb{S}_{+-+-}$ was calculated subject to static inhomogeneity of the system by propagating the density matrix for different manifestations of the resonance frequency of the system. Each τ domain signal was weighted according to a normalized gaussian with the desired spectral width and then added before Fourier transform. Shown in Figure 5.13 are the recovered lineshapes for a sample with a inhomogeneous Gaussian spectra profile of 0, 25,

50, and 75 Thz FWHM in black, green, red, and blue, respectively showing how an inhomogeneous sample broadens the recovered lineshape.

5.5 Applications to Coherent Control

Given the ubiquity of sinusoidal spectral phase modulation in the coherent control literature, there clearly exists an opportunity to create a broadly applicable, rigorous platform for understanding control mechanisms that exploit coherent matter waves. The results presented above demonstrate that phase cycling the sinusoidal spectral phase function that creates a train of pulses can separate pathways to the excited state that are sensitive to the applied phase of the cumulative light matter interaction in differing ways. Though real molecular systems are often poorly represented by a two level model due to additional complexity, the approach employed here can be readily expanded to encompass systems with a richer spectral response.

The ultimate usefulness of this technique lies in its ability to act as test for a hypothesized control mechanism after an optimization algorithm converges on a solution with periodic character. Within the context of a given model system, subject to the rotating frame approximation, it is straightforward to propose reasonable mechanisms for coherent control. Such mechanisms can be written down as formal, perturbative corrections to the density matrix that have definite, testable phase dependencies. The experimenter can then use this phase sensitivity to isolate the proposed mechanism from other pathways contributing to the fitness observable. In this way, the solutions discovered in coherent control experiments can be described in terms of the Liouville pathways that emerge from the perturbative expansion of the density matrix.

Numerical propagation of the density matrix, where complete generality is allowed both in the light matter interaction and perhaps more importantly, in the system bath interaction, [33-36] will continue to remain a crucial tool for understanding coherent control of molecular systems. And while it may be that some coherent control mechanisms cannot be adequately described within the restrictions of the rotating wave approximation or the perturbative expansion of the density matrix [1,37-39], the keen insights that are gained from an explicit pathway description of the light matter interaction, which has so successfully served the nonlinear spectroscopy community, will remain crucially important as coherent control continues to reveal novel molecular physics.

5.6 References Cited

1. V. Prokhorenko, A. Nagy, S. Waschuk, and L. Brown, "Coherent control of retinal isomerization in bacteriorhodopsin," Science (2006).

2. V. Prokhorenko, A. Nagy, L. Brown, and R. Miller, "On the mechanism of weak-field coherent control of retinal isomerization in bacteriorhodopsin," Chem Phys **341**, 296–309 (2007).

3. J. Herek, W. Wohlleben, R. Cogdell, D. Zeidler, and M. Motzkus, "Quantum control of energy flow in light harvesting," Nature **417**, 533–535 (2002).

4. J. Savolainen, R. Fanciulli, N. Dijkhuizen, A. L. Moore, J. Hauer, T. Buckup, M. Motzkus, and J. L. Herek, "Controlling the efficiency of an artificial light-harvesting complex," P Natl Acad Sci Usa **105**, 7641–7646 (2008).

5. E. M. Grumstrup, J. C. Johnson, and N. H. Damrauer, "Enhanced triplet formation in polycrystalline tetracene films by femtosecond optical-pulse shaping.," Phys. Rev. Lett. **105**, 257403– (2010).

6. J. Savolainen, T. Buckup, J. Hauer, A. Jafarpour, C. Serrat, M. Motzkus, and J. L. Herek, "Carotenoid deactivation in an artificial light-harvesting complex via a vibrationally hot ground state," Chem Phys **357**, 181–187 (2009).

7. J. Hauer, T. Buckup, and M. Motzkus, "Enhancement of molecular modes by

electronically resonant multipulse excitation: Further progress towards mode selective chemistry," J Chem Phys **125**, 061101 (2006).

8. D. Cardoza, F. Langhojer, and C. Trallero-Herrero, "Changing pulse-shape basis for molecular learning control," Physical Review A (2004).

9. A. Bartelt, T. Feurer, and L. Woste, "Understanding optimal control results by reducing the complexity," Chem Phys **318**, 207–216 (2005).

10. D. Meshulach and Y. Silberberg, "Coherent quantum control of multiphoton transitions by shaped ultrashort optical pulses," Physical Review A **60**, 1287–1292 (1999).

11. Y. Silberberg and D. Meshulach, "Coherent quantum control of two-photon transitions by a femtosecond laser pulse," Nature **396**, 239–242 (1998).

12. T. Polack, D. Oron, and Y. Silberberg, "Control and measurement of a non-resonant Raman wavepacket using a single ultrashort pulse," Chem Phys **318**, 163–169 (2005).

13. D. Oron, N. Dudovich, D. Yelin, and Y. Silberberg, "Quantum control of coherent anti-Stokes Raman processes," Physical Review A **65**, 043408 (2002).

14. K. A. Walowicz, I. Pastirk, V. V. Lozovoy, and M. Dantus, "Multiphoton Intrapulse Interference. 1. Control of Multiphoton Processes in Condensed Phases," J. Phys. Chem. A **106**, 9369–9373 (2002).

15. V. Lozovoy, I. Pastirk, K. Walowicz, and M. Dantus, "Multiphoton intrapulse interference. II. Control of two-and three-photon laser induced …," The Journal of Chemical Physics (2003).

16. W. Wohlleben, T. Buckup, J. Herek, and M. Motzkus, "Coherent control for spectroscopy and manipulation of biological dynamics," Chemphyschem **6**, 850–857 (2005).

17. J. Hauer, T. Buckup, and M. Motzkus, "Quantum control spectroscopy of vibrational modes: Comparison of control scenarios for ground and excited states in beta-carotene," Chem Phys **350**, 220–229 (2008).

18. T. Buckup, J. Hauer, C. Serrat, and M. Motzkus, "Control of excited-state population and vibrational coherence with shaped-resonant and near-resonant excitation," J Phys B-At Mol Opt **41**, 074024 (2008).

19. J. Voll and R. de Vivie-Riedle, "Pulse trains in molecular dynamics and coherent spectroscopy: a theoretical study," New J. Phys. **11**, 105036 (2009).

20. M. A. Montgomery, E. M. Grumstrup, and N. H. Damrauer, "Fourier transform

spectroscopies derived from amplitude or phase shaping of broadband laser pulses with applications to adaptive control," J Opt Soc Am B **27**, 2518–2533 (2010).

21. E. M. Grumstrup, S.-H. Shim, M. A. Montgomery, N. H. Damrauer, and M. T. Zanni, "Facile collection of two-dimensional electronic spectra using femtosecond pulse-shaping technology," Opt Express **15**, 16681–16689 (2007).

22. S. Yan and H.-S. Tan, "Phase cycling schemes for two-dimensional optical spectroscopy with a pump-probe beam geometry," Chem Phys **360**, 110–115 (2009).

23. R. W. Boyd, *Nonlinear Optics*, Third Edition (Elsevier/Academic Press, Amsterdam, 2008).

24. S. Mukamel, *Principles of Nonlinear Optical Spectroscopy* (1995).

25. K. Blum, *Density Matrix Theory and Applications*, Second, Physics of Atoms and Molecules (Plenum Press, 1996).

26. W. Press, S. Teukolsky, S. Vetterling, and B. Flannery, *Numerical Recipes: the Art of Scientific Computing* (2007).

27. L. Seidner, G. Stock, and W. Domcke, "Nonperturbative approach to femtosecond spectroscopy: General theory and application to multidimensional nonadiabatic photoisomerization processes," The Journal of Chemical Physics (1995).

28. T. Mančal, A. V. Pisliakov, and G. R. Fleming, "Two-dimensional optical three-pulse photon echo spectroscopy. I. Nonperturbative approach to the calculation of spectra," The Journal of Chemical Physics **124**, 234504 (2006).

29. H. Wang, "Nonperturbative simulation of pump–probe spectra for electron transfer reactions in the condensed phase," Chem Phys **347**, 139–151 (2008).

30. B. Wolfseder, L. Seidner, G. Stock, and W. Domcke, "Femtosecond pump-probe spectroscopy of electron-transfer systems: a nonperturbative approach," Chem Phys (1997).

31. A. V. Pisliakov, T. Mančal, and G. R. Fleming, "Two-dimensional optical three-pulse photon echo spectroscopy. II. Signatures of coherent electronic motion and exciton population transfer in dimer two-dimensional spectra," The Journal of Chemical Physics **124**, 234505 (2006).

32. D. Jonas, "Two-dimensional femtosecond spectroscopy," Ann. Rev. Phys. Chem. **54**, 425–463 (2003).

33. P. van der Walle, M. T. W. Milder, L. Kuipers, and J. L. Herek, "Quantum control experiment reveals solvation-induced decoherence.," Proc. Natl. Acad. Sci. USA **106**,

7714–7717 (2009).

34. M. P. A. Branderhorst, P. Londero, P. Wasylczyk, C. Brif, R. L. Kosut, H. Rabitz, and I. A. Walmsley, "Coherent control of decoherence.," Science **320**, 638–643 (2008).

35. G. Katz, M. A. Ratner, and R. Kosloff, "Control by decoherence: weak field control of an excited state objective," New J. Phys. **12**, 015003 (2010).

36. M. Spanner, C. A. Arango, and P. Brumer, "Communication: Conditions for one-photon coherent phase control in isolated and open quantum systems," J Chem Phys **133**, 151101 (2010).

37. M. Joffre, "Comment on “Coherent Control of Retinal Isomerization in Bacteriorhodopsin,”" Science **317**, 453b–453b (2007).

38. V. I. Prokhorenko, A. M. Nagy, S. A. Waschuk, L. S. Brown, R. R. Birge, and R. J. Dwayne Miller, "Response to comment on “Coherent control of retinal isomerization in bacteriorhodopsin,”" Science **317**, 453c–453c (2007).

39. V. Prokhorenko, A. Nagy, and L. Brown, "On the mechanism of weak-field coherent control of retinal isomerization in bacteriorhodopsin." Chem Phys (2007).

REFERENCES CITED

Chapter 1

1. S. Mukamel, *Principles of Nonlinear Optical Spectroscopy* (1995).

2. A. M. Weiner, "Femtosecond pulse shaping using spatial light modulators," Rev. Sci. Instrum. **71**, 1929–1960 (2000).

3. A. Weiner, D. Leaird, G. Wiederrecht, and K. Nelson, "Femtosecond pulse sequences used for optical manipulation of molecular motion," Science **247**, 1317 (1990).

4. D. Yelin, D. Meshulach, and Y. Silberberg, "Adaptive femtosecond pulse compression," Opt. Lett **22**, 1793–1795 (1997).

5. E. Zeek, K. Maginnis, S. Backus, U. Russek, M. Murnane, G. Mourou, H. Kapteyn, and G. Vdovin, "Pulse compression by use of deformable mirrors," Opt. Lett **24**, 493 (1999).

6. T. Brixner, M. Strehle, and G. Gerber, "Feedback-controlled optimization of amplified femtosecond laser pulses," Appl Phys B-Lasers O **68**, 281–284 (1999).

7. D. J. Tannor and S. A. Rice, "Control of selectivity of chemical reaction via control of wave packet evolution," J Chem Phys **83**, 5013 (1985).

8. D. Tannor, R. Kosloff, and S. Rice, "Coherent pulse sequence induced control of selectivity of reactions - exact quantum-mechanical calculations," J Chem Phys **85**, 5805–5820 (1986).

9. P. Brumer and M. Shapiro, "Control of unimolecular reactions using coherent-light," Chem. Phys. Lett. **126**, 541–546 (1986).

10. M. Shapiro, "A Uniform Theory of Preparation, Dissociation, and Product Formation in the Decay of Overlapping Resonances," J. Phys. Chem. A **102**, 9570–9576 (1998).

11. A. Zewail, "Laser selective chemistry 3-is it possible.," Physics Today **November**, 1–8 (1980).

12. F. F. Crim, "Selective excitation studies of unimolecular reaction dynamics," Annual Review of Physical Chemistry **35**, 657–691 (1984).

13. N. Bloembergen and A. H. Zewail, "Energy redistribution in isolated molecules and the question of mode-selective laser chemistry revisited. New experiments on the dynamics of collisionless energy redistribution in molecules possibilities for laser-selective chemistry with subpicosecond pulses," The Journal of Physical Chemistry **88**, 5459–5465 (1984).

14. A. Assion, T. Baumert, M. Bergt, T. Brixner, B. Kiefer, V. Seyfried, M. Strehle, and G. Gerber, "Control of chemical reactions by feedback-optimized phase-shaped femtosecond laser pulses," Science **282**, 919–922 (1998).

15. R. J. Levis, G. M. Menkir, and H. Rabitz, "Selective bond dissociation and rearrangement with optimally tailored, strong-field laser pulses.," Science **292**, 709–713 (2001).

16. N. H. Damrauer, C. Dietl, G. Krampert, S. H. Lee, K. H. Jung, and G. Gerber, "Control of bond-selective photochemistry in CH2BrCl using adaptive femtosecond pulse shaping," The European Physical Journal D - Atomic, Molecular and Optical Physics **20**, 71–76 (2002).

17. D. Cardoza, M. Baertschy, and T. Weinacht, "Understanding learning control of molecular fragmentation," Chemical Physics Letters **411**, 311–315 (2005).

18. Y. Silberberg and D. Meshulach, "Coherent quantum control of two-photon transitions by a femtosecond laser pulse," Nature **396**, 239–242 (1998).

19. D. Meshulach and Y. Silberberg, "Coherent quantum control of multiphoton transitions by shaped ultrashort optical pulses," Physical Review A **60**, 1287–1292 (1999).

20. T. Brixner, N. Damrauer, and G. Gerber, *Femtosecond Quantum Control* (2001), Vol. 46, pp. 1–54.

21. N. Dudovich, B. Dayan, Gallagher Faeder SM, and Y. Silberberg, "Transform-limited pulses are not optimal for resonant multiphoton transitions.," Phys. Rev. Lett. **86**, 47–50 (2001).

22. D. Oron, N. Dudovich, D. Yelin, and Y. Silberberg, "Quantum control of coherent anti-Stokes Raman processes," Physical Review A **65**, 043408 (2002).

23. N. Dudovich, D. Oron, and Y. Silberberg, "Single-pulse coherently controlled nonlinear Raman spectroscopy and microscopy," Nature **418**, 512–514 (2002).

24. T. Brixner, N. Damrauer, B. Kiefer, and G. Gerber, "Liquid-phase adaptive femtosecond quantum control: Removing intrinsic intensity dependencies," J Chem Phys **118**, 3692–3701 (2003).

25. T. Polack, D. Oron, and Y. Silberberg, "Control and measurement of a non-resonant Raman wavepacket using a single ultrashort pulse," Chem Phys **318**, 163–169 (2005).

26. M. A. Montgomery, R. R. Meglen, and N. H. Damrauer, "General method for the dimension reduction of adaptive control experiments," J. Phys. Chem. A **110**, 6391–6394 (2006).

27. M. A. Montgomery and N. H. Damrauer, "Elucidation of control mechanisms discovered during adaptive manipulation of [ru(dpb) 3](pf 6) 2emission in the solution phase," J. Phys. Chem. A **111**, 1426–1433 (2007).

28. C. Bardeen, Q. Wang, and C. Shank, "Selective excitation of vibrational wave packet motion using chirped pulses.," Phys. Rev. Lett. **75**, 3410–3413 (1995).

29. C. Bardeen, Q. Wang, and C. Shank, "Femtosecond chirped pulse excitation of vibrational wave packets in LD690 and bacteriorhodopsin," J. Phys. Chem. A **102**, 2759–2766 (1998).

30. C. Bardeen, V. Yakovlev, J. Squier, and K. Wilson, "Quantum control of population transfer in green fluorescent protein by using chirped femtosecond pulses," J Am Chem Soc **120**, 13023–13027 (1998).

31. J. Cao, C. Bardeen, and K. Wilson, "Molecular pi pulses: Population inversion with positively chirped short pulses," J Chem Phys **113**, 1898–1909 (2000).

32. R. Judson and H. Rabitz, "Teaching lasers to control molecules," Phys. Rev. Lett. **68**, 1500–1503 (1992).

33. J. Herek, W. Wohlleben, R. Cogdell, D. Zeidler, and M. Motzkus, "Quantum control of energy flow in light harvesting," Nature **417**, 533–535 (2002).

34. J. Savolainen, R. Fanciulli, N. Dijkhuizen, A. L. Moore, J. Hauer, T. Buckup, M. Motzkus, and J. L. Herek, "Controlling the efficiency of an artificial light-harvesting complex," P Natl Acad Sci Usa **105**, 7641–7646 (2008).

35. W. Wohlleben, T. Buckup, J. Herek, and M. Motzkus, "Coherent control for spectroscopy and manipulation of biological dynamics," Chemphyschem **6**, 850–857 (2005).

36. J. Hauer, T. Buckup, and M. Motzkus, "Enhancement of molecular modes by electronically resonant multipulse excitation: Further progress towards mode

selective chemistry," J Chem Phys **125**, 061101 (2006).

37. J. Hauer, T. Buckup, and M. Motzkus, "Quantum control spectroscopy of vibrational modes: Comparison of control scenarios for ground and excited states in beta-carotene," Chem Phys **350**, 220–229 (2008).

38. T. Buckup, J. Hauer, C. Serrat, and M. Motzkus, "Control of excited-state population and vibrational coherence with shaped-resonant and near-resonant excitation," J Phys B-At Mol Opt **41**, 074024 (2008).

39. P. van der Walle, M. Milder, and L. Kuipers, "Quantum control experiment reveals solvation-induced decoherence," Proceedings of the National Academy of Sciences (2009).

40. P. Brumer and M. Shapiro, "One photon mode selective control of reactions by rapid or shaped laser pulses: An emperor without clothes?," Chemical Physics **139**, 221–228 (1989).

41. V. I. Prokhorenko, A. M. Nagy, and R. J. Dwayne Miller, "Coherent control of the population transfer in complex solvated molecules at weak excitation. An experimental study," J Chem Phys **122**, 184502 (2005).

42. V. Prokhorenko, A. Nagy, S. Waschuk, and L. Brown, "Coherent control of retinal isomerization in bacteriorhodopsin," Science (2006).

43. M. P. A. Branderhorst, P. Londero, P. Wasylczyk, C. Brif, R. L. Kosut, H. Rabitz, and I. A. Walmsley, "Coherent control of decoherence.," Science **320**, 638–643 (2008).

44. M. Joffre, "Comment on “Coherent Control of Retinal Isomerization in Bacteriorhodopsin,”" Science **317**, 453b–453b (2007).

45. V. I. Prokhorenko, A. M. Nagy, S. A. Waschuk, L. S. Brown, R. R. Birge, and R. J. Dwayne Miller, "Response to comment on “Coherent control of retinal isomerization in bacteriorhodopsin,”" Science **317**, 453c–453c (2007).

46. G. Katz, M. A. Ratner, and R. Kosloff, "Control by decoherence: weak field control of an excited state objective," New J. Phys. **12**, 015003 (2010).

47. M. Spanner, C. A. Arango, and P. Brumer, "Communication: Conditions for one-photon coherent phase control in isolated and open quantum systems," J Chem Phys **133**, 151101 (2010).

48. J. White, B. Pearson, and P. Bucksbaum, "Extracting quantum dynamics from genetic learning algorithms through principal control …," J. Phys. B (2004).

49. D. Cardoza, C. Trallero-Herrero, F. Langhojer, H. Rabitz, and T. Weinacht, "Transformations to diagonal bases in closed-loop quantum learning control experiments.," The Journal of Chemical Physics **122**, 124306 (2005).

50. M. A. Montgomery, R. R. Meglen, and N. H. Damrauer, "General method for reducing adaptive laser pulse-shaping experiments to a single control variable," J. Phys. Chem. A **111**, 5126–5129 (2007).

51. D. G. Kuroda, C. P. Singh, Z. Peng, and V. D. Kleiman, "Mapping excited-state dynamics by coherent control of a dendrimer's photoemission efficiency.," Science **326**, 263–267 (2009).

52. B. Amstrup, R. J. Carlson, A. Matro, and S. A. Rice, "Use of pulse shaping to control the photodissociation of a diatomic molecule: preventing the best from being the enemy of the good," The Journal of Physical Chemistry **95**, 8019–8027 (1991).

53. T. Hornung, M. Motzkus, and R. de Vivie-Riedle, "Teaching optimal control theory to distill robust pulses even under experimental constraints," Physical Review A **65**, (2002).

54. M. A. Montgomery and N. H. Damrauer, "A convenient method to simulate and visually represent two-photon power spectra of arbitrarily and adaptively shaped broadband laser pulses," New J. Phys. **11**, 105053 (2009).

55. M. A. Montgomery, E. M. Grumstrup, and N. H. Damrauer, "Fourier transform spectroscopies derived from amplitude or phase shaping of broadband laser pulses with applications to adaptive control," J Opt Soc Am B **27**, 2518–2533 (2010).

56. A. Prakelt, M. Wollenhaupt, A. Assion, C. Horn, C. Sarpe-Tudoran, M. Winter, and T. Baumert, "Compact, robust, and flexible setup for femtosecond pulse shaping," Rev. Sci. Instrum. **74**, 4950–4953 (2003).

57. J. Vaughan, T. Feurer, K. Stone, and K. Nelson, "Analysis of replica pulses in femtosecond pulse shaping with pixelated devices," Opt Express **14**, 1314–1328 (2006).

58. D. Tannor, "Coherent pulse sequence control of product formation in chemical reactions," Advances in chemical physics (1988).

59. M. Shapiro and P. Brumer, "Laser control of product quantum state populations in unimolecular reactions," J Chem Phys **84**, 4103–4104 (1986).

60. E. M. Grumstrup, S.-H. Shim, M. A. Montgomery, N. H. Damrauer, and M. T. Zanni, "Facile collection of two-dimensional electronic spectra using

femtosecond pulse-shaping technology," Opt Express **15**, 16681–16689 (2007).

61. E. M. Grumstrup, J. C. Johnson, and N. H. Damrauer, "Enhanced triplet formation in polycrystalline tetracene films by femtosecond optical-pulse shaping.," Phys. Rev. Lett. **105**, 257403 (2010).

Chapter 2

1. J. D. Hybl, A. W. Albrecht, S. M. Gallagher Faeder, and D. M. Jonas, "Two-dimensional electronic spectroscopy," Chemical Physics Letters **297**, 307-313 (1998).

2. I. Stiopkin, T. Brixner, M. Yang, and G. R. Fleming, "Heterogeneous Exciton Dynamics Revealed by Two-Dimensional Optical Spectroscopy," The Journal of Physical Chemistry B **110**, 20032-20037 (2006).

3. G. S. Engel, T. R. Calhoun, E. L. Read, T.-K. Ahn, T. s. Mančal, Y.-C. Cheng, R. E. Blankenship, and G. R. Fleming, "Evidence for wavelike energy transfer through quantum coherence in photosynthetic systems," Nature **446**, 782-786 (2007).

4. D. Zigmantas, "Two-dimensional electronic spectroscopy of the B800-B820 light-harvesting complex," Proc. Natl. Acad. Sci. USA **103**, 12672-12677 (2006).

5. S. M. Gallagher Faeder and D. M. Jonas, "Two-Dimensional Electronic Correlation and Relaxation Spectra: Theory and Model Calculations," The Journal of Physical Chemistry A **103**, 10489-10505 (1999).

6. D. Jonas, "Two-dimensional femtosecond spectroscopy," Ann. Rev. Phys. Chem. **54**, 425-463 (2003).

7. G. Goodno, G. Dadusc, and R. Miller, "Ultrafast heterodyne-detected transient-grating spectroscopy using diffractive optics," Journal Of The Optical Society Of America B-Optical Physics **15**, 1791-1794 (1998).

8. T. Brixner, T. Mancal, I. Stiopkin, and G. Fleming, "Phase-stabilized two-dimensional electronic spectroscopy," Journal Of Chemical Physics **121**, 4221-4236 (2004).

9. V. Volkov, R. Schanz, and P. Hamm, "Active phase stabilization in Fourier-transform two-dimensional infrared spectroscopy," Opt. Lett **30**, 2010-2012 (2005).

10. T. Zhang, C. Borca, X. Li, and S. Cundiff, "Optical two-dimensional Fourier transform spectroscopy with active interferometric stabilization," Opt. Exp. **13**, 7432-7441 (2005).

11. M. Dugan, J. Tull, and W. Warren, "High-resolution acousto-optic shaping of unamplified and amplified femtosecond laser pulses," Journal Of The Optical Society Of America B-Optical Physics **14**, 2348-2358 (1997).

12. P. Tian, D. Keusters, Y. Suzaki, and W. Warren, "Femtosecond phase-coherent two-dimensional spectroscopy," Science **300**, 1553-1555 (2003).

13. P. Tekavec, G. Lott, and A. Marcus, "Flourescence-Detected Two-Dimensional Electronic Coherence Spectroscopy by Acousto-Optic Phase Modulation," Journal Of Chemical Physics **127**(2007).

14. J. Vaughan, T. Hornung, K. Stone, and K. Nelson, "Coherently controlled ultrafast four-wave mixing spectroscopy," The Journal of Physical Chemistry A **111**, 4873-4883 (2007).

15. M. F. Emde, W. P. de Boeij, M. S. Pshenichnikov, and D. A. Wiersma, "Spectral interferometry as an alternative to time-domain heterodyning.," Opt. Lett **22**, 1338-1340 (1997).

16. E. M. Grumstrup, S.-H. Shim, M. A. Montgomery, N. H. Damrauer, and M. T. Zanni, "Facile collection of two-dimensional electronic spectra using femtosecond pulse-shaping technology," Optics Express **15**, 16681-16689 (2007).

17. L. P. Deflores, R. A. Nicodemus, and A. Tokmakoff, "Two-dimensional Fourier transform spectroscopy in the pump-probe geometry.," Opt. Lett **32**, 2966-2968 (2007).

18. J. A. Myers, K. L. M. Lewis, P. F. Tekavec, and J. P. Ogilvie, "Two-color two-dimensional Fourier transform electronic spectroscopy with a pulse-shaper.," Optics Express **16**, 17420-17428 (2008).

19. P. E. Tekavec, J. A. Myers, K. L. M. Lewis, and J. P. Ogilvie, "Two-dimensional electronic spectroscopy with a continuum probe," Opt. Lett **34**, 1390-1392 (2009).

20. D. Abramavicius and S. Mukamel, "Disentangling multidimensional femtosecond spectra of excitons by pulse shaping with coherent control," Journal Of Chemical Physics **120**, 8373 (2004).

21. V. I. Prokhorenko, A. Halpin, and R. J. D. Miller, "Coherently-controlled two-dimensional photon echo electronic spectroscopy," Optics Express **17**, 9764 (2009).

22. M. D. Levenson and G. L. Eesley, "Polarization Selective Optical Heterodyne-Detection for Dramatically Improved Sensitivity in Laser Spectroscopy," Applied Physics **19**, 1-17 (1979).

23. S. Mukamel, *Principles of Nonlinear Optical Spectroscopy* (1995).

24. W. Wagner, C. Li, J. Semmlow, and W. Warren, "Rapid phase-cycled two-dimensional optical spectroscopy in fluorescence and transmission mode," Opt. Exp. **13**, 3697-3706 (2005).

25. S. Yan and H.-S. Tan, "Phase cycling schemes for two-dimensional optical spectroscopy with a pump-probe beam geometry," Chemical Physics **360**, 110-115 (2009).

26. S.-H. Shim, D. Strasfeld, Y. Ling, and M. Zanni, "Automated 2D IR spectroscopy using a mid-IR pulse shaper and application of this technology to the human islet amyloid polypeptide," Proc. Natl. Acad. Sci. USA **104**, 14197-14202 (2007).

27. J. Vaughan, T. Feurer, K. Stone, and K. Nelson, "Analysis of replica pulses in femtosecond pulse shaping with pixelated devices," Optics Express **14**, 1314-1328 (2006).

28. A. Weiner, "Femtosecond pulse shaping using spatial light modulators," Review of Scientific Instruments (2000).

29. D. Keusters, H. Tan, and W. Warren, "Role of pulse phase and direction in two-dimensional optical spectroscopy," The Journal of Physical Chemistry A **103**, 10369-10380 (1999).

30. L. Seidner, G. Stock, and W. Domcke, "Nonperturbative approach to femtosecond spectroscopy: General theory and application to multidimensional nonadiabatic photoisomerization processes," The Journal of Chemical Physics (1995).

31. B. Wolfseder, L. Seidner, G. Stock, and W. Domcke, "Femtosecond pump-probe spectroscopy of electron-transfer systems: a nonperturbative approach," Chemical Physics (1997).

32. H. Wang and M. Thoss, "Nonperturbative simulation of pump–probe spectra for electron transfer reactions in the condensed phase," Chemical Physics Letters **389**, 43-50 (2004).

33. T. s. Mančal, A. V. Pisliakov, and G. R. Fleming, "Two-dimensional optical three-pulse photon echo spectroscopy. I. Nonperturbative approach to the calculation of spectra," The Journal of Chemical Physics **124**, 234504 (2006).

34. R. W. Boyd, *Nonlinear optics,* Third ed. (Elsevier/Academic Press, Amsterdam, 2008).

35. K. Blum, *Density matrix theory and applications,* Second ed., Physics of Atoms and Molecules (Plenum Press, New York, 1996).

36. A. Albrecht, J. Hybl, S. Faeder, and D. Jonas, "Experimental distinction between phase shifts and time delays: Implications for femtosecond spectroscopy and coherent control of chemical reactions," Journal Of Chemical Physics **111**, 10934-10956 (1999).

37. D. Jonas, (personal communication, August 10, 2011).

Chapter 3

1. A. Nozik, "Quantum dot solar cells," Physica E: Low-dimensional Systems and Nanostructures (2002).

2. R. Schaller and V. Klimov, "High efficiency carrier multiplication in PbSe nanocrystals: Implications for solar energy conversion," Physical Review Letters **92**(2004).

3. R. Ellingson, M. Beard, J. Johnson, and P. Yu, "Highly efficient multiple exciton generation in colloidal PbSe and PbS quantum dots," Nano Lett (2005).

4. A. J. Nozik, M. C. Beard, J. M. Luther, M. Law, R. J. Ellingson, and J. C. Johnson, "Semiconductor Quantum Dots and Quantum Dot Arrays and Applications of Multiple Exciton Generation to Third-Generation Photovoltaic Solar Cells," Chemical Reviews **110**, 6873-6890 (2010).

5. V. Klimov, "Spectral and dynamical properties of multilexcitons in semiconductor nanocrystals," Annual Review of Physical Chemistry **58**, 635-673 (2007).

6. V. Klimov, "Mechanisms for photogeneration and recombination of multiexcitons in semiconductor nanocrystals: Implications for lasing and solar energy conversion," Journal Of Physical Chemistry B **110**, 16827-16845 (2006).

7. R. D. Schaller, V. M. Agranovich, and V. I. Klimov, "High-efficiency carrier multiplication through direct photogeneration of multi-excitons via virtual single-exciton states," Nature Physics **1**, 189-194 (2005).

8. A. Shabaev, A. L. Efros, and A. J. Nozik, "Multiexciton generation by a single photon in nanocrystals," Nano Lett **6**, 2856-2863 (2006).

9. A. Franceschetti, J. An, and A. Zunger, "Impact ionization can explain carrier multiplication in PbSe quantum dots," Nano Lett (2006).

10. Y. Silberberg and D. Meshulach, "Coherent quantum control of two-photon transitions by a femtosecond laser pulse," Nature (1998).

11. D. Meshulach and Y. Silberberg, "Coherent quantum control of multiphoton transitions by shaped ultrashort optical pulses," Physical Review A (1999).

12. T. Brixner, N. Damrauer, and G. Gerber, *Femtosecond quantum control*, Advances in Atomic, Molecular, and Optical Physics, Vol 46 (2001), Vol. 46, pp. 1-54.

13. J. Herek, W. Wohlleben, R. Cogdell, D. Zeidler, and M. Motzkus, "Quantum control of energy flow in light harvesting," Nature **417**, 533-535 (2002).

14. T. Brixner, N. Damrauer, B. Kiefer, and G. Gerber, "Liquid-phase adaptive femtosecond quantum control: Removing intrinsic intensity dependencies," Journal Of Chemical Physics **118**, 3692-3701 (2003).

15. W. Wohlleben, T. Buckup, J. Herek, and M. Motzkus, "Coherent control for spectroscopy and manipulation of biological dynamics," Chemphyschem **6**, 850-857 (2005).

16. M. A. Montgomery, R. R. Meglen, and N. H. Damrauer, "General Method for the Dimension Reduction of Adaptive Control Experiments," The Journal of Physical Chemistry A **110**, 6391-6394 (2006).

17. M. A. Montgomery and N. H. Damrauer, "Elucidation of Control Mechanisms Discovered during Adaptive Manipulation of [Ru(dpb) 3](PF 6) 2Emission in the Solution Phase," The Journal of Physical Chemistry A **111**, 1426-1433 (2007).

18. M. P. A. Branderhorst, P. Londero, P. Wasylczyk, C. Brif, R. L. Kosut, H. Rabitz, and I. A. Walmsley, "Coherent control of decoherence.," Science **320**, 638-643 (2008).

19. M. A. Montgomery, E. M. Grumstrup, and N. H. Damrauer, "Fourier transform spectroscopies derived from amplitude or phase shaping of broadband laser pulses with applications to adaptive control," Journal Of The Optical Society Of America B-Optical Physics **27**, 2518-2533 (2010).

20. T. Kobayashi and A. Shirakawa, "Sub-10-fs tunable pulses in visible and NIR and visible sub-5-fs pulses generated by noncollinear OPA," Journal of Luminescence **87**, 119-120 (2000).

21. J. Piel, M. Beutter, and E. Riedle, "20-50-fs pulses tunable across the near infrared from a blue-pumped noncollinear parametric amplifier," Optics Letters **25**, 180-182 (2000).

22. T. Feurer and A. Glass, "Two-photon photoconductivity in SiC photodiodes and its application to autocorrelation measurements of femtosecond optical pulses," Applied Physics B-Lasers And Optics (1997).

23. T. Buckup, T. Lebold, A. Weigel, W. Wohlleben, and M. Motzkus, "Singlet versus triplet dynamics of beta-carotene studied by quantum control spectroscopy," Journal of Photochemistry and Photobiology a-Chemistry **180**, 314-321 (2006).

24. J. Hauer, T. Buckup, and M. Motzkus, "Quantum control spectroscopy of vibrational modes: Comparison of control scenarios for ground and excited states in beta-carotene," Chemical Physics **350**, 220-229 (2008).

25. E. M. Grumstrup, J. C. Johnson, and N. H. Damrauer, "Enhanced triplet formation in polycrystalline tetracene films by femtosecond optical-pulse shaping," Physical Review Letters **105**, 257403- (2010).

26. P. Brumer and M. Shapiro, "Control of unimolecular reactions using coherent light," Chem. Phys. Lett. **126**, 541-546 (1986).

27. M. Shapiro and P. Brumer, "Laser control of product quantum state populations in unimolecular reactions," Journal Of Chemical Physics **84**, 4103-4104 (1986).

28. V. Klimov, J. McGuire, R. Schaller, and V. Rupasov, "Scaling of multiexciton lifetimes in semiconductor nanocrystals," Physical Review B **77**(2008).

29. E. M. Grumstrup, S.-H. Shim, M. A. Montgomery, N. H. Damrauer, and M. T. Zanni, "Facile collection of two-dimensional electronic spectra using femtosecond pulse-shaping technology," Optics Express **15**, 16681-16689 (2007).

30. W. Press, S. Teukolsky, S. Vetterling, and B. Flannery, *Numerical Recipes: The art of Scientific Computing* (2007).

31. R. W. Boyd, *Nonlinear optics,* Third ed. (Elsevier/Academic Press, Amsterdam, 2008), p. xx+613.

32. A. V. Pisliakov, T. s. Mančal, and G. R. Fleming, "Two-dimensional optical three-pulse photon echo spectroscopy. II. Signatures of coherent electronic motion and exciton population transfer in dimer two-dimensional spectra," The Journal of Chemical Physics **124**, 234505 (2006).

33. N. Dudovich, D. Oron, and Y. Silberberg, "Single-pulse coherently controlled nonlinear Raman spectroscopy and microscopy," Nature **418**, 512-514 (2002).

34. T. Polack, D. Oron, and Y. Silberberg, "Control and measurement of a non-resonant Raman wavepacket using a single ultrashort pulse," Chemical Physics **318**, 163-169 (2005).

35. B. Cho, W. K. Peters, R. J. Hill, T. L. Courtney, and D. M. Jonas, "Bulklike Hot Carrier Dynamics in Lead Sulfide Quantum Dots," Nano Lett **10**, 2498-2505 (2010).

36. H. Kamisaka, S. V. Kilina, K. Yamashita, and O. V. Prezhdo, "Ultrafast vibrationally-induced dephasing of electronic excitations in PbSe quantum dot," Nano Lett **6**, 2295-2300 (2006).

37. S. Kilina, C. Craig, D. Kilin, and O. Prezhdo, "Ab initio time-domain study of phonon-assisted relaxation of charge carriers in a PbSe quantum dot," Journal of Physical Chemistry C (2007).

Chapter 4

1. W. Shockley and H. J. Queisser, "Detailed Balance Limit of Efficiency of p-n Junction Solar Cells," Journal Of Applied Physics **32**, 510-519 (1961).

2. J. Tauc, "Electron impact ionization in semiconductors," Journal of Physics and Chemistry of Solids (1959).

3. C. Swenberg and W. Stacy, "Bimolecular radiationless transitions in crystalline tetracene," Chem. Phys. Lett. **2**, 327-328 (1968).

4. M. Pope and C. E. Swenberg, *Electronic Processes in Organic Crystals and Polymers,* 2nd ed. (Oxford University Press, New York, 1999).

5. A. J. Nozik, M. C. Beard, J. M. Luther, M. Law, R. J. Ellingson, and J. C. Johnson, "Semiconductor Quantum Dots and Quantum Dot Arrays and Applications of Multiple Exciton Generation to Third-Generation Photovoltaic Solar Cells," Chemical Reviews **110**, 6873-6890 (2010).

6. I. Paci, J. Johnson, X. Chen, G. Rana, D. Popovic, D. David, A. Nozik, M. Ratner, and J. Michl, "Singlet fission for dye-sensitized solar cells: Can a suitable sensitizer be found?," Journal Of The American Chemical Society **128**, 16546-16553 (2006).

7. M. B. Smith and J. Michl, "Singlet Fission," Chemical Reviews **110**, 6891-6936 (2010).

8. M. C. Hanna and A. J. Nozik, "Solar conversion efficiency of photovoltaic and photoelectrolysis cells with carrier multiplication absorbers," Journal Of Applied Physics **100**, 074510 (2006).

9. R. C. Johnson and R. E. Merrifield, "Effects of Magnetic Fields on the Mutual Annihilation of Triplet Excitons in Anthracene Crystals," Physical Review B **1**, 896-902 (1970).

10. S. H. Lim, T. G. Bjorklund, F. C. Spano, and C. J. Bardeen, "Exciton delocalization and superradiance in tetracene thin films and nanoaggregates," Physical Review Letters **92**(2004).

11. V. K. Thorsmolle, R. D. Averitt, J. Demsar, D. L. Smith, S. Tretiak, R. L. Martin, X. Chi, B. K. Crone, A. P. Ramirez, and A. J. Taylor, "Morphology Effectively Controls Singlet-Triplet Exciton Relaxation and Charge Transport in Organic Semiconductors," Physical Review Letters **102**(2009).

12. T. S. Kuhlman, J. Kongsted, K. V. Mikkelsen, K. B. Moller, and T. I. Solling, "Interpretation of the Ultrafast Photoinduced Processes in Pentacene Thin Films," Journal Of The American Chemical Society **132**, 3431-3439 (2010).

13. P. M. Zimmerman, Z. Zhang, and C. B. Musgrave, "Singlet fission in pentacene through multi-exciton quantum states," Nature Chemistry **2**, 648-652 (2010).

14. E. M. Grumstrup, J. C. Johnson, and N. H. Damrauer, "Enhanced triplet formation in polycrystalline tetracene films by femtosecond optical-pulse shaping," Physical Review Letters **105**, 257403- (2010).

15. W. Hofberger, "Structure and Optical-Properties of Polycrystalline Evaporated Tetracene Films," Phys Status Solidi A **30**, 271-278 (1975).

16. T. Kobayashi and A. Shirakawa, "Sub-10-fs tunable pulses in visible and NIR and visible sub-5-fs pulses generated by noncollinear OPA," Journal of Luminescence **87**, 119-120 (2000).

17. J. Piel, M. Beutter, and E. Riedle, "20-50-fs pulses tunable across the near infrared from a blue-pumped noncollinear parametric amplifier," Optics Letters **25**, 180-182 (2000).

18. A. Prakelt, M. Wollenhaupt, A. Assion, C. Horn, C. Sarpe-Tudoran, M. Winter, and T. Baumert, "Compact, robust, and flexible setup for femtosecond pulse shaping," Review of Scientific Instruments **74**, 4950-4953 (2003).

19. T. Feurer and A. Glass, "Two-photon photoconductivity in SiC photodiodes and its application to autocorrelation measurements of femtosecond optical pulses," Applied Physics B-Lasers And Optics (1997).

20. R. Judson and H. Rabitz, "Teaching lasers to control molecules," Physical Review Letters **68**, 1500-1503 (1992).

21. M. A. Montgomery, R. R. Meglen, and N. H. Damrauer, "General Method for the Dimension Reduction of Adaptive Control Experiments," The Journal of Physical Chemistry A **110**, 6391-6394 (2006).

22. A. S. Davydov, *Theory of Molecular Excitons* (McGraw-Hill, New York, 1962).

23. M. Voigt, A. Langner, P. Schouwink, J. M. Lupton, R. F. Mahrt, and M. Sokolowski, "Picosecond time resolved photoluminescence spectroscopy of a tetracene film on highly oriented pyrolytic graphite: Dynamical relaxation, trap emission, and superradiance," Journal Of Chemical Physics **127**(2007).

24. Y. H. Meyer, R. Astier, and J. M. Leclercq, "Triplet-Triplet Spectroscopy of Polyacenes," Journal Of Chemical Physics **56**, 801-& (1972).

25. J. R. Weinberg-Wolf, L. E. McNeil, S. Liu, and C. Kloc, "Evidence of low intermolecular coupling in rubrene single crystals by Raman scattering," Journal Of Physics-Condensed Matter **19**, 276204 (2007).

26. R. Lehnig and A. Slenczka, "Spectroscopic investigation of the solvation of organic molecules in superfluid helium droplets," Journal Of Chemical Physics **122**(2005).

27. P. M. Zimmerman and C. B. Musgrave, (personal communication, 2010).

28. Y. Tomkiewicz, R. P. Groff, and P. Avakian, "Spectroscopic Approach to Energetics of Exciton Fission and Fusion in Tetracene Crystals," Journal Of Chemical Physics **54**, 4504-& (1971).

29. R. Jankowiak, J. Kalinowski, M. Konys, and J. Buchert, "Solid-State Transitions in Crystalline Tetracene," Chem. Phys. Lett. **65**, 549-553 (1979).

30. E. Venuti, R. G. Della Valle, L. Farina, A. Brillante, M. Masino, and A. Girlando, "Phonons and structures of tetracene polymorphs at low temperature and high pressure," Physical Review B **70**(2004).

31. P. M. Zimmerman, (personal communication, 2011).

32. C. Bardeen, V. Yakovlev, J. Squier, and K. Wilson, "Quantum control of population transfer in green fluorescent protein by using chirped femtosecond pulses," Journal Of The American Chemical Society **120**, 13023-13027 (1998).

33. J. Cao, C. Bardeen, and K. Wilson, "Molecular pi pulses: Population inversion with positively chirped short pulses," Journal Of Chemical Physics **113**, 1898-1909 (2000).

34. J. Herek, W. Wohlleben, R. Cogdell, D. Zeidler, and M. Motzkus, "Quantum control of energy flow in light harvesting," Nature **417**, 533-535 (2002).

35. D. Cardoza, F. Langhojer, and C. Trallero-Herrero, "Changing pulse-shape basis for molecular learning control," Physical Review A (2004).

36. A. Bartelt, T. Feurer, and L. Woste, "Understanding optimal control results by reducing the complexity," Chemical Physics **318**, 207-216 (2005).

37. T. Buckup, J. Hauer, C. Serrat, and M. Motzkus, "Control of excited-state population and vibrational coherence with shaped-resonant and near-resonant excitation," Journal Of Physics B-Atomic Molecular And Optical Physics **41**, 074024 (2008).

38. A. Weiner, "Femtosecond pulse shaping using spatial light modulators," Review of Scientific Instruments **71**, 1929-1960 (2000).

39. J. Vaughan, T. Feurer, K. Stone, and K. Nelson, "Analysis of replica pulses in femtosecond pulse shaping with pixelated devices," Optics Express **14**, 1314-1328 (2006).

40. J. Hauer, H. Skenderovic, K. Kompa, and M. Motzkus, "Enhancement of Raman modes by coherent control in beta-carotene," Chem. Phys. Lett. **421**, 523-528 (2006).

41. J. Hauer, T. Buckup, and M. Motzkus, "Enhancement of molecular modes by electronically resonant multipulse excitation: Further progress towards mode selective chemistry," Journal Of Chemical Physics **125**, 061101 (2006).

42. A. Weiner, D. Leaird, G. Wiederrecht, and K. Nelson, "Femtosecond Pulse Sequences Used for Optical Manipulation of Molecular Motion," Science **247**, 1317 (1990).

43. H. Kawashima, M. Wefers, and K. Nelson, "Femtosecond Pulse Shaping, Multiple-Pulse Spectroscopy, and Optical Control," Ann. Rev. Phys. Chem. **46**, 627-656 (1995).

44. J. Hauer, T. Buckup, and M. Motzkus, "Quantum control spectroscopy of vibrational modes: Comparison of control scenarios for ground and excited states in beta-carotene," Chemical Physics **350**, 220-229 (2008).

Chapter 5

1. V. Prokhorenko, A. Nagy, S. Waschuk, and L. Brown, "Coherent control of retinal isomerization in bacteriorhodopsin," Science (2006).

2. V. Prokhorenko, A. Nagy, L. Brown, and R. Miller, "On the mechanism of weak-field coherent control of retinal isomerization in bacteriorhodopsin," Chem Phys **341**, 296–309 (2007).

3. J. Herek, W. Wohlleben, R. Cogdell, D. Zeidler, and M. Motzkus, "Quantum control of energy flow in light harvesting," Nature **417**, 533–535 (2002).

4. J. Savolainen, R. Fanciulli, N. Dijkhuizen, A. L. Moore, J. Hauer, T. Buckup, M. Motzkus, and J. L. Herek, "Controlling the efficiency of an artificial light-harvesting complex," P Natl Acad Sci Usa **105**, 7641–7646 (2008).

5. E. M. Grumstrup, J. C. Johnson, and N. H. Damrauer, "Enhanced triplet formation in polycrystalline tetracene films by femtosecond optical-pulse shaping.," Phys. Rev. Lett. **105**, 257403– (2010).

6. J. Savolainen, T. Buckup, J. Hauer, A. Jafarpour, C. Serrat, M. Motzkus, and J. L. Herek, "Carotenoid deactivation in an artificial light-harvesting complex via a vibrationally hot ground state," Chem Phys **357**, 181–187 (2009).

7. J. Hauer, T. Buckup, and M. Motzkus, "Enhancement of molecular modes by electronically resonant multipulse excitation: Further progress towards mode selective chemistry," J Chem Phys **125**, 061101 (2006).

8. D. Cardoza, F. Langhojer, and C. Trallero-Herrero, "Changing pulse-shape basis for molecular learning control," Physical Review A (2004).

9. A. Bartelt, T. Feurer, and L. Woste, "Understanding optimal control results by reducing the complexity," Chem Phys **318**, 207–216 (2005).

10. D. Meshulach and Y. Silberberg, "Coherent quantum control of multiphoton transitions by shaped ultrashort optical pulses," Physical Review A **60**, 1287–1292 (1999).

11. Y. Silberberg and D. Meshulach, "Coherent quantum control of two-photon transitions by a femtosecond laser pulse," Nature **396**, 239–242 (1998).

12. T. Polack, D. Oron, and Y. Silberberg, "Control and measurement of a non-resonant Raman wavepacket using a single ultrashort pulse," Chem Phys **318**, 163–169 (2005).

13. D. Oron, N. Dudovich, D. Yelin, and Y. Silberberg, "Quantum control of

coherent anti-Stokes Raman processes," Physical Review A **65**, 043408 (2002).

14. K. A. Walowicz, I. Pastirk, V. V. Lozovoy, and M. Dantus, "Multiphoton Intrapulse Interference. 1. Control of Multiphoton Processes in Condensed Phases," J. Phys. Chem. A **106**, 9369–9373 (2002).

15. V. Lozovoy, I. Pastirk, K. Walowicz, and M. Dantus, "Multiphoton intrapulse interference. II. Control of two-and three-photon laser induced …," The Journal of Chemical Physics (2003).

16. W. Wohlleben, T. Buckup, J. Herek, and M. Motzkus, "Coherent control for spectroscopy and manipulation of biological dynamics," Chemphyschem **6**, 850–857 (2005).

17. J. Hauer, T. Buckup, and M. Motzkus, "Quantum control spectroscopy of vibrational modes: Comparison of control scenarios for ground and excited states in beta-carotene," Chem Phys **350**, 220–229 (2008).

18. T. Buckup, J. Hauer, C. Serrat, and M. Motzkus, "Control of excited-state population and vibrational coherence with shaped-resonant and near-resonant excitation," J Phys B-At Mol Opt **41**, 074024 (2008).

19. J. Voll and R. de Vivie-Riedle, "Pulse trains in molecular dynamics and coherent spectroscopy: a theoretical study," New J. Phys. **11**, 105036 (2009).

20. M. A. Montgomery, E. M. Grumstrup, and N. H. Damrauer, "Fourier transform spectroscopies derived from amplitude or phase shaping of broadband laser pulses with applications to adaptive control," J Opt Soc Am B **27**, 2518–2533 (2010).

21. E. M. Grumstrup, S.-H. Shim, M. A. Montgomery, N. H. Damrauer, and M. T. Zanni, "Facile collection of two-dimensional electronic spectra using femtosecond pulse-shaping technology," Opt Express **15**, 16681–16689 (2007).

22. S. Yan and H.-S. Tan, "Phase cycling schemes for two-dimensional optical spectroscopy with a pump-probe beam geometry," Chem Phys **360**, 110–115 (2009).

23. R. W. Boyd, *Nonlinear Optics*, Third Edition (Elsevier/Academic Press, Amsterdam, 2008).

24. S. Mukamel, *Principles of Nonlinear Optical Spectroscopy* (1995).

25. K. Blum, *Density Matrix Theory and Applications*, Second, Physics of Atoms and

Molecules (Plenum Press, 1996).

26. W. Press, S. Teukolsky, S. Vetterling, and B. Flannery, *Numerical Recipes: the Art of Scientific Computing* (2007).

27. L. Seidner, G. Stock, and W. Domcke, "Nonperturbative approach to femtosecond spectroscopy: General theory and application to multidimensional nonadiabatic photoisomerization processes," The Journal of Chemical Physics (1995).

28. T. Mančal, A. V. Pisliakov, and G. R. Fleming, "Two-dimensional optical three-pulse photon echo spectroscopy. I. Nonperturbative approach to the calculation of spectra," The Journal of Chemical Physics **124**, 234504 (2006).

29. H. Wang, "Nonperturbative simulation of pump–probe spectra for electron transfer reactions in the condensed phase," Chem Phys **347**, 139–151 (2008).

30. B. Wolfseder, L. Seidner, G. Stock, and W. Domcke, "Femtosecond pump-probe spectroscopy of electron-transfer systems: a nonperturbative approach," Chem Phys (1997).

31. A. V. Pisliakov, T. Mančal, and G. R. Fleming, "Two-dimensional optical three-pulse photon echo spectroscopy. II. Signatures of coherent electronic motion and exciton population transfer in dimer two-dimensional spectra," The Journal of Chemical Physics **124**, 234505 (2006).

32. D. Jonas, "Two-dimensional femtosecond spectroscopy," Ann. Rev. Phys. Chem. **54**, 425–463 (2003).

33. P. van der Walle, M. T. W. Milder, L. Kuipers, and J. L. Herek, "Quantum control experiment reveals solvation-induced decoherence.," Proc. Natl. Acad. Sci. USA **106**, 7714–7717 (2009).

34. M. P. A. Branderhorst, P. Londero, P. Wasylczyk, C. Brif, R. L. Kosut, H. Rabitz, and I. A. Walmsley, "Coherent control of decoherence.," Science **320**, 638–643 (2008).

35. G. Katz, M. A. Ratner, and R. Kosloff, "Control by decoherence: weak field control of an excited state objective," New J. Phys. **12**, 015003 (2010).

36. M. Spanner, C. A. Arango, and P. Brumer, "Communication: Conditions for one-photon coherent phase control in isolated and open quantum systems," J Chem Phys **133**, 151101 (2010).

37. M. Joffre, "Comment on “Coherent Control of Retinal Isomerization in Bacteriorhodopsin,”" Science **317**, 453b–453b (2007).

38. V. I. Prokhorenko, A. M. Nagy, S. A. Waschuk, L. S. Brown, R. R. Birge, and R. J. Dwayne Miller, "Response to comment on “Coherent control of retinal isomerization in bacteriorhodopsin,”" Science **317**, 453c–453c (2007).

39. V. Prokhorenko, A. Nagy, and L. Brown, "On the mechanism of weak-field coherent control of retinal isomerization in bacteriorhodopsin." Chem Phys (2007).